Космични изследвания в България

Том 4 . София . 1983

Българска академия на науките

Space Research in Bulgaria

Volume 4 . Sofia . 1983

Bulgarian Academy of Sciences

Contents

Содержание

1

2

On the Kinetic Processes in the Middle Ionosphere during Sunset

K. B. Serafimov

The formation of a deep "valley" above the E-layer after sunset, the layer-like formations observed within it and the patterns of their motions have been known for a long time. Thus in [1, 2, 3] we have shown that the $E2$ layer appears on the ionograms obtained by probe measurements at mid-geomagnetic latitudes mainly at sunrise-sunset periods and this was interpreted in terms of shielding of the daytime E-layer. Its critical frequencies f_0E vary more in dependence on the solar zenith angle and this results in the positive values of the difference $d = f_0E2 - f_0E$ in the sunset-sunrise period and ionosondes record the presence of the $E2$ layer. The strong dynamics of the layer-like formations in the valley during the night and their intensive vertical motions are fairly well known. In particular, our analysis of the incoherent scatter radar data from Arecibo ($\varphi = 18.4°N$, $\lambda = 66.8°W$), published in [4], confirms the presence of multilayer-like structure in the region between 100 and 170-180 km, which is moving almost permanently during the night. Here we shall discuss again the data from this incoherent scatter radar (more details for the instrument and patterns of determination of the electron density vertical distribution see in [5, 6, 7]). The necessity of their correct interpretation would be shown in terms of possibilities to define some new physical parameters.

The problems of nighttime and sunset-sunrise variations of the electron density N_e over Arecibo have been discussed in many publications, e. g. [4, 8, 9], etc. In [9] an attempt has been made to define the height distribution of the effective recombination coefficient α_{eff} on data from the electron density N_e variations. Based on the profiles used in [4, 9], here we shall demonstrate some new possibilities for correct analysis of ionizing-neutralizing and dynamic processes in the middle ionosphere. By the term middle ionosphere here we shall understand the part between 100 and 180 km according to the definition given in [3] as the basis analysis would refer to a higher region — from 130 to 200 km. The principal balance equation from the familiar α-type is analysed in [9]:

$$(1) \qquad \frac{dN_e}{dt} = q - \alpha_{eff}N_e^2,$$

where q is the ion production rate, which in the sunset period is $q \approx 0$. We can find in [9] that the time variation of $1/N_e$ at constant height of $[Z = const]$ re-

presents almost a straight line. That is why the authors of the same paper consider the dependence (1) at $q \approx 0$ to be accurately realized for the sunrise-sunset period and the coefficient α_{eff} can be defined as an angular coefficient of the straight line (2) obtained by integrating (1):

$$(2) \qquad \frac{1}{N_e} \approx \alpha_{eff} t + C_0,$$

where C_0 is constant depending on the height Z. Based on this an altitudinal profile for the effective recombination coefficient $\alpha_{eff}(Z)$ is determined in [9], which, compared to the theoretical data for the specific coefficients of the dissociative recombination of O_2^+ and NO^+ ions, demonstrates great differences from them. The α_{eff} coefficient obtained on data from $N_e(t)$ in the upper part of the discussed region (over 170 km) is smaller than the two specific coefficients $\alpha_D(O_2^+)$ and $\alpha_D(NO^+)$ and at the bottom part of the region (about 140 km) the α_{eff} thus calculated is almost equal to $\alpha_D(NO^+) \approx 2\alpha_D(O_2^+)$, which is rather impossible due to the abundance of O_2^+ ions at these heights. Therefore, the profile of $\alpha_{eff}(Z)$ is obtained in [9], which is very different from all available data of laboratory and theoretical values for the possible vertical distribution of the recombination coefficient. These significant differences are interpreted in [9] by a probably stronger temperature dependence of $\alpha_D(T_e)$ with respect to the laboratory data and deviation from the condition $q = 0$, because a certain portion of the solar radiation still penetrates to these heights. But the evaluation of all possible ionization sources in the middle ionosphere (L_α, L_β, CIII, 900-1000 Å continuum, soft-X-ray radiation with $\lambda = 40$ to 200 Å, etc.) definitely shows that the integral intensity of the solar ionizing radiations disappears after sunset due to the dense atmospheric layers the sunbeam has to penetrate. The radiation scattered by the geocorona is of negligible importance to the relatively high level of the N_e presunset values, but could be of minimum importance during the sunrise period. Therefore, there are no serious arguments to explain the great difference between the $\alpha_{eff}(Z)$ distributions obtained by the electron density profile, on the one hand, and the theoretical and laboratory values of the recombination coefficient — on the other, as defined in [9].

The significant differences between α_{eff} values calculated from Arecibo ionospheric data and the theoretical and laboratory data values of this magnitude may be explained considering the strong motion of sunset-sunrise ionosphere and, in particular, the intensive vertical movements between 130 and 200 km over the earth during these transition periods. This reasonable physical consideration requires the application of the following well-known form of the balance equation (see for ex. [3]) in (1):

$$(3) \qquad \frac{dN_e}{dt} = q - \alpha N_e^2 - \text{div}(N_e \mathbf{V}),$$

where $\mathbf{V}$ is the total plasma bulk velocity. The familiar expressions including the diffusion may be applied to the divergent term in (3), but the vertical ionization transfer is determinant for the sunset-rise plasma motions between 130 and 200 km. That is why the divergent term in (3) is often replaced by its vertical part only. Taking into consideration that $q \approx 0$ in the examined period and denoting $\text{div}(N_e \mathbf{V}) \approx M$, from (3) we obtain

$$(4) \qquad \frac{dN_e}{dt} = -\alpha N_e^2 - M.$$

4

In the time integration of (4) we obtain first approximation

$$(5) \qquad \frac{1}{N_e} \approx \left(-\alpha - \frac{M}{N_e^2}\right) \cdot t + C_0.$$

The experimental fact that the dependence between $1/N_e$ and the time t is almost straightly linear is considered in (5). And such straight linearity is possible only when the factor before the time t is constant, i. e.

$$(6) \qquad \alpha + \frac{M}{N_e^2} \approx \text{const.}$$

The constant of the right-hand side is equal to α_{eff} according to formula (2).

The straight linear dependence between $1/N_e$ and t is confirmed by all data available from Arecibo for thd sunset period. Therefore, if not neglecting motions, we should consider them as modifying α_{eff} to incredible values compared with laboratory measurements and theoretical calculations. It follows from (6) that

$$(7) \qquad \frac{M}{N_e^2} = A,$$

where the A value is constant at sunrise-sunset period but changes with the altitude Z.

The dependence (7) is of particular interest because it demonstrates that the time variations of the motion contribution to the middle ionospheric balance during sunrise-sunset period are proportional to the square of the electron density, i. e.

$$(8) \qquad M(t)|_{z=\text{const}} = A N_e^2(t)|_{z=\text{const}}.$$

It follows from (6) that the correction which should reduce the α_{eff} value to more realistic quantities is the magnitude $A(Z)$ according to [9]. In fact, the α_{eff} value of (2) is identic to the sum $\alpha_{\text{eff}} + A$ in (5). Therefore, if we have computations on the α_{eff} value from other measurements, it would be possible to calculate the factor A from (5) and from there — the contribution of the motions M. In order to obtain tentative values of the divergent term M, we have to proceed as follows: to define theoretically the value of the coefficient α as an effective coefficient of the dissociative recombination in a medium with significant concentration of molecular O_2^+ and NO^+ ions

$$(9) \qquad \alpha = \frac{\alpha_D(O_2^+)[O_2^+]^2 + \alpha_D(NO^+)[NO^+]}{[O_2^+] + [NO^+] + [O^+]}.$$

The yield of (9) shows the fact that the total ion concentration between 130 and 200 km is defined by the sum of the denominator under the examined conditions, i. e.

$$(10) \qquad [O_2^+] + [NO^+] + [O^+] = N_i = N_e.$$

In order to define altitudinal variations of α, we use most recently determined values of the temperature dependence of $\alpha_D(O_2^+)$ and $\alpha_D(NO_2^+)$ which according to [10] are:

$$(11) \qquad \alpha_D(O_2^+) = 1.6 \times 10^{-7} \left(\frac{T_e}{300}\right)^{-0.55},$$

$$(12) \qquad \alpha_D(NO^+) = 4.2 \times 10^{-7} \left(\frac{T_e}{300}\right)^{-0.85}.$$

When there is no available evidence on the vertical distributions of the ion densities over Arecibo, for the examined period we use the data on the relative ion densities: $[O_2^+]/N_e$ and $[NO^+]/N_e$ according to the IRI model [11]. We also apply the IRI model for the vertical distribution of the electron tempera-
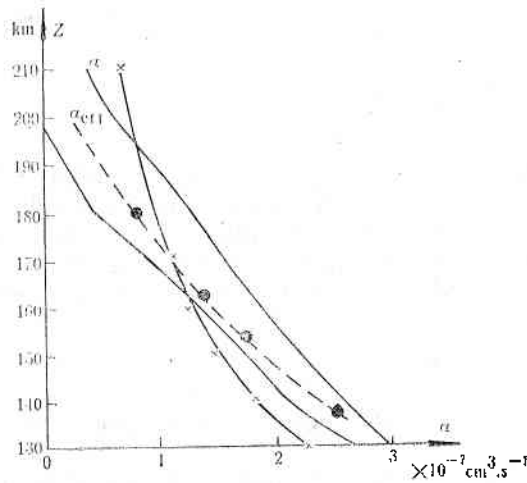
F ig. 1
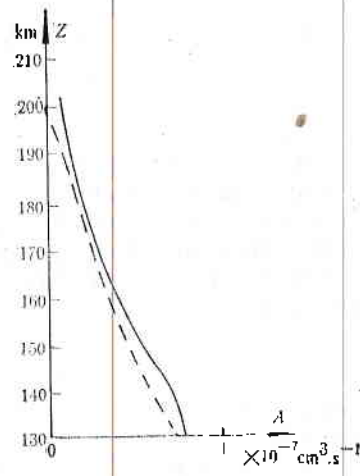
Fig. 2

ture $T_e(Z)$ but with the corrections from our measurements performed with IRI the Vertical series rockets (see [12]). If we denote $K_{O_2^+} = [O_2^+]/N_e$ and $K_{NO^+} = [NO^+]/N_e$, we shall obtain

(13)
$$\alpha = \alpha_D(O_2^+)K_{O_2^+} + \alpha_D(NO^+)K_{NO^+}$$

for α according to [9]. The vertical profiles of $\alpha_D(O_2^+)$ and $\alpha_D(NO^+)$ are built according to [11], [12] and the $T_e(Z)$ vertical profile — according to IRI and the corrections from [12]. The coefficients $K_{O_2^+}$ and K_{NO^+} are determined using IRI, and the altitudinal profile of V is defined from [11], as shown in Fig. 1. The same Figure demonstrates as an example the profile of α_{eff} as obtained in [9] on data from sunset values of $N_e(t, Z)$ for Sept. 9, 1966 and calculated according to formula (2), i. e. neglecting motions. The analysis of avialable sunset-sunrise data from Arecibo, computed by formula (2) although with certain variations, confirms the curve in Fig. 1. The data scatter is shown with hatched area in the Figure. In first approximation we may consider the values of α_{eff} from [9] as close to the average ones for this quantity obtained with the primitive analysis performed by formula (2). The comparison between theoretical α and the field of α_{eff} values shows that the deviations between these two values are not a random phenomenon but are rather of a basic nature. This confirms the important role of motions in the nocturnal middle ionosphere and Fig. 1 clearly shows that α is greater than all the values of α_{eff} obtained for $Z > 190$ km and $\alpha < \alpha_{eff}$ for heights $Z < 160$ km. An approximate equality exists between 160 and 190 km and for the particular case of Sept. 9, 1966 this equalization appears at 170 km.

The altitudinal profile for

(14)
$$A(Z) = \alpha_{eff}^{-\alpha}$$

6

can be built using euaqtions (5), (6) and (7). Figure 2 shows this profile for the conditions in [9].

Figure 3 demonstrates three vertical profiles of $\dot{M}$ for the sunset period of Sept. 9, 1966 (for the beginning of the sunset at 18 h 28 min LT; for a ty-
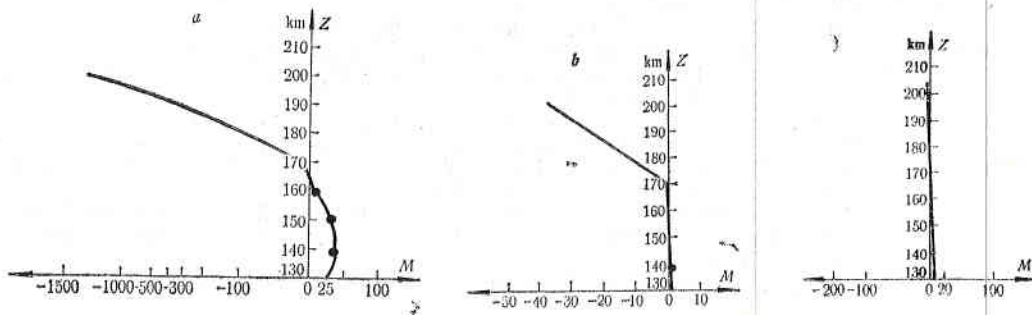
Fig. 3

pical moment at 19 h 29 min LT and for one of the final moments at 20 h 02 min LT, respectively). The absence of M values in the altitudinal region between 140 and 160 km is due to the decrease of N_e below the measurement possibilities of the incoherent radar. The calculations of M are performed according to formula (8).

It is seen from Fig. 3 that the value $M(Z)$ changes in sign at altitude of about 165 km. It is clear from Fig. 1 for the dependence (14) that for the altitudinal region from 160 to 190 km we shall obtain a systematic change in sign of M for all cases available in Arecibo. In the upper part the electron transfer increases the electron density and in the sunset period it reacts as a particular ionizing factor. The reverse phenomenon takes place in the bottom part — the electron transfer decreases the electron density and is equivalent of the neutralization increase.

Of course, factor M is not precisely adequate to the contribution of motions in the balance equation (3) because the coefficient α was theoretically found and all the measurement errors as well as the deviations of the IRI model from reality are included in the magnitude M. But in first approximation we may consider that M represents values similar to the divergent term in (3) and when using other methods to find for instance the electron temperature and the ion composition the contribution of the motions can be determined accurately.

From this paper we can make the conclusion that the contribution of motions to the formation of the night structure of the middle ionosphere is not to be neglected and the complete analysis of the neutralizing processes cannot be performed on the basis of chemical eduilibrium only. Together with this we assume that it is useful and important to define the constant ratio between motions M contribtion to the squared electron density (see formula (6)).

7

References

1. Serafimov, K., D. Samardjiev. — Compt. rend. Acad. bulg. sci., **16**, 1963, 4, p. 365.
2. Самарджиев, Д., К. Серафимов. — Изв. Геофиз. инст. БАН, **4**, 1963, с. 109.
3. Серафимов, К. Физика средней ионосферы. С., БАН, 1970.
4. Серафимов, К. - Съобщения, 1978, No 1.
5. Gordon, W. E., L. M. LaLonde. — IRE Trans., **9AP**, 1961, p. 17.
6. Carlson, H. C. CRSR Report 212 (Cornell University, Ithaca, New York), 1965.
7. The Users' Manual for the Arecibo Observatory. Nat. Astr. and Ionosph. Center (Ithaca, New York — Arecibo, Puerto Rico), 1976.
8. Mahajan, K. K., O. P. Saxena. — J. Geophys. Res., **81**, 1976, p. 3165.
9. Mahajan, K. K., — Indian J. of Radio and Space Phys., 7, 1978, p. 132.
10. Torr, D. Q., M. R. Torr, J. C. Walker, A. O. Nier, L. H. Brace, H. C. Brinton. — J. Geophys. Res., **81**, 1976, p. 5578.
11. Rawer, R., S. Ramakrishnan, D. Bilitza. Preliminary Ref. Profiles for Electron and Ion Densities and Temperatures prop. for the Intern. Reference Ionosphere. IPW — Sci. Rep. W. B. 2, 1975.
12. Серафимов, К. Космические исследования в Болгарии. С., БАН, 1979.

О кинетических процессах в средней ионосфере при закате Солнца

К. Б. Серафимов

Резюме)

Показано, что для полноценного анализа временных и высотных изменений электронной концентрации в ночной и восходно-закатной средней ионосфере (в пределах от 130 до 200 km над Землей) необходимо учитывать перенос электронов и ионов. Учет этого переноса по данным инкогерентного радара в Arecibo приводит к выводу, что временные изменения переноса на данной постоянной высоте пропорциональны N_e^2. Исходя из модели IRI и данных об электронной концентрации, полученных в Arecibo, определены теоретические изменения эффективного рекомбинационного коэффициента α, а по его разностям с значениями α_{eff}, вычисленными по ионосферным данным (пренебрегая движениями), вычислены высотные изменения дивергентного члена в основном уравнении баланса электронной концентрации.

On Some Problems in Geophysics Solved with the Help of Satellites on Polar Orbits

V. M. Balebanov, M. M. Gogoshev, E. M. Dubinin,
I. S. Kutiev, I. M. Podgorniy, K. B. Serafimov

I. Convection

The initial *in situ* measurements on board Injun-5 and OGO-6 have shown the existence of two vortex convection [1, 2]. One of the major factors defining this picture is the direction of the interplanetary magnetic field (IMF). The convective fluxes in the polar cap become asymmetric in dependence on the sign of the magnetic field component B_y, in their shift to morning or evening side. Measurements on board AE-C provided for certain precision on this model [3]. The change of convection direction was found to occur in sufficiently narrow longitudinal band located near noon. Experiments with laboratory magnetospheric model [4, 5] have shown that in dependence on the sign of the vertical component of the interplanetary magnetic field B_z, the direction of convection changes to reverse in the polar cap. It was shown that magnetospheric field lines materialize into interplanetary field lines in the region of the polar casp. This gives evidence to the existence of magnetic field lines common for the earth dipole and the solar wind. If we use the concepts of the classical magnetic hydrodynamics, we may say that in the region of the polar casp reconnection of earth magnetic lines with solar wind takes place.

In dependence on the vertical component of the interplanetary field B_z, the reconnection appears either near the equatorial or the polar boundary of the casp. The convection in the polar cap in terms of the south component of the interplanetary magnetic field ($B_z < 0$) always appears in direction away from the Sun. This fact has been confirmed by numerous measurements. Under $B_z > 0$ the convection from the Sun is observed only at small B_z values. When increasing the positive value of B_z, the convection direction becomes reversive in the polar cap region. A typical dependence of the morning-evening (E_y) electric field component on B_z in the polar cap under undisturbed supersonic flux interacting with the magnetic field dipole is given in Fig. 1.

Besides the effects of reconnection, an important factor determinant of the convection picture are the viscous processes at the magnetospheric boundary. It is well seen in Fig. 1 that the sign of the electric field in the polar cap

and therefore the convection direction changes become reverse only at sufficiently large positive values of B_z.

Important consequence from the viscous interaction effects is the fact that part of the convective currents generated by the solar wind plasma flux in the
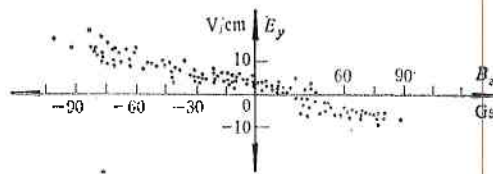
Fig. 1. Electric field dependence on the value and the sign of the vertical component (B_z) of the magnetic field in free flux (model experiment) for the polar cap.
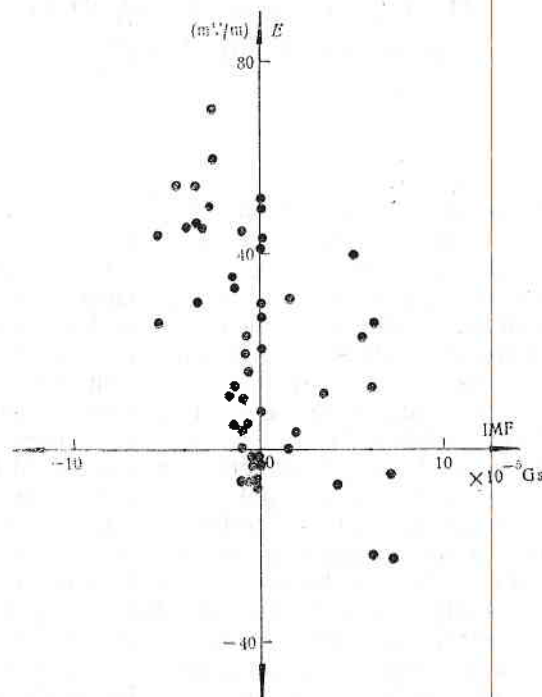
Fig. 2. Electric field dependence on the vertical component (balloon measurements) for the polar cap.

boundary magnetospheric layer is located at closed field lines [4]. Considering the south component of the interplanetary magnetic field, the convection remains in general the same but new convection fluxes appear on the open field lines in the polar cap. Although the conclusions based on laboratory experiments are confirmed by some ground-based observations, they still require further illumination.

10

Information obtained from measurements over the earth polar cap is often contradictory, i. e. the correct electric field measurements are not yet a reliable method. Balloon measurements [6], carried out by Mózer as early as 1974 (Fig. 2), agree rather well with the laboratory data but the large scatter of
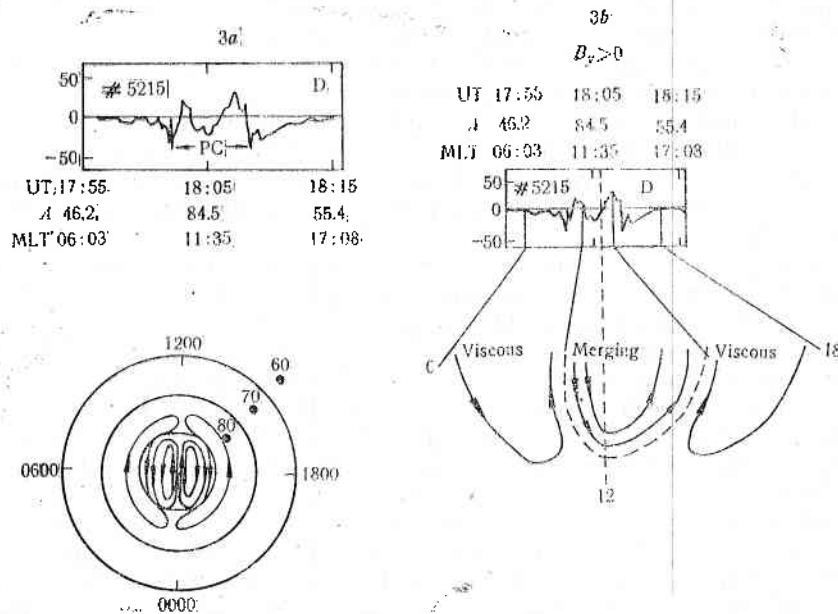
Fig. 3. Electric field distribution in the polar cap under the northern component of four-vortex convection model (a), three-vortex model (b)

the points in Fig. 2 makes questionable the statement that at large positive B_z values the plasma drift in the polar cap is really reversive to the solar wind. Many geophysicists even do not consider the possibility of existence of such drift phenomenon. Additional evidence on the correctness of the results obtained for the existence of the polar cap convection and sun convection at $B_z > 0$ was obtained recently.

Data from [7] which give results from measurements of the electric field on board the polar satellite S3-2 show that at the northern component of the interplanetary field, a clearly expressed convection in the polar cap is to be seen oriented sunward. Nevertheless, it is difficult to state that the situation is completely comprehensive. Thus, for instance, some authors based on measurements from S3-2 conclude on the generation of two additional vortex systems in the polar cap under the northern component of IMF (two convective vortex systems result from effects of the viscous interaction and other two—from effects of the reconnection) (Fig. 3a). There is another interpretation of the same data given in [8]. Crooker considers the northern component of IMF to add only one convective nucleus to the polar cap (Fig. 3b). Thus, the results shown here demonstrate the necessity of systematic electric field measurements in auroral regions and in the polar cap.

2. Field-Aligned Currents

The field-aligned currents play a key role in the energy transfer from solar wind to polar ionosphere. Magnetic field disturbances due to the field-aligned currents have been studied for years. The basic portion of the data on the field-aligned current distribution was obtained on TRIAD satellite. The results from these measurements are already well known and it is aimless to consider them in detail. Brief summary on the results might be represented as follows 1) two current systems (1) and (2) are available (Fig. 4). The current system (1) coincides approximately with the polar portion of the auroral oval and system (2) — with its equatorial portion; 2) the current in system (1) flows to the ionosphere — in the evening side; the direction of currents in system (2) is reverse; 3) current in system (1) exceeds, on the average, the current flow in system (2).

We should note that only the magnetic measurements performed on board Triad satellite composed the experiment. Charged particles and electric fields experiments were not envolved in this program.

Many results support the fact of increased informativity in simultaneous measurements of charged particles and field-aligned currents. This is clearly expressed in the experiments on ISIS-2 [9,10]. The data comparison between magnetic measurements and simultaneous electron fluxes measurements within the energy range of 0.15-10 keV enabled the discovery of new interesting features. The poleward boundary of the current system (1) coincides with the high-latitudinal boundary of plasma layer. In the case of B_z (IMF)$<1\gamma$, morning and evening sectors, change of convection direction often takes place at lower latitudes, compared to the latitude at which the outer boundary in plasma layer is projected. This provides for the very important conclusion that the outer region of the plasma layer at low altitudes, where the convection is oriented from the Sun, is projected in the viscous boundary layer adjacent to the magnetosphere boundary. This result supports conclusions reached on the basis of laboratory modelling. It is interesting to note that although electric field measurements were not performed on board ISIS-2, the picture of convection was reconstructed by magnetic measurements only. The magnetic lines which can be considered as elastic strings, convect in a conductive ionosphere and
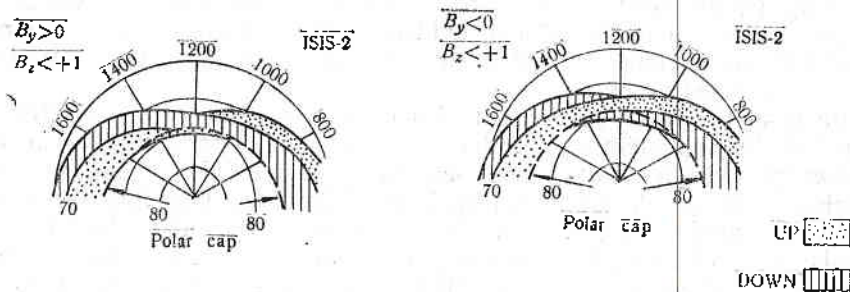
Fig. 4. Field-aligned current picture for $By>0$ and $By<0$ on TRIAD data and on ISIS-2 data. Convection directions are given with arrows

therefore experience a force $J \times B$. This force, acting in direction opposite to the convection, would result in a slight change of the magnetic field vector. Thus, we may judge by the sign of the disturbance about the convective flow direction. The orientation accuracy of ISIS-2 satellite was ~0.1° which materia-

lizes records of field vector deviation ～3'. The data thus obtained give evidence for the reversive convection change in the polar cap under the northern component of IMF. Figure 5 shows the dependence of disturbance ΔB_x on the vertical component B_z IMF built up on data from ISIS-2 for the polar cap.
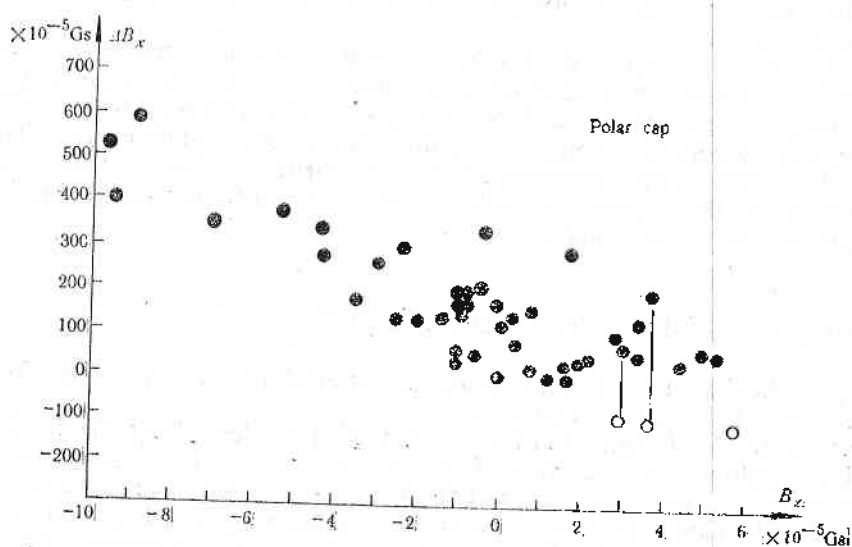
Fig. 5. Magnetic field disturbances dependence (ΔB_x) on (B_z) value and sign

The nature of this dependence is similar to laboratory experiments (Fig. 1) but naturally the statistics of the negative ΔB_x corresponding to tail convection is significantly lower here. Anyway, it should be considered that such picture, constructed on magnetic data only, is somewhat idealized and the directional change of the field line depends on the ionospheric conductivity which may vary incontrollably. Therefore, data obtained from ISIS-2 require additional support based on simultaneous electric and magnetic measurements.

An important feature of the results obtained on board TRIAD and ISIS-2 satellites from measurements of the magnetic field disturbances is the dependence of their sign on the sign of B_y in the noon sector (10:00-15:00 MLT). The sign of the magnetic disturbance due to field-aligned currents is such that plasma convection in the polar casp region appears mainly westward when $B_y > 0$ and eastward when $B_y > 0$ (Fig. 3). Currents available here are predominantly oriented upward from the northern polar cap for $B_y > 0$ and downward for $B_y < 0$. We should note that currents in the region of the noon meridian built up upon data from TRIAD satellite are different from the picture obtained by ISIS-2. It is seen in Fig. 4 that unlike the scheme built up with the TRIAD measurements, the scheme obtained by ISIS-2 depicts all currents in the casp region to flow either upward $(B_y > 0)$ or downward $(B_y < 0)$ — north polar cap. There are other differences, e. g. a Canadian team analysing data from ISIS-2 have found clear correlation between B_y value and the values of the field-aligned currents in the region of the polar casp while this fact has not been observed by others. Thus field-aligned current distribution, especially in the region 12:00 and 24:00 MLT, is not well studied yet. Poorly studied is the fine structure of the currents themselves. Measurements from satellite with

13

circular polar orbit are needed for various longitudes in the polar ionosphere, the orbital height should be $\geq 10^3$ m, so that the satellite should be located considerably higher than the system of ionospheric currents.

Simultaneous measurement of electric and magnetic fields in the polar ionosphere should be carried out together with measurements of the interplanetary magnetic field. The operation of one or better of several satellites on ecliptic orbit is required for such measurements with apogee of more than 20 R_s (e. g. Prognoz-type satellites).

Interpretation accuracy of electric and magnetic field measurements should be controlled by direct determination of drift velocity of cold plasma. A retarding potential analyser on board the satellite can measure the vector sum of drift velocities and the spacecraft. Simultaneous measurements of angular and energy characteristics of magnetospheric precipitated charged particles allows for the correct determination of the topological link between the different magnetospheric regions and the polar ionosphere.

3. Anomalous Resistance and Double Layers

Problems on field-aligned electric fields and anomalous resistance are directly attached to the field-aligned currents.

Considerations of high mobility of charged particles along the field and the equipotentiality of the magnetic field lines are not always correct. Usually two reasons for violation of the equipotentiality are underlined: (1) anomalous increase of resistance when the electron current velocity reaches certain critical value; (2) formation of self-sustained electric charge distribution of double electric layer type. Both mechanisms of significant potential drop were observed in laboratory conditions and were considered in theoretical works. They result in significant potential drop within limited sectors and when precipitated particles appear.

Kindel and Kennel [11] have initially discussed in detail the problem of stability of field-aligned currents with regard to excitement of plasma waves in the auroral zone. Basic factors responsible for the generation of anomalous resistance at altitudes of ≥ 1000 km are the ion-acoustic instability and the ion-cyclotron wave instbility. In terms of ion-acoustic instability it is well known that in plasma with $T_e \gg T_i$ the critical drift velocity appears when the instability is $v_{кр} \sim 4\sqrt{2T_i/m}$. In isothermal plasma the threshold increases up to $v_{кр} \sim \sqrt{2T_e/m}$ as Landau damping for ions becomes very strong. Characteristic frequencies of these waves $\omega \simeq \Omega_{pi}$ correspond to wavelenght of the order of Debay radius. But as already shown by Kindel and Kennel, within a large range of electron and ion temperature ratios (e. g., in hydrogen plasma for $0.1 \leq T_e/T_i \leq 0.8$) the threshold of excitation for the electrostatic ion-cyclotron waves is lower than the corresponding threshold of the ion sound. For example, at $T_e \sim T_i v_{кр} \sim 13\sqrt{2T_i/m}$. When the ion-cyclotronic threshold of the instability is attained, waves of frequencies slightly exceeding the cyclotronic frequency are generated ($\omega \sim 1.2\Omega H_i$ for $T_e \sim T_i$ and $\omega \sim 1.5\Omega H_i$ for $T_e \gg T_i$). Transverse wavelength of such occilations is of the order of the Larmour ion radius and the field-aligned ~ 10 Larmour radii. With the increase of current velocity the next harmonics are excited. It is interesting to note that the insertion of heavy ions into the light hydrogen plasma shock waves. Other bursts of the ion-cyclotron noise clearly correlate with electron fluxes (0.074-5.04 KeV) and turbulence field-aligned electric fields. It is interesting to note that one

14

of the antennas on the S3-3 satellite could operate in Langmuir probe regime and this enables to receive the density fluctuations spectrum. Four maxima are clearly seen approximately at the ion-cyclotron frequency fH^+ and its harmonics. As far as f_{max}, T_e/T_i can be evaluated directly from the dispersion
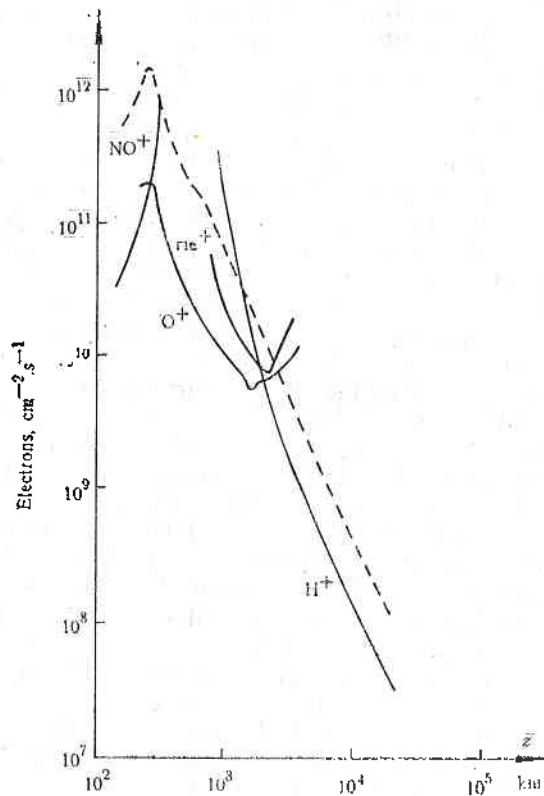
Fig. 6 Critical current dependence of height
- - - - - ion sound

ratio of ion-cyclotron waves. This is ≥ 1. Noise level $\varepsilon = \frac{E^2}{8\pi n T_e} \sim 7\ 10^{-4}$. Anomalous resistance calculated on the measured ion-cyclotron fluctuation level $\eta \sim 10^{2\Omega}/m$ (for comparison we shall note that the value of the classic Coulombs resistance is $10^{-3\Omega}/m$, i. e. by 5 orders of magnitude lower). Thus the field-aligned electric field can be evaluated by $E = \eta j$ ($i \sim 10^{-5} a/m^2$). It is $\sim 1mV/m$ i. e. if an anomalous resistance exists in several thousands of kilometres, it is easy to obtain potential drop along magnetic field line of several kilovolts, which is sufficient to explain accelerations of auroral particles observed.

We have to consider that ion-cyclotron turbulence was observed only at height of $\geq 2,000$ km. This could be related with the fact that at lower heights the critical current velocity was not attained, to excite ion-cyclotron turbulence at the harmonics of ion hydrogen cyclotron frequency. At heights of 1,000 km, as seen in Fig. 6, the ion-cyclotron turbulence should be excited first at frequencies corresponding to heavier ions, i. e., oxygen ions, i. e. lower frequencies of 2-10 Hz. The instruments on board S3-3 could record electric fluctuations only

15

with frequencies of $\geq$30-50 Hz. That is why measurements of AC electric fields at lower frequencies are necessary in order to understand whether waves of frequencies of $n\dfrac{eH}{M_o{}^+c}$ are excited at heights $\sim$1,000 km, decreases the thershold of ion-cyclotron instability and increases the range of electron and ion temperature ratio, at which ion-cyclotronic turbulence is still dominant. Roughly speaking, the critical drift velocity in multicomponent plasma with respect to the ion sound is basically defined by light ions, while for the ion-cyclotron waves this is performed by the heavy ions. The initial excitation of ion-cyclotron waves starts at frequencies corresponding to the cyclotron frequencies of heavier ions O^+, followed by He^+ and H^+. This is well seen in Fig. 6, where critical current values are shown, exciting various types of waves depending on altitude. At low current density, the ion-cyclotron waves with frequencies corresponding to cyclotron frequencies of hydrogen ions are excited at heights higher than 1,000 km. When the current density increases, the region of instability descends until excitation of waves corresponding to heavier component — oxygen ions — begins. Which are the real current density values? For instance, in situation of a "calm" magnetosphere, the maximum currents were observed in the current system of type (1) within the region 7-8 hrs. MLT (10^9 electrons. cm^{-2} s^{-1}), i. e. practically such currents may easily excite an ion-cyclotron turbulence. Recent measurements of electric fields and the density fluctuation on board S5-3 satellite had confirmed these conclusions [12-13]. On board S3-3 the fields were measured in the range 0.5-16 KHz with wide band receiver (ion-cyclotron frequency corresponding to the hydrogen ions is of the order of 100 GHz). The ion-cyclotron turbulence was observed in large interval in the local time but as a rule on L-shelves [6] only. The typical duration of such phenomena is $\sim$5 s ($\sim$35 km) which corresponds to scale of $\sim$10 km in the lower ionosphere. Maximum noises were attached to large ($\geq$120 nV/m) field-aligned electric fields in the so-called electrostatic where $n=1,2,...,$ or the turbulence source is located in fact at higher altitudes. Ion-cyclotron turbulence could be excited not only by field-aligned current electrons, but also by ion fluxes. It is quite possible for both mechanisms to operate. Therefore, simultaneous measurements of field-aligned currents, ion fluxes and electric noises would help to understand better the reasons of ion-cyclotron waves generation. In such a complex of measurements quite important are measurements in directions transverse to the magnetic field as far as the ion-cyclotron waves in a resonant way accelerate ions perpendicular to the field. According to the theory given in [14], the energy acquired by them could exceed 0.5 keV. Ion acceleration transversely to the field was actually observed on S3-3 satellite [15]. We shall also consider that modes correspondent to oxygen ions are difficult to identify as the phase velocity of these waves is about an order of madnitude lower and that is why the Doppler shift due to satellite motion would result in spectral enlargement.

Peculiarities in electron precipitation distribution from inverted V-type observed as early as Injun-5 experiment, and also O^+ and H^+ fluxes of ionspheric origin accelerated to energies of several keV moving upward along the field lines, seemed to be interpreted in terms of simple existence of field-aligned electric fields and anomalous resistance. At the same time, the value of field-aligned electric fields required to supply the observed potential drop have to be of the order of several mV/m.

Data from measurements performed on board S3-3 satellite obviously give considerably larger values — about several hundreds of mV/m (Fig.7). This

value should be considered carefully as far as the error in the angular resolution of the antenna at strong field-aligned electric fields could significantly augment this value. If such electric fields really exist, it is already impossible to interpret them with the anomalous resistance effects (AC electric fields in
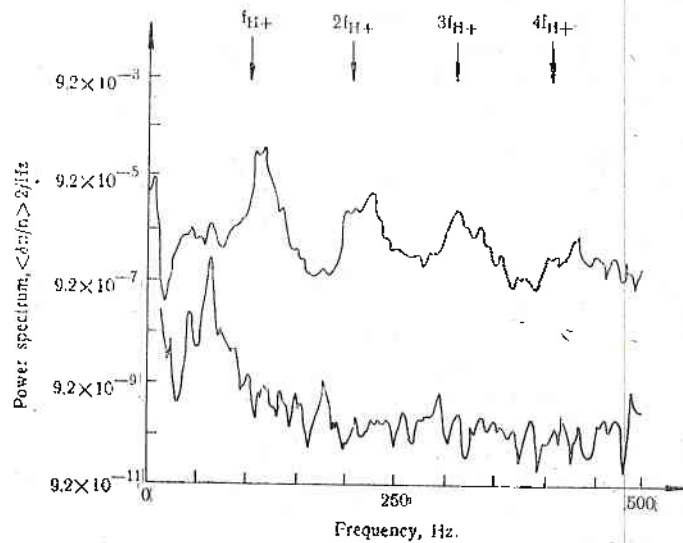
Fig. 7. Energy spectrum of ion-cyclotron turbulence as measured on board S3-3 satellite

such case have to attain values of about tens of V/m, which exceeds significantly the level of recorded noises). Obviously they are related to the formation of so-called double layers in the plasma. Double layers were discovered by Langmuir some 50 years ago in studies of gas discharges. Similar to the phenomenon of anomalous resistance, the double layer generates only when the current density starts to exceed some threshold values. In double layers observed in the magnetosphere, the low-potential boundary of the layer is further from the Earth than the high-potential one. Passing through the potential jump in the double layer, the electrons are enhanced in one direction and the ions in another. In order to generate a double layer, rather specific charged particles distribution is required. Their trajectories should be such as to enable abundance of one charge compared to the other at the double layer boundaries.

In the theoretical models of double layers the problem of distribution of charged particle populations is very important (as a rule in theoretical works only steady-state solutions are considered, i. e. the self-consistent problem is rather complicated).

Obviously the model of thermal electron and ion distribution, where ionospheric ions move upward and hot electrons move earthward, is most reasonable for the magnetosphere. But the problem of how the particle distribution functions are built to generate a double layer is still unclear. At present not only the evolution of distribution functions is not studied, but the same refers even to the steady-state charged particle distribution. The problem of what reflects upward acceleration of ions and provides for positive charge excess

at low double layer boundary is still open. Whether they are back-scattered at ion-cyclotron fluctuations or at higher altitudes, double layers of reverse charge distribution are formed at its boundaries. It is not clear why often in measurements of field-aligned electric fields double structures are observed. Is this a simple result from equipotential short-circuit generated along the double layer field lines or a result from two double "steep" layers formation (ion-cyclotron shock waves)? It is hard even to predict whether anomalous resistance or double layers would result from field-aligned current instabilily. Therefore, further study on double layers is required, based on three-component electric field sensors and charged particle detectors, on board satellites on polar orbit.

Besides ion-cyclotron and ion-acoustic fluctuations responsible for the generation of anomalous resistance and electrostatic shock waves (double layers), rather interesting are emissions in the region of the low hybrid resonance and also Whistler mode controlling electron distribution in the earth radiation belts and various types of hydromagnetic fluctuations excited in auroral regions by the ring current precipitated particle fluxes.

We should pay attention to measurements of the so-called high latitude turbulence (HLT) characterized with wide band low-frequency spectrum (< 500 Hz) and observed in auroral regions at all MLT. This turbulence is obviously attached to Kelvin-Helmholtz instability generated at plasma flows of heterogeneous velocity profile [16]. Although HLT-turbulence is pretty thoroughly studied on board OVI-17, S3-3 and Hawkeye satellites, simultaneous measurements of plasma drift variations and electrostatic noises would enable the better understanding of suggested cascade mechanisms of this turbulence [17].

4. Stable Auroral Red Arcs

The importance of ring currents in dynamic ionospheric-magnetospheric interactions comes from the amount of energy stored in this region ($\sim 10^{23}$ ergs). Even if a small portion of this is given to the ionosphere, it could result in a spectacular change in the ionospheric situation. Simultaneous measurements of emission spectra of the upper ionosphere, charged particles fluxes and electromagnetic waves would permit to clarify series of important regularities in such effects. In particular, these measurements would help to understand the nature of red arcs generated at latitudes corresponding to $L=2-4$ [18]. Sub-auroral red arcs appear in the recovery phase of the geomagnetic storm. According to the generally accepted viewpoint, these emissions (mainly oxygen line — 6,300 Å) are generated by heated electrons. The mechanism of electron heating is generally attached to ring current dissipation. During the recovery phase the ring current is located deeper in the plasmasphere [19]. When the plasmasphere is filled with sufficient amount of ring current ions, this generates the electromagnetic ion-cyclotron turbulence. Scattered at ion-cyclotron waves, ions fall into the loss cone and precipitate downward. In its turn, the ion-cyclotron turbulence could heat thermal electrons from the plasmasphere at the expense of Landau dumping. Experimental data [20] are available, which show that simultaneously with the increase of ring current the ion-cyclotron waves are to be observed. Together with this, dramatic change in the pitch angle distribution of ring current particles takes plase (it becomes anisotropic). But regardless of the fact that this theory correctly predicts red arcs location, it does not explain how the energy transferred to electrons is transported from the equatorial regions, where the heating takes place, downward to the iono-

sphere. For example, electrons heated at the plasmasphere boundary up to ~10 eV could become trapped by the magnetic field (collision frequency ~$10^{-5}s^{-1}$), therefore a process resulting in their precipitation is required. We should also note that on board S3-3 satellite only 18 events were recorded, which may be identified as ion-cyclotron turbulence as some of them were not accompanied by any change in pitch angular distribution of ions [21]. On board Hawkeye-1 only 5 such events were observed in 18 months period, although in 14 cases when considerable weakening in D_{st} (-25γ) was observed, no ion-cyclotron turbulence was recorded [22].

In [23] another mechanism of electron heating is suggested. This is attached to the kinetic Alfven waves dissipation. Such waves (of transverse to the magnetic field wavelength of the order of the ion Larmour radius) could be excited at the expense of conversion from MHD-surface waves. Field-aligned electric fields existing in these waves could heat cold electrons by resonance mode ($V_A - 1.7 V_{T_e}$). Heating is of local nature along L-shelves since its velocity rapidly decreases moving away from the resonance. Such a mechanism provides for direct precipitation of heated electrons, since the wavelength along the field line is comparable to the field tube length itself. Indirect support to this mechanism was obtained with ground-based magnetic measurements [24]. Large fluxes of precipitated electrons (~20 eV) were also reported in [25]. Thus various hypotheses interpreting red arcs are available. For the proper understanding of their generation mechanism, it is necessary to perform complex simultaneous measurements on polar orbit satellite on precipitated particles fluxes, wave measurements, space scanning of red line emissions. In order to obtain information on the ring current situation, the operation of another satellite is required as its orbit should cross the region of the ring current — plasmasphere at low latitudes. Very important are the ground observation of magnetic field pulsation.

5. Active Experiment

Recently, the mechanisms of particle filling and decay of the ring current are intensively studied. Important information on decay mechanism should be given by the experiment of forced particle precipitation, the point being that the ring current is in thermodynamic unsteady state and plasma injection could become a triggering mechanism resulting in particle evacuation to the atmosphere and therefore to excitation of aurora.

When compact plasma beam is injected into the magnetosphere, particles precipitation could be activated due to two reasons: (a) magnetic field distortion; (b) wave excitation and particle velocity vector shifted to the loss cone at the expense of resonance wave-particle interaction. In the second case, precipitation would appear after plasma filling in the respective field tube. Complex of wave measurements would enable the separation of these processes. The records of artificially excited aurora should be effected on board the satellite together with ground photographic and radiolocation means.

Compact plasma beam may be obtained by pulse electrodynamic accelerator. Such accelerators have been designed in the USSR as early as 1958 for the purposes of thermonuclear studies and are largely used recently in various technical fields, including spacecrafts. If barium is selected as operation material, we may observe the whole injection process after the beam injection near the terminator including the delicate effects of the beam and the magnetic field interactions. These observations could happen to be of unique nature

since such experiments are difficult to be performed in laboratories due to the chamber wall effects. Ground observations of injections are possible at total quantity of injected particles $10^{19} \div 10^{20}$ cm^{-3}.

In order to avoid the negative effects of accelerator pulses on the proper functioning of the other instruments, it is useful to perform injection after the accomplishment of the geophysical experimental program.

6. The Midlatitudinal Trough

Specific for the upper ionosphere is the existence of sufficiently narrow regions of low ion density. Recently the morphology of such troughs (mid-and high-latitude) and their interaction with the plasmapause and the polar casp are thoroughly studied. The interpretation of these specifics, in agreement with observation data available, is not yet obtained. In accordance with some hypotheses, a very important role in trough formation is played by the electric fields generating plasma convection. Ion drift with respect to neutrals spectacularly increases the velocity of some plasmachemical reactions, e. g. the density of molecular ions [26] increases due to $O^+ + N_2 \rightarrow No + N^+$. Molecular ions in their turn quickly recombine and the total ion density lowers. There is another hypothesis for the trough formation given in [27]. Insofar as plasma convection at ionospheric heights is defined both by electric fields, generated by

Fig. 8. Scheme of generation mechanism of the midlatitudinal trough. In the D-region the flux is defined by the electric field, while in the A-region it is determined by the field related to the earth rotation. In the intermediary regions B and C the flux direction changes from east to west. The "stagnation" region — E-W velocity component becomes zero.

solar wind interactions with the magnetosphere (effects of recombination and viscousity), and by electric fields related to planetary rotation, the resultant convection pattern (Fig. 8) could establish particular regions of very slow plasma motion on the night side. Since plasma in these regions is maintained for a long time, recombination processes decrease significantly the ion density. Simultaneous measurements of plasma convection with electric field and ion drift sensors, together with mass-energy analyser of thermal plasma in the trough regions, would enable the understanding of the nature of these interesting features.

7. Electric Fields in the Equatorial Ionosphere

We should pay attention to electric field measurements in the equatorial ionosphere, since recent experimental data provide evidence on the interactions between the electric field at ionospheric heights and the orientation of the interplanetary magnetic field [28, 29]. The electric field in the magnetospheric tail is usually oriented from morning to evening side (this field is either projected in tail by the solar wind or is induced by viscous plasma — field inter-

20

action at the magnetospheric boundary). In a stationary situation the electric field cannot penetrate into the plasmasphere due to the screening effect of polarizing charges formed near its boundary. However, the variations of this field with the characteristic time of ≤ 1 hour could be observed deep into the plasmasphere. For example, the fast sign change in IMF from the stable south direction to the north generates anomalous turn in the zonal equatorial electric field. The interpretation of this very interesting effect could be related with the fact that such change of IMF vector direction leads to the decrease of the electric field in the polar cap and possibly changes its sign, therefore that happens inside the magnetosphere too. Screening charges in the plasma layer boundary cannot redistribute so fast, which results in electric field orientation from evening to morning side inside the plasmasphere. There are data showing dependence of the electric field on the B_y component of IMF, for the equatorial ionosphere. Such relationship between IMF and convection in the magnetosphere, on the one hand, and the processes taking place deeply into the plasmasphere, on the other, are quite intriguing and require thorough study. Drift measurements of charged particles and electric fields at low latitudes and the comparison with IMF data will give a key to the solution of this problem.

8. Altitudinal Thermal Plasma Distribution

Problems referring to thermal plasma distribution along field tubes are of particular interest, together with relations between ionosphere and plasmasphere. In daytime thermal proton fluxes from the ionosphere fill up the plasmasphere field tubes. During the night the recombination processes become predominant and the energy stored in the plasmasphere feeds back into the ionosphere, i. e. fluxes from the plasmasphere maintain the existence of the F-layer. The link between these two regions has a dynamic character. For instance, during magnetospheric disturbances, plasmaspheric field tubes may convect to the far magnetosphere where they lose their plasma content. Pressure gradients generated at this process in the "empty" tubes must create large plasma flow from the ionosphere similar to the polar wind, which refills the plasmasphere. The plasma flow induced in this way may be superimposed by a flow induced by the interaction of the F-region ionosphere with neutral winds. The neutral wind forces the ions to move along magnetic field lines. Depending on the magnetic inclination, the velocity component of the neutral wind along the field line should be different. This could result in lifting or descending ionization in the F-layer. Thus, for instance, an equatorward meridional wind in the northern hemisphere will result in altitudinal increase in the F-layer until the drag force between ions and neutrals is not balanced by the earth gravity, density gradient and polarization fields. Usually the time required for establishing the diffusive equilibrium in a given field tube is much smaller than the characteristic time of wind system variations in the F-region, therefore we may suggest that the shift of the F-layer will result in a corresponding increase and decrease of the ion density at heights of 1,000 km [30]. This means that the global measurement of the ion density at heights well above the F-layer maximum are important for the studies of large-scale air mass transfer in the night midlatitudinal F-region. In order to avoid effects of altitudinal change in the ion density, it is necessary to have a circular orbit satellite.

Basic difficulty in the interpretation on the experimental data is the necessity to select effects related to the different behaviour of O^+ and H^+ density. As shown in [30], the sharp decrease of the boundary above which the H^+

ion density slightly changes with the altitude, is observed during the night at magnetic latitudes of ±30°. The boundary at these latitudes is located at height of ~600 km. It appears that the ion density is approximately the same at both ends of the field tube at 1000 km where the invariant latitude is Λ = 30-50°, independent of how low the O⁺ ion density is. This brings to the idea that H⁺ ion in distribution along magnetic field lines is controlled by equalizing the pressure along the entire field tube and does not depend severely on O⁺ and H⁺ interactions in the ionosphere. Such conclusion means that measurements at heights of about 1,000 km of H⁺ density reflect the dynamics of plasmasphere rather than that of the ionosphere.

9. Equatorial Anomaly

Figure 9 illustrates light ion distribution at 1,000 km at night [32]. It is well seen that the distribution of hydrogen ions is bi-maximal. Minimum H⁺ density is to be found in the equatorial region. Hydrogen ion density falls sharply after ~40° latitude, forming the equatorial boundary of the midlatitudinal trough of light ions. The anomaly appears also in the ion composition and temperature. Such minimum and two maxima in the equatorial F-region are formed in afternoon hours as a result of two effects — $E \times B$ drift due to E-W electric field and plasma diffusion in meridional direction along the magnetic field tubes. This is familiar as "fountain" effect. But the theory of nighttime equatorial anomaly formation and its dynamic should not be considered accomplished yet. In particular, the equatorial anomaly property largely depends on longitude. Longitudinal variations of equatorial ionosphere result from upward and downward plasma motion effects. In their turn, the latter to a
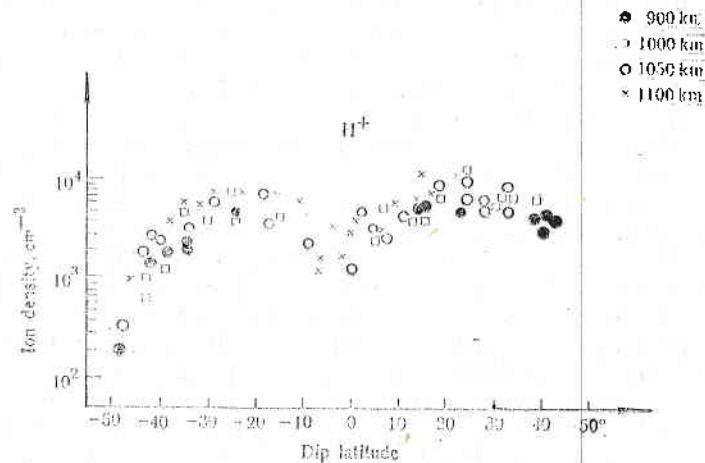
Fig. 9. Light ions distribution at height of ~1,000 km from latitude

large degree are determined by the neutral winds. Simultaneous measurements of electric fields, electron and ion density distribution and velocity of charged particles drift on board polar orbit setellites would enable the better understanding of the entire complex of sophisticated interacting factors.

22

10. Circulation in the Thermosphere

Certain ionospheric phenomena are directly linked to winds in the upper atmosphere. Interaction between solar wind and atmosphere is effected by two basic mechanisms: (1) auroral particle precipitation; dissipation of ionospheric current systems. These processes take place in general at high-latitude atmosphere, while ultraviolet heating has maximum at the subsolar point. The relatively constant heating by the solar uv generates thermospheric circulation which is the reason of the global wind system generation at heights of 100 km, described in [33, 34]. The Joule heating and heating from precipitated particles due to the above-mentioned process results in generation of a secondary wind system of variable equatorial boundary in dependence on the magnetic activity. Typical circula-
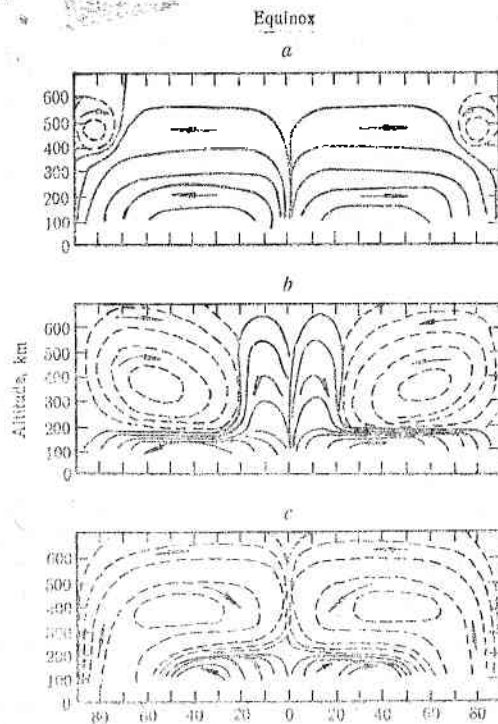
Fig. 10. Diagram of the zonal mid-meridional circulation in earth thermosphere for the equinox period with reference to various levels of auroral activity (a) extremely calm geomagnetic activity, (b) average activity (10^{18} erg. S^{-1}) and (c) geomagnetic storm (10^{19} erg. S^{-1}). The contours illustrate schematically the mass flux and the arrows show the motion direction

tion pattern in the meridian plane is shown in Fig. 10 [33, 34, 35, 36]. The formation of a secondary wind system oriented from high to low geographic latitudes may be due to the fact that the heating in high-latitude regions becomes comparable to the solar ultraviolet heating [37].

23

In equinox periods the circulation due to solar ultraviolet is manifested by upward motion over the geographic equator with a subsequent poleward streaming. The secondary circulation due to auroral heating has a reverse direction - - from the pole to the equator and its equatorial boundary depends on the energy supplied into the atmosphere. During magnetic substorms the normal circulation is constrained only to heights lower than 150 km and to low and mid-geographic latitudes.

During the solar solstice the circulation due to the solar ultraviolet has direction from summer to winter hemisphere. Auroral atmospheric heating gives rise to circulation from pole to equator in the winter hemisphere. Its equatorial boundary shifts depending on the degree of the magnetic disturbance. In the summer hemisphere the circulation is maintained at its normal state. The changes described above are the major motions of thermospheric circulation in which the Eerth upper atmosphere is involved during magnetic distrubances. Many small-scale motions are also observed.

Investigations of the three-dimentional circulation of thermosphere under various levels of solar and magnetic activity are still in their initial phase. The complete understanding of these processes would permit the evaluation of the ionospheric effect on circulation. Simultaneous measurements of the differential charge particle spectrum and the dissipation of current systems would enable the definition of total energy flux at subauroral and auroral latitudes. A possibility to establish a model of earth atmospheric circulation emerges from combined data on air-glow emissions [38].

11. Plasma Irregularities in the Ionosphere

Measurements performed on board satellites [32, 39] enabled the discovery of irregularities in the ionospheric plasma at relatively high latitudes. The spatial sizes of these irregularities range between 30 and 50 km. These irregularities play an important role for the problem of spaceborne radiocommunications. Particularly interesting is the shortwave irregularities phenomenon (10-100 km). In order to measure irregularities in ionospheric plasma density, the application of Langmuir probes may be useful. It is substantial to understand the main mechanisms of irregularity generation. Particularly large irregularities are observed in the region of the midlatitudinal trough which could result, for instance, from large gradients and strong electric fields triggering the generation of various types of plasma irregularities. Still open is the problem of nteractions between midlatitudinal trough dynamics and the equatorial boundary of the high-latitude irregularities. Simultaneous measurements on thermal plasma and electric fields on board polar satellite of circular orbit may help to obtain the answer to these questions. Very important is the study of irregularities in the equatorial ionosphere. The nonreliability of satellite communication systems contributes to the increased interest toward this phenomenon. VHF-signals emitted by satellites and received on earth are largely deformed in the equatorial region.

Conclusion

The data presented in this work clearly show that the launch of satellites with circular polar orbits at heights of about 1,000 km would permit to solve a series of important problems related to phenomena in interplanetary medium, magnetosphere, ionosphere and earth atmosphere.

24

References

1. Cauffmann, D. T., P. A. Gurnett. — Space Sci. Rev., **13**, 1972, 369.
2. Heppner, J. P. Initial Problems of Magnetospheric Physics. Ed. E. R. Dyer. Washington, IUCSTP, 1972, p. 107.
3. Heelis, R. A., W. B. Hanson, J. L. Burch. — J. Geophys. Res., **81**, 1976, 3803.
4. Дубинин, Э. М., И. М. Подгорный, Ю. Н. Потанин. — Космические исследования, **15**, 1977, с. 866.
5. Podgorny, I. M., E. M. Dubinin, Yu. N. Potanin. — Geophys. Res. Lett., **4** 1978, p. 207.
6. Mozer, F. S., W. D. Gonzales, F. H. Bogotl, M. C. Kelley. S. Schutz. — J. Geophys. Res., **79**, 1974, p. 56.
7. Burke, W. L., M. C. Kelley, R. C. Sagalyn, M. Smiddy, S. T. Lai. — Geophys. Res. Lett., **6**, 1979, p. 21.
8. Crooker, N. U. — J. Geophys. Res., **84**, 1979, p. 951.
9. McDiarmid, I. B., J. R. Burrows, M. D. Wilson. — J. Geophys. Res., **83**, 1978, p. 681.
10. McDiarmid, I. B., J. R. Burrows, M. D. Wilson. — J. Geophys. Res., **84**, 1979, p. 1431.
11. Kindel, J. M., C. F. Kennel. — J. Geophys. Res., **76**, 1971, p. 3055.
12. Mozer, F. S., C. W., Carlson, M. K. Hudson, R. B. Torbert, B. Parady, J. Yatteau, M. C. Kelley. — Phys. Rev. Lett., **38**, 1977, p. 292.
13. Kintner, P. M., M. C. Kelley, F. S. Mozer. — Geophys. Res. Lett., **5**, 1978, p. 139.
14. Lysak, R. L., M. K. Hudson, M. Temerin. — J. Geophys. Res., **84**, 1979.
15. Sharp, R. D., R. G. Johnson, E. G. Shelley. — J. Geophys. Res., **82**, 1977, p. 3324.
16. Kintner, P. M. — J. Geophys. Res., **81**, 1976, p. 5114.
17. Kelley, M. C., P. M. Kintner. — Ap. J., **220**, 19, p. 330.
18. Hoch, R. J., C. R. Batishko, K. C. Clark. — J. Geophys. Res., **76**, 1971, p. 6185.
19. Chappel, R. C., K. K. Harris, G. W. Sharp. — J. Geophys. Res., **76**, 1971, p. 2357.
20. Lundblad, J. A., F. Soraas. — Planet Space Sci., **26**, 1978, p. 245.
21. Taylor, W. W. L., L. R. Lyons. — J. Geophys. Res., **81**, 1976, p 6177.
22. Kintner, P. M., D. A. Gurnett. — J. Geophys. Res. **82**, 1977, p. 2314.
23. Hasegawa, A., K. Mima. — J. Geophys. Res., **83**, 1978, 1117.
24. Lanzerotti, L. J., A. Hassegawa, C. F. MacClennau. — Planet Space Sci., **26**, p. 777.
25. Shepherd, G. G. — EOS Trans. Am. Geophys., **58**, 1977, p. 481.
26. Schunk, R. W., W. J. Raitt, P. M. Banks. — J. Geophys. Res., **80**, 1975, 3121.
27. Spiro, R. W., R. A. Heelis, W. B. Hanson. — J. Geophys. Res., **83**, 1978, p. 4255.
28. Kelley, M. C., B. G. Fejer, C. A. Gonzales. — Geophys. Res. Lett., **6**, 1979, p. 301.
29. Galperin, Yu. I., V. N. Ponomarev, A. G. Zosimova. — J. Geophys. Res. **83**, p. 4265.
30. Bailey, G. J., R. I. Moffett, J. A. Murphy. — Planet Space Sci., **25**, 1977, p. 967.
31. Kutiev, I., R. Heelis, S. Sanatany. — J. Geophys. Res., **85**, 1980, p. 2366.
32. Серафимов, К. Космические исследования в Болгарии. С., БАН, 1979.
33. Blum, P. W., I. Marris. — Space Research, XIII, 1973, p. 369.
34. King-Hele, D. G., D. M. C. Walker. — Planet. Space Sci., **25**, 1977, p. 313.
35. Roble, R. G. The Upper Atmosphere and Magnetosphere. Report of the National Research Council. Washington D. C., 1977.
36. Dickinson, R. E., E. C. Ridley, R. G. Roble. — J. Atmosph. Sci., **34**, 1977, p. 178.
37. Banks, P. M. — J. Atmos. Terr. Phys., **39**, 1977, p. 179.
38. Bittencourt, J. A., B. A. Tinsley. — J. Geophys. Res., **81**, 1976, p. 3781.
39. P. L. Dyson, J. P. McClure. — J. Geophys. Res., **79**, 1974, p. 1497.

О некоторых проблемах геофизики, решаемых с помощью спутников на полярных орбитах

В. М. Балебанов, М. М. Гогошев, Е. М. Дубинин, И. С. Кутиев, И. М. Подгорни, К. Б. Серафимов

(Резюме)

Рассматривается возможность установления зависимости между конвекцией магнитосферной плазмы и магнитным полем посредством измерения электрического и магнитного полей и регистрации плазменного дрейфа.

Такие эксперименты могут быть выполнены на спутниках на полярных орбитах как с целью выявления конвекции в области магнитной шапки, так и для изучения явления в экваториальных районах и термосферной циркуляции.

Statistical Relationship between Aeronomic and Geophysical Parameters for the South Atlantic Geomagnetic Anomaly Region

T. K. Yanev, D. N. Mishev, M. G. Gerdjikova, N. D. Pelova

The examination of the results from the systematic observations on aeronomic and geophysical parameters in the South Atlantic Region results in the conclusion that the region westward from the mid-Atlantic ridge is of particular interest to meteorology and geophysics. This is based on the analysis of 35 parameters for which data were provided by meteorological, geophysical and space observations: (1) average atmospheric temperature of the contact layer — summer; (2) average surface water temperature; (3) deficit of irrigation point more than 850 mb; (4) deficit of irrigation point more that 500 mb; (5) average air pressure of the contact layer — summer; (6) mean air temperature $h = 10$ km — summer; (7) mean air pressure $h = 10$ km — summer; (8) average annual air temperature $h = 10$ km; (9) average annual air pressure $h = 10$ km; (10) total cloudiness; (11) northern component of the geomagnetic filed X $h = 0$ km; (12) eastern component of the geomagnetic field Y $h = 0$ km; (13) vertical componet of the geomagnetic field Z $h = 0$ km; (14) geomagnetic field intensity $H h = 0$ km, (15) northern component of the geomagnetic field $X h = 10$ km; (16) eastern component of the geomagnetic field $Y h = 10$ km; (17) vertical component of the geomagnetic field $Z h = 10$ km; (18) geomagnetic field intensity $H h = 10$ km; (19) northern component of the geomagnetic field $X h = 350$ km; (20) eastern component of the geomagnetic field $Z h = 350$ km; (21) vertical component of the geomagnetic field $Z h = 350$ km; (22) geomagnetic field intensity $H h = 350$ km; (23) velocity of charged particles precipitation from space; (24) northern component of nondipole geomagnetic field $X' h = 0$ km; (25) eastern component of nondipole geomagnetic field $Y' h = 0$ km; (26) vertical component of the nondipole geomagnetic field $Z' h = 0$ km; (27) nondipole field intensity $H' h = 0$ km; (28) northern component of nondipole geomagnetic field $X' h = 10$ km; (29) eastern component of nondipole geomagnetic field $Y' h = 0$ km; (30) vertical component of the nondipole geomagnetic field $Z' h = 10$ km; (31) nondipole geomagnetic field intensity $H' h = 10$ km; (32) northern component of nondipole geomagnetic field $X' h = 350$ km; (33) eastern component of the nondipole geomagnetic field $Y' h = 350$ km; (34) vertical

component of nondipole geomagnetic field Z' $h=350$ km; (35) nondipole geomagnetic field intensity H' $h=350$ km.

In this paper relationships characterizing various in nature processes are studied. In general, these are meteorological elements (temperature, pressure) components of the geomagnetic field — observed and nondipole, characteristics of phenomena resulting from the solar activity.

The data on these parameters are statistically processed. This comprises the determination of correlative and regressive dependences between topographic changes of the geophysical parameters studied. The procedure is performed with statistical models and essentially represents a model problem (regressive model) but in this case the model is formally mathematical. Its parameters do not have direct physical interpretation. The efforts when applying the model were to obtain the intervals within which the average values of the regression line, which expresses the functional relationship between the studied parameters, are defined with given confidence level. The selection of the parameters aimed at better representativeness of the analysed relationships, i. e. better characterization of the processes and phenomena observed. Nevertheless, data on single parameters do not refer to one and the same above sea level height. Therefore, changes of the temperature and the dry air pressure, as well as of the components of the geomagnetic field are taken into account at heights of: $h=0$ km (sea level), $h=10$ km (average bottom boundary of the troposphere), and $h=350$ km (spacecraft trajectory height with reference to measurements for parameter No 23).

Based on the results obtained in [6, 7] and revealing some interesting dependences between the components of the geomagnetic field, on the one hand, and the meteorological elements — on the other, the emphasis of the statistical analysis performed here is placed on the determination of similar relationships and the specification of the ones already defined. As far as the analysis of some dependences between meteorological and geomagnetic field parameters made in [6] shows that some of the relationships obtained are not of particular importance and do not contain qualitatively new information on the processes observed, further discussions would not refer to them. This would be replaced by data which may help to specify and confirm the relationships defined.

In order to collect data on the mentioned parameters, we use the results which in one form or another are already published or at the given initial conditions are computed with reference to the purpose of their application.

The data are calculated and located in the nodes of a 5^0 network. Thus, the source difference does not affect the calculations of the initial data.

The region in consideration is located at the southwestern part of the Atlantic Ocean from 20 to 70° west longitude and from 0 to 50° south latitude. The cartographic calculation of the parametric values is effected as the value of the respective isoline is taken in the nodes of the 5^0 network, and for the case where this is not available, the value is linearly approximated. The succession of the value calculations is selected arbitrarily, but once selected, it is kept the same for the parameters considered. The same procedure is applied for the cases where the data are taken by the respective catalogues or are computed. In this case the calculation is performed with the method of sweep. The parametric values are calculated in 70 points describing the region from the Atlantic Ocean with the above-given coordinates.

Values both for observed and for nondipole geomagnetic fields and used in the analysis of the geomagnetic field component data. The data are obtained as the geomagnetic potential is expanded to a series of spherical harmonic fun-

tions with accuracy up to the 100th term (for the observed geomagnetic field) and the first term of the development representing the dipole geomagnetic field is substracted for the nondipole field.

The parametric data are statistically processed and are studied by linear correlative analysis and correlative ratio.

The results from the linear correlative analysis are elements of the normalized correlative matrix. Each matrix element is a coefficient of the mutual correlation. The degres of fitness of the experimental data for the studied parameters with respect to the straight line is evaluated through the coefficient of the common linear correlation

$$(1) \qquad r_{ij} = \frac{1}{n} \frac{\sum\limits_{l=1}^{n} (a_{il} - \overline{a}_j)(a_{jl} - a_j)}{\sigma_{ai}\, \sigma_{aj}},$$

$$\overline{a} = \frac{\sum\limits_{l=1}^{n} a_{il}}{n}, \qquad \sigma_{ai} = \sqrt{\sum\limits_{l=1}^{n} (a_{il} - \overline{a}_j)/n},$$

where r_{ij} is the coefffcient of mutual correlation between the i-th and the j-th variables, σ_a — standard deviation, σ_{il}, a_{jl} — values observed for the i-th and j-th variables, n — number of observation (number of values observed for a_i and a_j for the case $h = 70$).

The existence of functional dependence between a given couple of variables without revealing the type of this dependence is evaluated by the correlative ratio given in expression

$$(2) \qquad \eta_{ij} = \frac{\sum\limits_{i=1}^{m_i} (a_i - \overline{a})^2 n_i}{\sum\limits_{i=1}^{m}\sum\limits_{l=1}^{n_i} (a_{il} - \overline{a})^2},$$

where $\quad a_i = \dfrac{\sum\limits_{l=1}^{n_i} a_{il}}{n_i}, \qquad \overline{a} = \dfrac{\sum\limits_{i=1}^{m_j}\sum\limits_{l=1}^{n_i} (a_{il})}{n_i}, \qquad n = \sum\limits_{i=1}^{m} n_i$, n is the number of experimental data for a_i and a_j, m_j is the number of intervals of a_j (along the X-axis);

$$m_j = \frac{\Delta_j}{\delta_j},$$

where

Δ_j is the complete interval of a_j variation observed, δ_j is the a_j measurement accuracy (indeterminancy interval of a_j).

For the purpose of this work a polynomial regression model is used, linear with respect to the constants α of the assumed regression between a_i and a_j.

29

$$(3) \qquad \widehat{a}_i = \sum_{l=1}^{Q} {}' a_{il} a_j^{l \text{out}}$$

The set $\{a_j\}$ incorporates components of observed and nondipole geomagnetic fields for heights of $h=10$ km and $h=350$ km, and the set $\{a_i\}$ represents certain meteoelements as average month and annual temperature and pressure for dry air at $h=10$ km and velocity of space charged particle precipitation. The accuracy with which the model $\widehat{a}_i$ describes the availabe experimental data has been determined through Fischer's criterion

$$(4) \qquad F = \dfrac{\sum\limits_{l=1}^{Q} {}' (\widehat{a}_{il} - \bar{a}_i)^2 (n-k-1)}{\sum\limits_{l=1}^{Q} {}' (a_{il} - \widehat{a}_i)^2 k} \;,$$

Table 1

Dependence between parameters Nos	Polynominal power	Fischer's criterion F
6-15	4	24.562
7-15	3	17.217
8-15	4	33.205
9-15	4	16.043
6-16	3	128.984
7-16	3	84.021
8-16	3	138.683
9-16	3	97.467
6-17	3	169.284
7-17	4	194.753
8-17	3	182.982
9-17	4	158.006
6-18	4	41.963
7-18	4	58.854
8-18	4	35.886
9-18	4	56.233
6-28	4	6.312
7-28	3	8.749
8-28	4	3.971
9-28	4	11.025
6-29	2	32.112
7-29	2	26.349
8-29	2	35.652
9-29	1	23.650
6-30	4	457.025
7-30	4	211.722
8-30	1	503.402
9-30	1	204.835
6-31	2	716.24
7-31	2	470.012
8-31	2	813.287
9-31	2	392.186
23-19	1	39.813
23-20	2	21.872
23-21	3	8.212
23-22	4	4.417
23-32	1	18.667
23-33	2	7.688
23-34	3	14.062
23-35	4	14.863

where: $\hat{a}_i$ is the calculated a_i values according to the model, $\bar{a}$ is the average a_i value.

The evaluation of the regression model accuracy is performed under confidence level of $p=0.05$ as $n<100$ and powers of freedom for the numerator equal to the power k of the polynomial and for the denominator $(n-k-1)$.

Resulting from the application of the regression analysis through a step regression from first to fourth power in agreement with equation (3), the form of the best regression models describing the experimental data is obtained. The statistical characteristics of some of them, as polynomial power, Fischer's criterion and regression coefficients are listed in Tables 1 and 2.

As already shown, the major characteristic of the studied regression fitness is the F-ratio. From a theoretical point of view, at $n<100$ the confidence level p cannot be greater than 0.05, regardless of the fact that most of the

T a b l e 2

Dependence between parameters Nos	Regression coefficients				
	a_0	a_1	a_2	a_3	a_4
6-15	—42.7513	—	—	—	1896.4082
7-15	264.1711	—	—	1082.054	—
8-15	—46.7699	—	—	—	2645.8073
9-15	270.0776	—	—	—	3172.8139
6-16	—44.0839	—	—	—21451.13	—
7-16	263.4516	—	—	—43705.367	—
8-16	—48.10348	—	—	—27277.75	—
9-16	267.0065	—	—	—40133.273	—
6-17	—33.7062	—	—	959.1721	—
7-17	285.0156	—	—	—	—8899.355
8-17	—34.9268	—	—	1216.5942	—
9-17	285.2434	—	—	—	—7688.215
6-18	—29.8447	—	—	—	—2100.906
7-18	296.5337	—	—	—	—5136.988
8-18	—30.7741	—	—	—	—2507.963
9-18	296.417	—	—	—	—4513.433
6-28	—41.3221	—	—	—	14656.716
7-28	267.4776	—	—	—5083.813	—
8-28	—44.203	—	—	—	14821.469
9-28	271.1931	—	—	—	37053.063
6-29	—48.7036	—191.4451	4785.293	—	—
7-29	253.5461	—404.1636	9922.5461	—	—
8-29	—54.1898	—244.3384	6297.5352	—	—
9-29	268.156	—284.437	—	—	—
6-30	—35.2721	—44.1034	—457.1682	—	12419.199
7-30	283.4253	—	—	—	—94.8064
8-30	—40.091	—57.8803	—	—	—
9-30	278.7434	—84.0031	—	—	—
6-31	—32.2859	—	—481.9697	—	—
7-31	228.4802	—	—1045.3175	—	—
8-31	—33.1792	—	—607.8804	—	—
9-31	289.3406	—	—918.3919	—	—
23-19	104.2394	—526.9827	—	—	—
23-20	—1.8724	—	22216.097	—	—3975742
23-21	2.75185	161.1247	—	—171341.81	—39591.88
23-22	28.0485	—	—	—	—4422.418
23-32	—7.5785	—390.6569	—	—	—
23-33	8.9018	—	30352.238	—	—18628128
23-34	18.43375	—447.606	—1955.16	34244.188	144292.13
23-35	18.6511	—582.01953	—	—	—119720.7

31

regression models obtained and shown in Table 1 should have a confidence level of $p < 0.01$. As it can be seen from this Table, almost all values of F are greater than the numbers corresponding to a confidence level of $p = 0.01$, but conclusions on the significance of the model can be valid only for $p = 0.05$ due to $n < 100$. This is not contradictory to the comparative model analysis, but we have to keep in mind that all models are at confidence level $p = 0.05$ (or 95 % reliability from a statistical point of view).

Under these conditions we can see that between all the 40 regression models there is a group of 15 models for which the F-value is significantly higher (about one or two orders more) than the value of the remaining ones.

Figures 1-4 show the type of some model regressive curves, describing the correspondent experimental data.

The study of the experimental data with the multiple regressive analysis applying a step regression from first to fourth power shows that between indices Nos 6, 17; 7, 17; 7, 18; 6, 30; 7, 30; 6, 31; 7, 31 there is a clearly expressed curvilinear dependence described by curves from first to fourth power. This is confirmed by the high values of the F-ratio (Table 1). But in some cases the general grouping of experimental data considerably differs from the model curve obtained with step regression. This is due to the fact that the program used for the polynomial step regression provides for the examination of dependences only by polynomials from first to fourth power. As a regular sequence the models defined by the program as best cannot be considered best in general. There are cases when although the program has shown a given curve of the same power as the best regression model for two different dependences, this curve does not describe the scatter of experimental data in a unified manner, for example for dependences Nos 23, 19 and 23, 32. The comparison between the F-ratio values for them shows that although the model curve for both models to be of first power, the model selected for the first is formally better, due to the twice greater value of F for 23, 19 compared to the one for 23, 32.

Table 3

Dependence between parameters Nos.	Correlative coefficients r	Confidence intervals	
		r_d	r_u
5-32	—0.9013	—0.909	—0.8957
6-27	0.9411	0.9366	0.9447
6-30	—0.9231	—0.9275	—0.9186
6-35	0.9503	0.9478	0.9536
7-35	0.9127	0.909	0.9154
8-27	0.9536	0.9508	0.9562
8-30	—0.9386	—0.9425	—0.9354
8-35	0.963	0.9611	0.9661

Table 4

Dependence between parameters Nos	Correlative ratio	Fischer's criterion F
8-17	0.8182	182.982
8-30	0.9797	503.402
8-31	0.9672	813.287
9-17	0.7962	158.002
9-30	0.9386	204.853
9-31	0.8712	392.186

32

The presence in experimental data of one or two values much larger than the other ones or different in sign results in significant change of the model curve type. In consequence, the regression model becomes worse. This can be
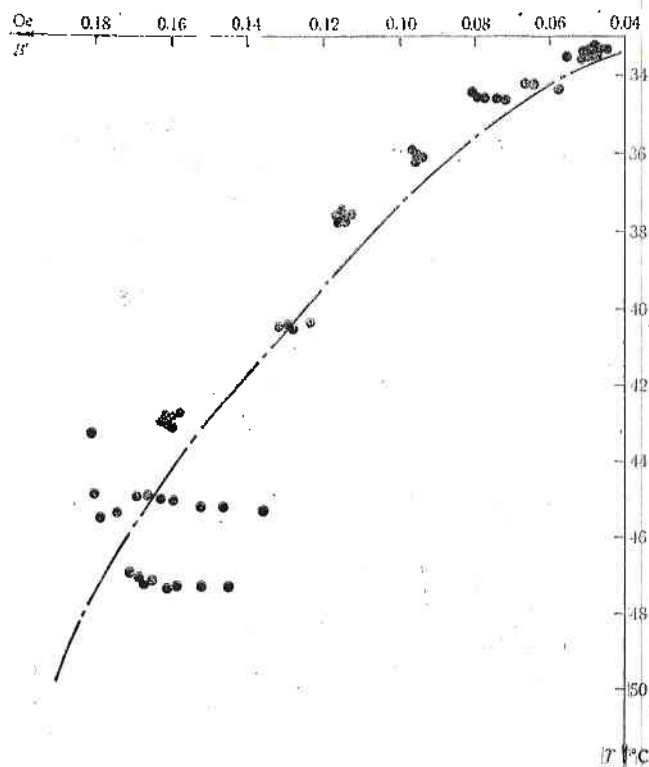

Fig. 1. Regression dependence between the intensity of the nondipole geomagnetic field ($h=10$ km) and the average atmospheric temperature ($h=10$ km)

elliminated by rejection of the single vaules because their presence may be of incidental nature with respect to the examined problem.

As already mentioned, both the data for observed and nondipole geomagnetic field obtained by the exclusion of the dipole field effects are subject to statistical processing. The comparison of results obtained shows that when the nondipole field is processed, the relationships determined between the indices of various groups (different nature) are more strongly expressed and clear nonlinearity of the dependences is observed. This is confirmed by the significantly greater values of the F-ratio (estimating the model accuracy).

Resulting from the application of the correlative analysis between the examined 35 parameters, the dependences (165 in number) characterized by the high coefficient of the common correlation are defined within the boundaries $\pm 0.7 \leq r \leq \pm 1$. The correlative coefficients related with dependences between indices of various nature (Table 3) are of particular interest. Part of these coefficients refer to relationships between meteorological parameters and components of the nondipole geomagnetic field and the rest — between these para meters and the components of the observed geomagnetic field. It is seen tha

for many nonlinear dependences having high values for the F-ratio the coeffi-
cient of the linear correlation is also high, as this is valid for all the linear
models from Table 1. The comparison performed confirms the expressed func-
tional dependence between variables observed (Table 3). The value of the cor-

Fig. 2. Regression dependence between the intensity of the nondipole
geomagnetic field ($h=10$ km) and the average atmospheric pressure
($h=10$ km)

relative ratios (Table 4) for some of the discussed relationships shows the
presence of strong functional dependence which confirms the reliability of the
relationship defined.

Results obtained permit to draw the following conclusions:

1. The application of data related with the nondipole part of the geomag-
netic field results in stronger manifestation of the relationships observed and
provides for relatively better interpretation from physical point of view.

2. Strongly expressed functional dependences are determined between the
intensity of the nondipole geomagnetic field H (level $h=10$ km) and the ave-
rage air pressure and temperature (for the same level) (Figs. 1 and 2), as well
as between the vertical component of the nondipole geomagnetic field and the
same parameters (for $h=10$ km, Figs. 3 and 4). The experimental data scatter
is described for these dependencies with model curves of second or fourth
power.

It can be seen form the comparison of the results from the statistical ana-
lysis that the functional dependences obtained, where components of the non-

34

Fig. 3. Regression dependence between the verical component of the nondipole geomagnetic field ($h=10$ km) and the average atmospheric temperature ($h=10$ km)
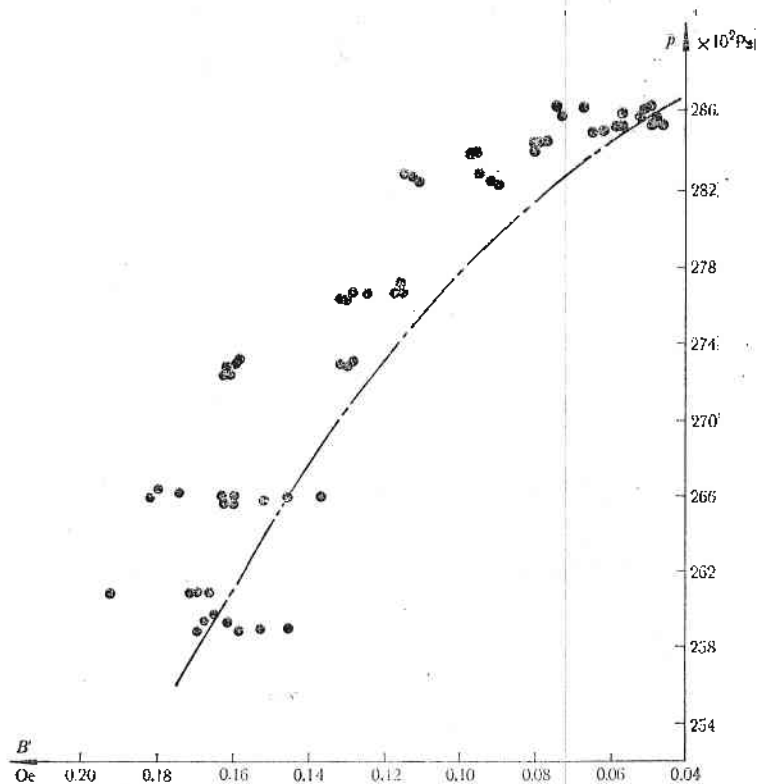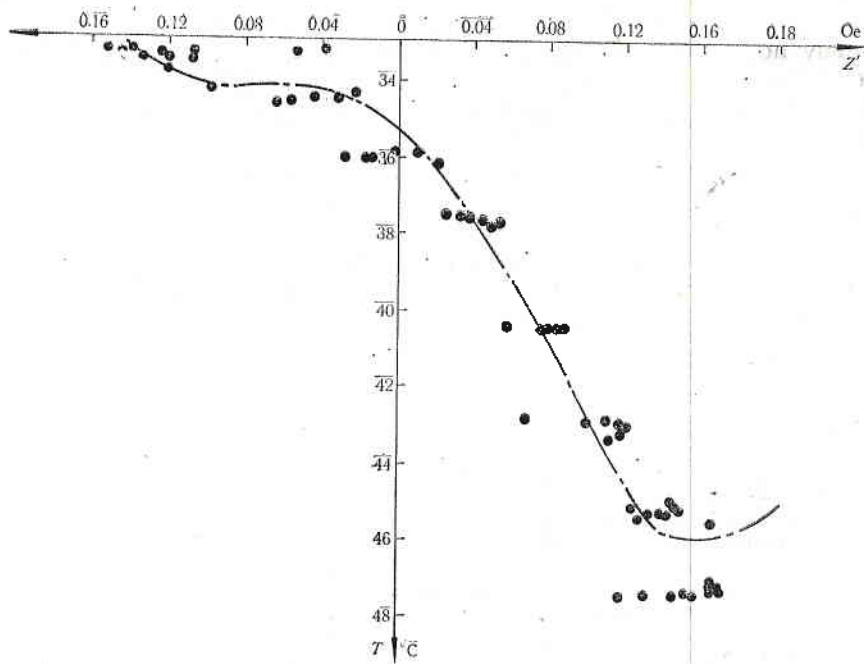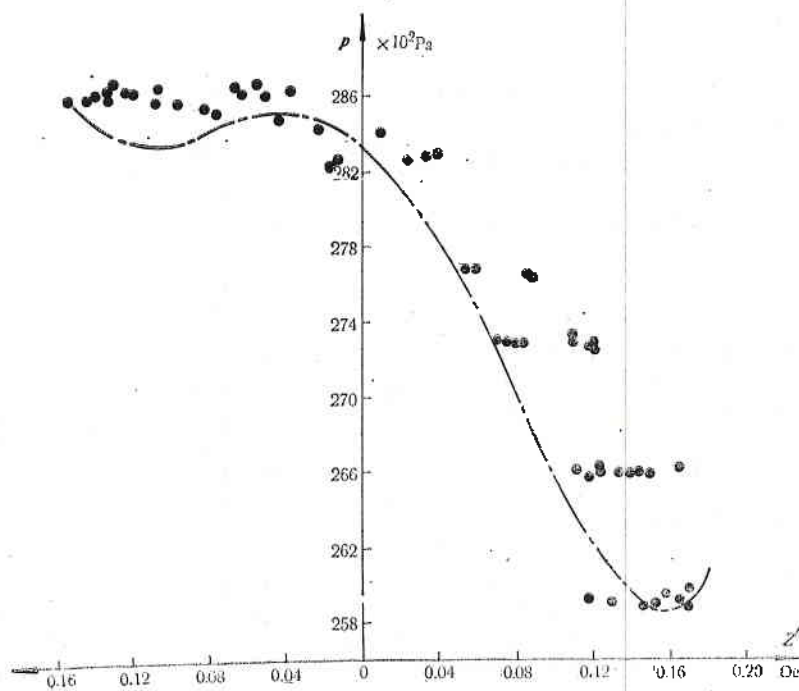

Fig. 4. Regression dependence between the vertical component of the nondipole geomagnetic field ($h=10$) and the average atmospheric pressure ($h=10$ km)

35

dipole geomagnetic field are incorporated, are more strongly expressed than the ones related with the components of the observed geomagnetic field. This can be interpreted in terms of the fact that the dipole field due to its smooth development of spatial variations results in "polishing" of the examined dependences and does not provide for the manifestation of peculiarities of the geomagnetic field that are directly affecting the temperature and the pressure at a given level. That is why the reduction of the dipole term provides for a possibility to study the relationship of the nondipole geomagnetic field with the mentioned meteo-fields. The field thus obtained contains all the specifics of the observed one and much more clearly represents its characteristic. The analysis performed confirms this fact as well.

References

1. Витинский, Ю. И., А. И. Оль, Б. И. Сазонов. Солнце и атмосфера Земли. Л., Гидрометеоиздат, 1976.
2. Митропольский, Н. К. Техника статистических вычислений. М., Наука, 1971.
3. Рао, Р. С. Линейные статистические методы и их применения. М., Наука, 1968.
4. Сазонов, Б. И. — В: Тр. ГГО, вып. 227. Л., Гидрометеоиздат, 1968.
5. Божанов, Е. С., И. Н. Вучков. Статистически методи за моделиране и оптимизиране на многофакторни обекти. С., Техника, 1973.
6. Герджикова, М. Г. Зависимости между аерономични и геофизични показатели в района на Южноатлантическата геомагнитна аномалия (unpublished).
7. Mishev, D. N., T. K. Janev, M. G. Gerdjikova, N. D. Pelova. — Comtes rend. Acad. Bulg. Sci., 31, 1978, No 9.
. Janev, T. K., M. G. Gerdjikova. — Comtes rend. Acad. Bulg. Sci., 33, 1980, No 10.

Зависимости между аэродинамическими и геофизическими параметрами для района Южноатлантической геомагнитной аномалии

Т. К. Янев, Д. Н. Мишев, М. Г. Герджикова, Н. Д. Пелова

(Резюме)

В настоящей работе рассматриваются статистические зависимости между аэродинамическими и геофизическими параметрами для района Южноатлантической геомагнитной аномалии. Исследуются 35 параметров, характеризирующих поведение некоторых метеополей, поведение геомагнитных полей — наблюдаемого и недипольного, а также проявления солнечной активности. Применяется корреляционный и регрессионный анализ для обработки данных. Как следствие этого получены наилучшие регрессионные модели, описывающие существующие экспериментальные данные при помощи полиномов с второй до четвертой степени.

Установлены очень четко выраженные криволинейные зависимости между полной интенсивностью недипольного геомагнитного поля для $h = 10$ km, с одной стороны, и температурой и давлением для $h = 10$ km — с другой, а также между вертикальной составляющей недипольного геомагнитного поля и теми самыми параметрами, снова для $h = 10$ km. Все они описываются полиномами второй либо четвертой степени.

36

Multispectral Imagery
and Interference Filter Effects

D. N. Mishev, K. P. Bakalova

The multispectral photography of the earth surface provides for useful infor mation both to science and practice and is applied in remote aero- and space sensing. The multizonal camera MKF-6 was elaborated for this purpose. The separation of the spectral ranges in it is effected through specially designed interference filters (IF) combined with coloured glasses. They are of steep slopes and large luminous transmittance. Imagery of objects studied with the MKF-6 is rectangular. The long side of the frame corresponds to an angle of sight $2\sigma_e = 36°$ and the short side — to $2\sigma_s = 25°$ [2]. It is assumed that such an angle of taking the image does not affect significantly the spectral brightness, related to the increase of the angle θ between the vertical and the picture direction [1]. The changes resulting from the fact that IF operate with relatively large light beams are not yet evaluated. We assume that such an evaluation should be performed. Therefore, we are looking for the IF effects on the frame image in a given spectral range using data from previous studies of other IF. This is based on the similarity between the angle characteristics of the IF of common principle of operation. The spectral coefficient of IF transmission is described by the function [3]

$$(1) \qquad \tau(\lambda, \theta) = \frac{J^{(l)}}{J^{(l)}} = \left(1 - \frac{A}{1-R}\right) \frac{1}{1 + F \sin^2 \frac{\delta(\lambda, \theta)}{2}},$$

where

$$(2) \qquad \delta(\lambda, \theta) = \frac{4\pi}{\lambda} nh \sqrt{1 - \frac{\sin^2 \theta}{n^2}} + 2\varphi,$$

$$(3) \qquad \lambda_m(\theta) = \frac{2nh}{m - \varphi/\pi} \sqrt{1 - \frac{\sin^2 \theta}{n^2}}, \quad m = 1, 2, \ldots,$$

with the following denominations: λ -- wavelength in vacuum; θ — slope of falling light; n — refraction index of the filter intermediate layer; h — thickness of the same layer; φ — phase shift; A — light losses from the filter reflective cover; R — cover reflective capacity and $F = \frac{4R}{(1-R)^2}$.

Both the wave length λ_m for which $\tau = $ max and the semiwidth $\Delta\lambda$ of the transmission band and the value of maximal transmission, are functions of the beam slope θ. Therefore, the IF effects on imagery would be revealed in two directions:

a) redistribution of illumination $E(\theta)$ on the frame;

b) spectral range shift in which the object brightness is studied.

The illumination at one frame point at a distance r from its centre ($r = f \operatorname{tg} \theta$, where f is the objective focal distance) may be represented as

$$(4) \qquad E(\theta) = \varphi(\theta) \int\limits_0^\infty B(\lambda)\tau_\theta(\lambda)d\lambda,$$

where $\varphi(\theta)$ is the specific function of a given optical instrument showing the light distribution along the field of sight; $B(\lambda)$ is the spectral brightness of the studied object; $\tau_\theta(\lambda)$ — spectral coefficient of IF transmission in the case of parallel light beam at angle θ. At equal exposure time, the negative density is defined from $E(\theta)$ at a given point. Therefore, the IF effect is expressed through the function $\theta_\theta(\lambda)$. We have examined the experimental data for $\tau_\theta(\lambda)$ of several IF [4]. It was defined there that the dependence $\tau_m(\theta)$ for $\theta \leq 20°$ is well approximated with the function $\cos(k\theta)$, where k is a constant typical for a particular filter. For the samples studied $k \sim 1.15—2.65$. The semiwidth $\Delta\lambda$ of the curves $\tau_\theta(\lambda)$ slightly increases with the θ slope increase differently from τ_m.

Let us examine two boundary cases determined by the function $B(\lambda)$ type:

1) the brightness of the object $B(\lambda)$ slightly changes within the resolution range of a given IF. $\lambda_1(\theta)$ and $\lambda_2(\theta)$ limit this range for a given θ. According to the theorem for the average values, from (4) we have

$$(5) \qquad E(\theta) = \varphi(\theta)B_\theta(\bar\lambda) \int\limits_{\lambda_1(\theta)}^{\lambda_2(\theta)} \tau_\theta(\lambda)d\lambda = \varphi(\theta)B_\theta(\bar\lambda)I_1(\theta).$$

From the function $I_1(\theta)$ with which we have denominated

$$(6) \qquad I_1(\theta) = \int\limits_{\lambda_1(\theta)}^{\lambda_2(\theta)} \tau_\theta(\lambda)d\lambda$$

and which may be considered as integral IF transmission for slope θ, the redistribution of energy over the frame is determined. The determination of the dependence of the integral IF transmission on the incident light angle is a very interesting fact in itself. It can be performed in different ways, for example through measurement of the light energy transmitted by the IF for various θ with nonselective receiver of given sensitivity or by calculating the integral $I_1(\theta)$. We shall examine the second case, as the calculation of $I_1(\theta)$ is performed through geometric calculation of areas surrounded by the experimental curves $\tau_\theta(\lambda)$ available. For the areas $S(\theta)$ under the curves $\tau_\theta(\lambda)$ the results presented in Table 1 were obtained. The maximum relative area variation under the curves $\tau_\theta(\lambda)$ for the two IF (i. e. of $I_1(\theta)$) is 3.3 and 1.5%, respectively. Therefore, we may consider with sufficiently good approximation that the integral transmittance of IF is constant by θ.

$$(7) \qquad I_1(\theta) = \mathrm{const} = I.$$

Table 1

Filter	$S(\theta)$	θ^0				$\left(\dfrac{\Delta S}{S}\right)_{max}$, %
		0	10	15	20	
1	$S_1(\theta)$	425	425	411	412	3.3
2	$S_2(\theta)$	471	475	478	472	1.5

Table 2

θ^0	r, mm	λ_m, nm						$\Delta\lambda$, nm	
0	0	480	540	600	660	720	840	40	100
5	11.5	479	539	599	659	719	839	40.6	101.5
10	20.0	477	536	596	656	715	834	42.6	106.5
15	33.5	473	532	591	650	709	827	46.2	115.5
18	40.5	470	528	587	646	705	822	49.5	123.6

This means that IF would not introduce additional redistribution of energy on the frame. In the case where the spectral characteristic of the object slightly changes within the operation range of IF, its effect is experssed by the constant I, i. e. quantitatively the filter weakens the light energy passed through it equally for all waves regardless of the angle of their propagation. In addition, the IF changes the spectral range in which the averaging of the measured brightness $\overline{B_\theta(\lambda)}$ is performed in dependence on the slope θ. Let us assume that the IF of the MKF-6 camera have $k=2$ and accept the following appproximation (which often happens in practice) — that the $\tau_\theta(\lambda)$ are Π-shaped curves whose width equals the semiwidth $\Delta\lambda$ for the slope 0, and the height is equal to the maximal transmittance for the same slope. Then, it follows from (6) and (7)

$$(8) \qquad \int_{\lambda_1(\theta)}^{\lambda_2(\theta)} \tau_\theta(\lambda)d\lambda = \tau_m(\theta)\Delta\lambda(\theta) = \tau_m(0)\Delta\lambda(0)$$

as $\tau_m(0)$ and $\Delta\lambda(0)$ are data from the filter passport. In addition, if we consider (3), we shall have an approximate picture of the variation in the spectral ranges introduced by the IF at different points of the MKF-6 frame. The results from these approximate calculations are given in Table 2 and plotted in Fig. 1, where the operation ranges of the MKF-6 camera are presented together with their shift in dependence of the distance r.

2) The brightness largely varies within the range of $\lambda_1(\theta)-\lambda_2(\theta)$. We shall consider the boundary case for such large variation, where $B(\lambda)$ changes in steps

$$B(\lambda) = \begin{cases} B, & \lambda \le \lambda_c \\ 0, & \lambda > \lambda_c \end{cases}.$$

Let $\lambda_c \in [\lambda_1(\theta), \lambda_2(\theta)]$ for some of the filters. The illumination distribution over the frame from (4) is

$$(9) \qquad E(\theta) = \varphi(\theta)B \int_{\lambda_1(\theta)}^{\lambda_c} \tau_\theta(\lambda)d\lambda.$$

The IF effect on the illumination distributions in this case is defined by the term

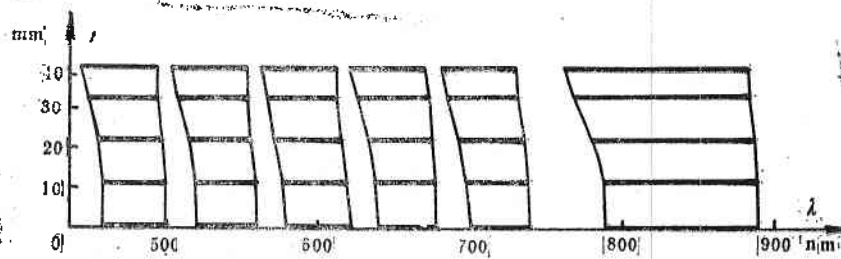$$I_2(\theta) = \int\limits_{\lambda_1(\theta)}^{\lambda_c} \tau_\theta(\lambda)d\lambda$$

Fig. 1

and can easily be calculated if we consider again the IF characteristics as Π-shaped, with reference to (7) then we have

$$I_2(\theta) = \tau_m(\theta)\,[\lambda_c - \lambda_g(\theta)],$$

λ_g is the left end of the Π-shaped characteristic.

$$\lambda_g = \lambda_m(\theta) - \frac{1}{2}\,\Delta\lambda(\theta)$$

$$I_2(\theta) = \tau_m(0)\lambda_c \cos(k\theta) - \tau_m(0)\lambda_m(0)\cos(k\theta)\sqrt{1 - \frac{\sin^2\theta}{n^2}} + \frac{1}{2}\,\tau_m(0)\Delta\lambda(0) =$$

$$= a\cos(k\theta) - b\cos(k\theta)\sqrt{1 - \frac{\sin^2\theta}{n^2}} + c,$$

where

$$a = \lambda_c\tau_m(0),$$

$$b = \tau_m(0)\lambda_m(0),$$

$$c = \frac{1}{2}\,\tau_m(0)\Delta\lambda(0).$$

Similarly, if $B = \begin{cases} B, & \lambda \geq \lambda_c \\ 0, & \lambda < \lambda_c \end{cases}$ and $\lambda_c \in [\lambda_1(\theta),\ \lambda_2(\theta)]$,

$$I_2(\theta) = -a\cos(k\theta) + b\cos(k\theta)\sqrt{1 - \frac{\sin^2\theta}{n^2}} + c.$$

Let a diffusively reflecting object (which often occurs in nature) with a step-like spectral characteristic fill up the entire field of sight of the MKF-6 objective. Then, in dependence on the values of λ_c, we shall obtain different pictures.

a) $\lambda_c < \lambda_g(0)$. Such an object would not be centered in the frame. It could be seen for distances greater than r for which $\lambda_c = \lambda_g(\theta)$, $r = f\,\mathrm{tg}\,\theta$, and with the increase of r the negative density will augment gradually. The frame would

40

Table 3

Parameters	Channel 2					Channel 5				
r, mm	4.3	12.6	18.2	21.1	27	4.3	9.4	12.0	21.1	27
$d(r)$	1.00	0.96	0.92	0.83	0.86	1.00	0.97	0.95	0.93	0.96

look as if two objects were photographed: one round shape, which does not emit within the filter range, and the second surrounding the first one with brightness gradually increasing in radial direction.

b) let λ_c be close to $\lambda_2(0)$ and the spectral brightness of the object filling up the objective field of sight be of the second type, i. e, limited from below. Such an object would appear on the frame as two objects: one in the centre with decreasing brightness and around it another one with zero spectral brightness in this range.

Thus the effect of IF over the frame image is the stronger the less smooth the spectral characteristic of the studied object is. For example, the spectral characteristic of grass permits to follow the decrease of its spectral brightness with the increase of the distance r from the frame centre for the 2nd and 5th channel of the MKF-6 camera for $\lambda = 540$ and $\lambda = 720$ nm, respectively. For the purpose, the densities of negatives representing grass (D_T) and white tissue (D_M) are measured with microdensity meter at different places of the frame. Pictures are taken with the MKF-6 camera on board the airplane laboratory AN-30 over a research field in Bulgaria. For the white tissue we obtain from (5) and (7)

(10) $$D_M(\theta) \sim E_M(\theta) = \varphi(\theta)B_M I, \quad B_M I = \text{const}$$

and for the grass we obtain from (5) and (10)

(11) $$D_T(\theta) \sim E_T(\theta) = \varphi(\theta)d(\theta) \sim D_M d(\theta)$$

or as

$$\theta = \operatorname{arctg}(r/f),$$

$$D(r) \sim D_M(r)d(r),$$

from where we obtain the function $d(r)$ normalized by its maximum value (Table 3). With the increase of r the value of $d(r)$ decreases due to spectral range shift, where the measured spectral brightness is averaged. This illustrates the effect of IF.

What type of practical conclusions may be drawn from this study. Certainly to the end of the frame the spectral range shifts to shorter wavelengths and expands. This effect is larger for the long-wave channels. The graphical presentation of this shift is sufficiently clear. It is seen that changes introduced by IF can be entirely neglected in the frame centre. The size of their area is specific for the instrument applying the IF and depend on the characteristics of the filters themselves. For the examined case, the IF do not change the picture in a circle with radius of about 22 mm centrally located ($\theta = 10°$). The approximate calculations performed may be considered as a pattern of evaluating the effect of IF used in the multispectral photographic images obtained and also in designing instruments similar to the MKF-6 camera.

References

1. Эксперимент „Радуга" — многозональное фотографирование Земли с космического корабля „Союз—22", ИКИ—АН СССР, Д-254, 1977.
2. Design and technical partmeters of the MKF-6 Multispectral Camera and the MSP-4 Multispectral Projector' Dr. A. Zickler, FEB Carl Zeiss Jena — GDR, International Symposium on Remote Sensing of Environment, April 1978, Manila, Philippines.
3. Борн М., Э. Вольф. Основы оптики. М., 1973.
4. Bakalova, K. Interferential Filters in Spectral Instruments without Collimation Optics. — Space Res. in Bulgaria, 3, 1980, 47-52.

Влияние интерференционных фильтров на получаемые с их помощью многоспектральные изображения

Д. Н. Мишев, К. П. Бакалова

(Резюме)

В данной работе рассматривается влияние интерференционных фильтров на многоспектральные изображения, полученные камерой МКФ-6. Показано, что влияние проявляется в смещении спектральных диапазонов работы камеры с увеличением расстояния r от центра к краю поля изображения. В качестве примера рассмотрено уменьшение спектральной яркости определенного объекта (люцерина) к краю кадра для второго ($\lambda = 540$ nm) и пятого ($\lambda = 720$ nm) каналов многоспектральной фотокамеры МКФ-6.

Problems Related to the Body Potential of Large Satellites and Their Particular Resolution with the Bulgarian Probe Experiment with Intercosmos-19 Satellite

S. K. Chapkunov, T. N. Ivanova, G. L. Gdalevich

A certain period of time after the launching of the three satellites from the automatic unified orbital station (AUOS) series (Cosmos-900, Intercosmos-17 and Intercosmos-18) the body is charged with large negative potential with reference to the potential of the studied plasma (PP), when the solar batteries are operating (illuminated object). This is a serious defect, particularly for measurements of thermal and low-energy plasma (this does not refer to optical and high-energy experiments). The large potentials observed, exceeding $-15\,V$ on the Cosmos-900 and $-12\,V$ on the Intercosmos series appear 6-7-days after the launch of Intercosmos-17 and two month after the launch of Intercosmos-18. In certain cases this potential attains a value of $-25\,V$. It is assumed that this is related to an error of systematic or accidental origin.

A precise analysis of the commands transmitted to the spacecraft, of the operation of the complex scientific equipment (SE) and of the service-systems is required. Two major sources of large negative body potential generation are assumed at present for the AUOS series [1]:

1. One of the possible causes is the wrong coupling of the negative output terminal (of the board power supply) $-28\,V$ with the spacecraft body through a leakage resistance of the order of tens or hundreds of $k\Omega$. The panels of the illuminated batteries represent a system of voltage sources with surfaces under different potentials. In order to evaluate the phenomenon, we may consider this system as two electrodes with a voltage between them of the order of $30\,V$ (i. e. double probe immersed into the studied plasma). Due to the high electron mobility, from their thermal velocity v_{T_e} and the ion collection at the expense of electrode motion with the satellite velocity, only if $v_0 \gg v_{T_i}$, a nonlinear characteristic is obtained. The equalization of the electron and ion currents of the double probe is possible only when the positive electrode is of $2 \div 5\,V$ more positive than PP and the negative receives potential around $-25\,V$.

If the satellite is well insulated, from the feeding output terminal it receives a floating potential $(-4 \div +1)$ V with reference to the PP from secondary effects (rectified HF antenna voltage, photoemissions, charged particle fluxes, etc.) regardless of the solar batteries. But at reduced insulation resistance (R_{ins}) with respect to -28 V in a supply output terminal, the magnitude of the ion currents is limited and the satellite conductive surface is charged with negative potential $U_s = U_- + R_{ins} \cdot I_i$ which at low values of R_{out} and reduced N_i may attain -25 V with respect to the PP.

2. The possibility of leakage for the negative output terminal of the supply is larger than for the positive, as far as the output terminal -28 V is used as common and is permanently passed to all the instruments. The commands are transmitted to the positive output terminal $+28$ V from where the nonfunctioning instruments are switched off as well.

Series of conclusions may be drawn from the above-mentioned possible sources as to the further design of large satellites both for the constructors of the spacecraft and for the design of the different scientific experiments.

A. Recommendations to spacecraft constructors in order to avoid the effect of body charge:

a) To increase the effective spacecraft surface (2.5 m² only for AUOS); conductor and solar battery panel shielding; coating of nonconductive surface (thermal protective coat) with metal set of 5 mm step;

b) Not to switch on all the instruments to the negative output terminal -28 V and to use it for all switchings and commands. To utilize as common the positive output terminal $+28$ V;

c) At all test stages for the spacecraft (including complex ones with self-acting feeding by illuminated batteries) to control the insulation resistance of the chemical and solar batteries circuits with reference to the satellite body with additional instrument at voltage of 100 V.

B. As the Intercosmos-19 was ready for launching, the constructors of the instruments from the complex scientific equipment had to introduce some changes in the electric circuits:

a) A single command of switching on and off of a resistance 1 was introduced in the satellite-controlling block (SCB-4). Under such coupling of the spacecraft body and the supply output terminal $+28$ V, regardless of leakage from the negative output terminal -28 V, the body potential cannot exceed $--12$ V (excluding the case of short circuit at -28 V at the satellite body). Under resistance $R = 1$ kΩ and short circuit of $--28$ V, an additional consumption of 0.9 W appears. Besides, the possible error at the telemetry input is 0.05 %, which is probably much less than the error generated by the satellite variations;

b) To execute thorough control over the insulation resistance at the input of the secondary sources of feeding for each instrument from the complex SE. At a voltage of 100 V the resistance of output terminals $+28$ V and -28 V to the spacecraft body should be larger than 20 MΩ at normal humidity situation;

c) This negative potential would result in significant losses of scientific information obtained by the probe experiments, therefore constructors of such instruments have to consider the possibility of expanding the operation range of the input voltages and the sweep size to the sensors (expansion of the functional capacity).

C. To resolve the problem on the body potential for Intercosmos-19 (AUOS type) in the particular case of combined probe instrument experiment.

44

The Intercosmos-19 satellite was launched on February 27, 1979 with the following orbital parameters: apogee — 996 km, perigee — 502 km, rotation period — 99.8 min, orbital inclination — 74°. For the first time two Bulgarian space instruments (EMO-1 and P-4) were flown and operated on board such a large spacecraft. But while the body potential did not affect the optic electrophotometer EMO-1, the combined probe instrument P-4 (designed to measure the parameters of the ion and electron plasma components) had to be largely modified in comparison to the other P-series instruments flown on small satellites (Intercosmos-8, 12 and 14) [2, 3].

a) Modification of the cyclogram of the spheric ion traps function PL-39/1 and PL-39/2 (sensors of the P-4 instrument) designed to measure the ion plasma component (M_i, T_i, N_i) in order to reduce disturbances generated by the body potential variations due to the sawtooth voltages with large amplitude at their outer grids. This affects the precision of measurement of many instruments from the ionospheric complex SE on board the spacecraft: the experiment with the high-frequency probe KM3 (Czechoslovakia); the low-frequency analyser ANCH-2ME (USSR) for measurements of the electric component; the experiment with the Langmuir cylindric probe P-4 (Bulgaria) and to a certain extent — the functioning of all antenna instruments (the thickness of the bulk charge layer varies).
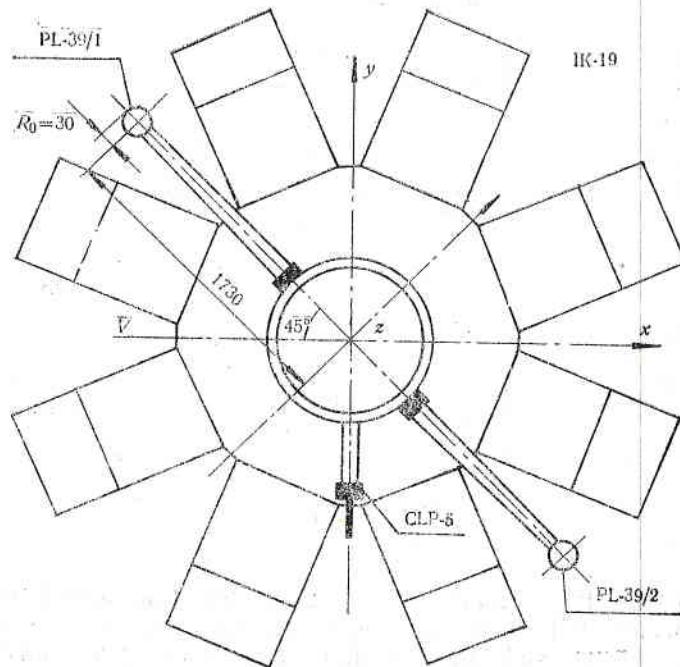

Fig. 1

The situation of the sensors to the P-4 instrument — ion traps PL-39/1,2 and the cylindric Langmuir probe CLP-5 on the body of the oriented satellite Intercosmos-19 is given in Fig. 1. The initial version of the P-4 instrument was designed for successive feeding of sawtooth voltages (points 2 and 3

of the time diagrams in Fig. 2) from the sweep generator, synchronized with the board pulses with quartz stabilized frequency board-time 1 (point *1* from Fig. 2).

Regardless of the relatively large AUOS satellite size, the net conductive surface is small (2.5 m²) and slightly differs from the surface of the small
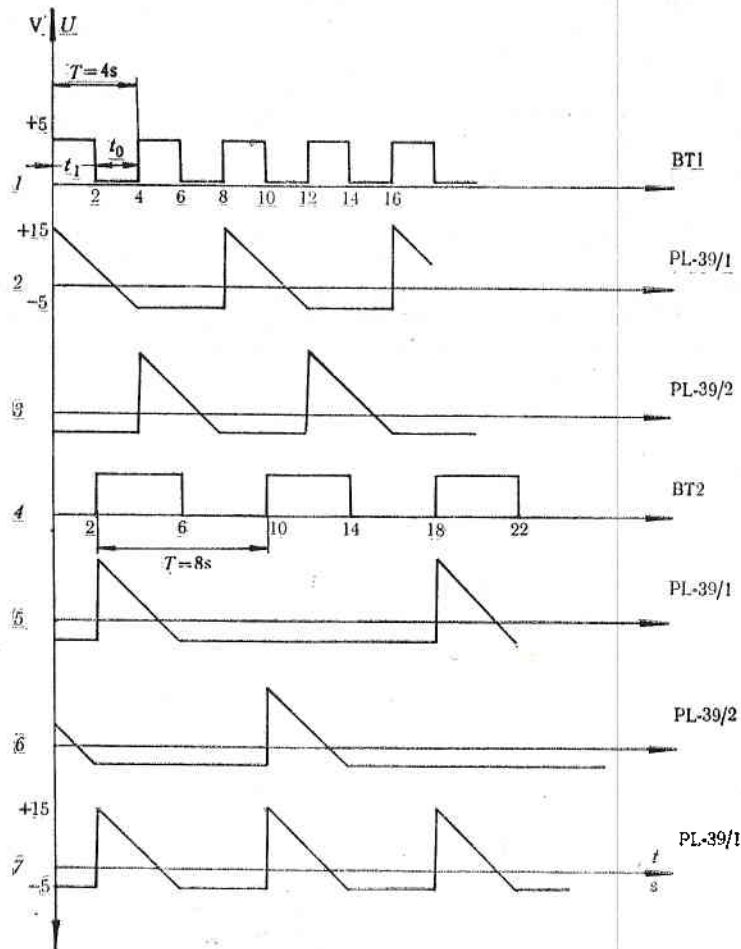
Fig. 2

satellites from the Intercosmos series. The system trap-satellite represents a double probe which collects electrons from all directions when a positive potential is fed to the IT while the satellite collects electrons only from the contrary flux. For slight potential variations of the satellite it is necessary [4]

$$\frac{S_s}{S_{IT}} > \alpha \sqrt{M_i \frac{m_i}{m_e}}, \quad \text{where} \quad \alpha = f\left[\frac{eU_0}{kT}\left(\frac{D}{R}\right)^{4/3}\right].$$

The minimum IT surface (without considering the bulk charge layer) $S_{IT} \geqslant 113$ cm² at $R_0 = 3$ cm (Fig. 1).

The projection of the satellite conductive surface over a plane perpendicular to the velocity vector is $S_s = 2.5 \times 104/4 = 6250$ cm² (under assumption

46

Table 1

Potential of I T, V	0	+5	+15
Coeffcient α	1.47	7.0	19.0
Required surface ratio	236	1122	3045

that the conductive surface is equally distributed). Hence the ratio between surfaces $S_s/S_{IT} = 56$. But most simple calculations with the given formulas for field height $H = 500$ km (perigee) at $M_i = 14$, $T_e = 2500$ K and $D = 0.6$ cm show that this ratio is much smaller than the required even at zero potential of IT (Table 1).

Therefore, for $H = 500$ km we may neglect the applied to the IT voltage effect over the satellite potential at ratio of the active surfaces more than 3,000. As far as this requirement was hardly satisfied, two modes of reducing this effect were suggested.

1. To use the Bulgarian traps supplied with a fourth outer shielding grid (flown on two rocket experiments already — Vertical — 7 and Centaur-II). But constructors did not permit a change of sensor with larger size ($R_0 = 3.5$ cm) and weight (85 g) due to the fact that the satellite had passed all test stages and was prepared for launching.

2. New cyclogram of the sensors IT operation (points 5 and 6 from Fig. 2) in argeement with the board-time 2 (point 4). But the cyclogram thus suggested reduced two times the instrument resolution (measurements by 16 s). Besides, one of the IT would be in shadow and it will be difficult to determine which information has to be processed. In addition, this satellite was not provided with mass-spectrometer, thus the determination of the ion composition has to be performed with the IT measurements and this required greater frequency.

In the final version of the cyclogram for the P-4 instrument operation, a sweep voltage is supplied to the PL-39/1 sensor only at an angle of 45° of $\bar{V}$ (Fig. 1). This results from the fact that the instrument is located on the front plane of the spacecraft and the possibility to flow in an undisturbed plasma is greater, referring to disturbances provided by the solar batteries, antennas, sensor booms for the other experiments, etc. The sensor PL-39/2 is under floating potential in order to define the time interval for which a sawtooth voltage is not fed to the PL-39/1 (this is replaced by a direct voltage of —5 V). This has to overlap with the bottom level of the meander board-time 2 (point 7 from Fig. 2).

As the board meander board-time 1 is relatively accurate (t_1) = 2.002 s, $t_0 = 1.998$ s) no problems occurred from the back front of board-time 1 in the synchronization of the sweep generator to IT.

b) Introduction of additional block for the measurement of the floating potential U_{FP} on the insulated outer grid of IT. This is permanently controlled on PL-39/2 and on PL-39/1 only in M-4 mode, when a sweep voltage is fed there too. Then the U_{FP} is measured in sequence on the two IT with a period of 4 s with respect to the satellite body (and with reverse polarity on IT). It should be mentioned that we do not measure the potential plasma-spacecraft but sensor-spacecraft and the floating potential of an insulated sensor is by 0.7÷0.8 V more negative compared with the plasma.

The emitting repeaters with high input resistance (OA with FET input) measure the U_{FP} within a range of (+15÷—1) V and from the outputs the voltage is then translated to the telemetry scale range (0÷+6) V and is sup-

plied through a single channel (328-PP). The graph dependence and the formulaes for the U_{FP} determination are given in Fig. 3.

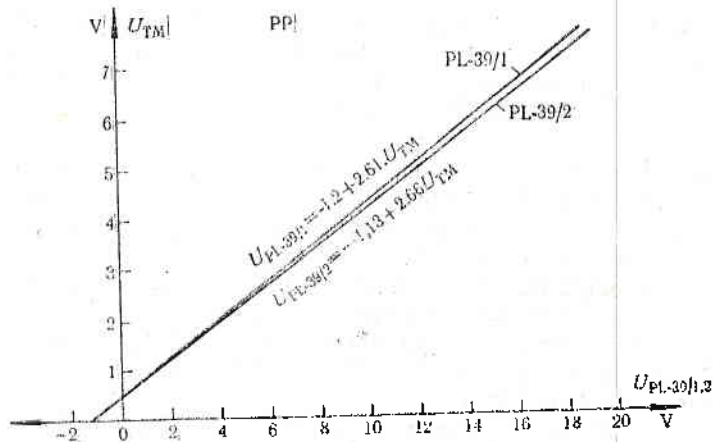c) Range variation of the sweep generator for CLP-5 in dependence on U_{FP}.

Fig. 3
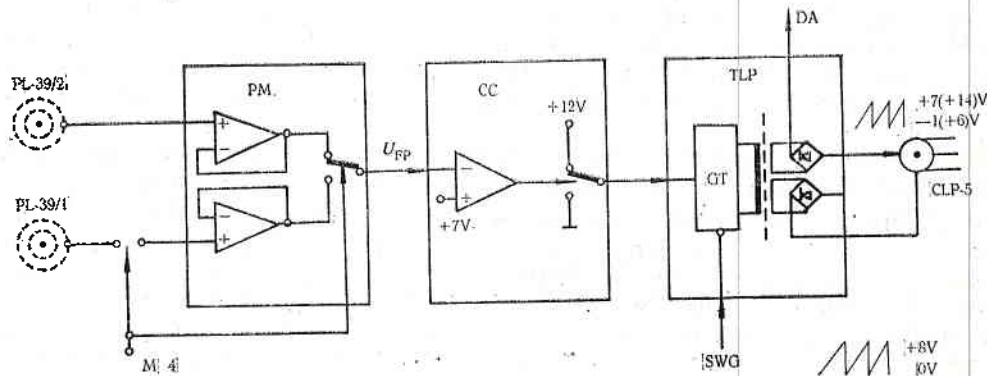
Fig. 4

The P-4 instrument measures the parameters of the electron plasma component (T_e, N_e) with the help of a cylindric Langmuir probe, mounted perpendicular to $\vec{V}$ (Fig. 1). The block diagram of the additionally designed system to this circuit is given in Fig. 4.

By the scheme of comparison which starts to operate at $U_{FP} = +7$ V (measured by the MP block) the range of sawtooth voltage variations is switched on CLP-5 from $(-1 \div +7)$ V to $(+6 \div +14)$ V. This is realized in the high-frequency generator of the transformer (GT) of the block TLP, which is controlled by the basic generator SWG to supply two equal linearly increasing voltages (the acceptable difference between them being 0.1 V) to the electrodes of CLP-5, as one of them is insulated from the spacecraft (between the collector of CLP-5 and the amplifier input DA).

48

In conclusion, we may say that problems related to large satellites are bigger than the problems attached to small spacecraft. The presence of insulated surfaces increases the possibility of variations in the spacecraft potential of the order of tens of volts (see e. g. [5]), which even under normal conditions (normal potential difference "plasma-satellite") makes difficult the operation of the probe instruments mainly and also of all low-energy measurers (electrostatic and electromagnetic scientific equipment).

The problem of the optimum potential for this type of measurements is much more complicated and this paper should be considered as a first attempt only to introduce recent Bulgarian contribution to this new and important scientific field.

References

1. Материали от съвещанието на Работната група по космическа физика към съвета „ИНТЕРКОСМОС". Прага, 1978.
2. Чапкынов, С. К., Т. Н. Иванова, М. Х. Петрунова. Прибор П1 для измерения параметров плазмы вблизи искусственного спутника Земли. — Научные приборы, 5, 1974, с. 39.
3. Чапкынов, С. К., М. Х. Петрунова, Т. Н. Иванова. Прибор П2 для измерения параметров плазмы вблизи искусственного спутника Земли. — Научные приборы, 11, 1976, с. 23.
4. Козлов, О. В. Электрический зонд в плазме. М., Атомиздат, 1969.
5. Parker, I. W. Differential charging and sheath assymetry of nonconducting spacecraft due to plasma flows. — J. Geophys. Res., 83, p. 10.

Проблемы, связанные с потенциалом корпуса спутников
больших размеров, и частичное их решение при проведении
болгарского зондового эксперимента на „ИК-19"

С. К. Чапкынов, Т. Н. Иванова, Г. Л. Гдалевич

(Резюме)

В данной работе обсуждается проблема появления относительно большого отрицательного потенциала на корпусе спутников серии „АУОС" во время их нахождения на освещенных частях орбиты. Проведено глубокое исследование возможных причин его возникновения и обсуждены методы уменьшения его влияния. Подробно рассмотрен случай „ИК-19" —(АУОС-3-Ионозонд), а также изменения, необходимые для предотвращения влияния потенциала корпуса спутника. Описываются особенности болгарского комбинированного зондового прибора „П4", выведенного на орбиту спутником „ИК-19", в двух аспектах: с одной стороны, уменьшение взаимного влияния экспериментов с точки зрения нарушения равновесного потенциала корпуса, а, с другой — увеличение его функциональных возможностей и обеспечение его работы при высоком потенциале корпуса.

Correlation of Wind and Electric Field in the Nocturnal *F*-Region

James C. G. Walker

National Astronomy and Ionosphere Center, Arecibo Observatory, Arecibo, Puerto Rico 00612, U.S.A.

Introduction

The incoherent scatter radar of the Arecibo Observatory operates at a frequency of 430 MHz and a peak transmitter power of 2 MW. Combined with an antenna that is 300 m in diameter, the radar is sufficiently sensitive to measure the drift velocity of *F*-region ions parallel to the radar beam to an accuracy of 2 m. s $^{-1}$ after an integration time of only 10 min. The radar beam can be pointed in any direction within 22° of the zenith. If it is assumed that ionospheric drift velocities do not vary with position over horizontal distances of about 200 km and vary with time in a linear fashion it is possible to combine line-of-sight velocity measurements made in various directions to derive three orthogonal components of the ion drift velocity vector (B e h n k e, H a r p e r, 1973). Figure 1 illustrates this procedure in two dimensions.

A particularly useful coordinate system to use for the drift velocity is one which specifies the components parallel to the geomagnetic field, perpendicular to the magnetic field and horizontal, and perpendicular to the field in the magnetic meridian plane. At *F*-region heights, where the ion-neutral collision frequency is much smaller than the cyclotron frequency, ion motion perpendicular to the magnetic field can be produced only by an electrostatic field. The parallel component of the motion is caused by the combined influence of the neutral wind (only the component parallel to the magnetic field is effective) and ambipolar diffusion.

This paper is concerned with the relationship between the parallel component, designated $v_{//}$, and the perpendicular component in the vertical plane containing the magnetic meridian, designated $v_\perp$. These two components to-

gether influence the continuity equation for *F*-region ionization and the height of the *F*-layer. The horizontal component of the ion drift velocity does not affect the electron density profile unless horizontal gradients in the ionosphere are large.
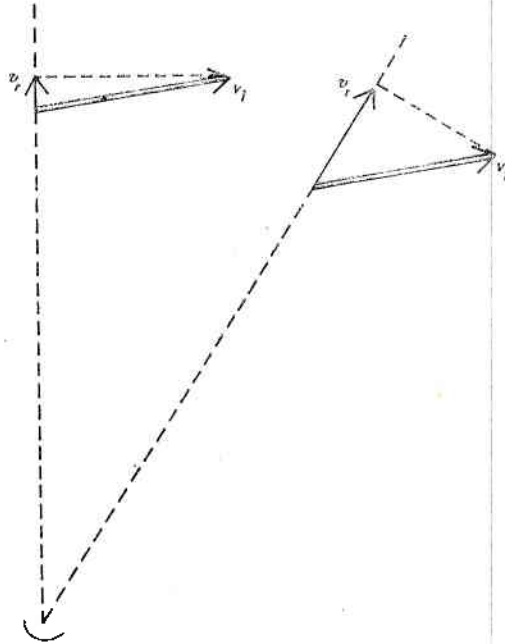

Fig. 1. Provided it does not vary horizontally, the ion velocity vector, v_i, can be derived from measurements of the line-of-sight velocity, v_r, made with the radar beam pointing first in one direction and then in another

The very surprising result revealed by Arecibo measurements in the nocturnal ionosphere is that there is a strong negative correlation between $v_{\parallel}$ and $v_{\perp}$ (B e h n k e, H a r p e r, 1973). A representative example of this negative correlation is shown in Fig. 2. The figure reveals marked fluctuations in both velocity components on a time scale of an hour or two, with the fluctuations of the two components being approximately equal in amplitude and opposite sign. Since both components are defined as being positive upward and since the magnetic dip angle at Arecibo is 50', it appears that the vertical component of $v_{\parallel}$ tends to cancel the vertical component of $v_{\perp}$, while the two horizontal components add. Evidently there is some feedback mechanism in the *F*-region that constrains ionization to move horizontally rather than vertically, even when the magnetic field is neither horizontal nor vertical.

The nature of this feedback mechanism has not yet been convincingly etablished. This paper reviews various mechanisms that have been suggested, reaches some tentative conclusions, and recommends directions for further research.

51

Theoretical considerations

Three mechanisms have been suggested to explain the negative correlation between $v_{\parallel}$ and $v_{\perp}$. They are ion drag (Dougherty, 1961; Rishbeth et al., 1965; Behnke, Harper, 1973; Thomas, Williams, 1975), F-re-
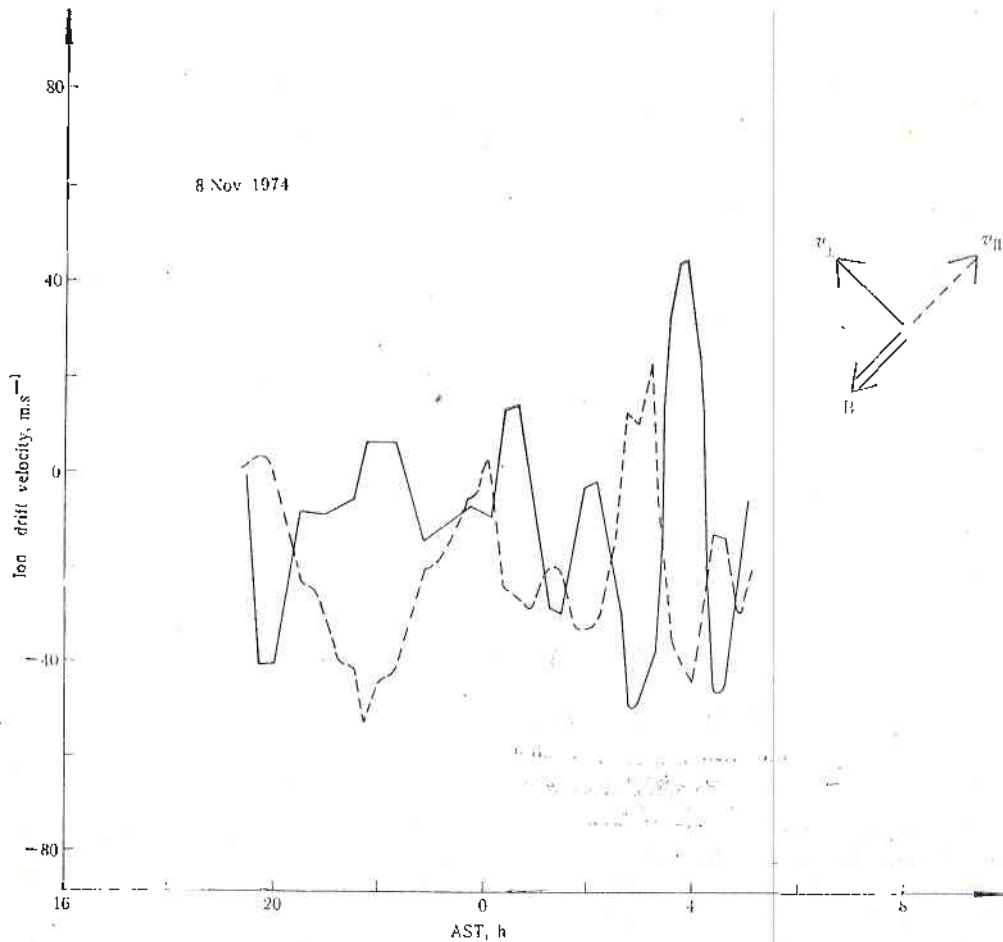
Fig. 2. Measurements of the ion drift velocity vector in the nocturnal F-region over Arecibo reveal a marked negative correlation between the components parallel and perpendicular to the geomagnetic field

gion polarization field (Rishbeth, 1971a, b; Behnke, Hagfors, 1974; Heelis et al., 1974), and diffusion (Rishbeth, 1967; Stubble, Chandra, 1970). This section describes these three mechanisms and compares, in qualitative fashion, their predictions concerning ionospheric behavior.

The ion drag mechanism is illustrated in Fig. 3. It is assumed here that the eastward electric field increases, causing an immediate increase in $v_{\perp}$. The friction of the ions drifting through the neutral gas affects the motion of the neutrals so that, after some time, the neutral wind U acquires an additional northward component. This northward component of the wind blows ionization down the magnetic field, causing a negative perturbation in $v_{\parallel}$. Equilibrium is

52

achieved when there is no relative motion of ions and neutrals, the situation illustrated in Fig. 3.

There is no doubt that the ion drag mechanism can, in principle, cause a negative correlation of v_{II} and $v_{\perp}$. The problem, at least for the nocturnal
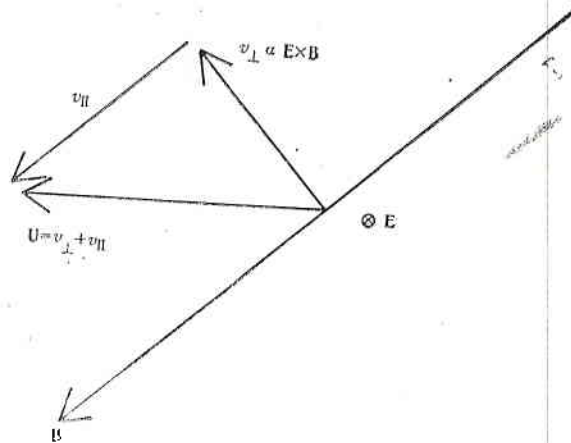
Fig. 3. The ion drag mechanism. See text for explanation
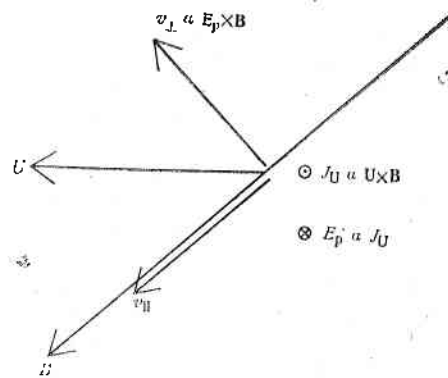
Fig. 4. The polarization field mechanism. See text for explanation

ionosphere, is associated with the time it takes for ion drag to modify the neutral wind. Roughly speaking, the neutral wind can change significantly only after all of the neutral atoms have collided at least once with an ion (Rishbeth, Garriott, 1969). The characteristic time for the ion drag mechanism is therefore the inverse of the neutral-ion collision frequency. For nocturnal ion densities less than 3×10^5 cm^{-3} this time exceeds 1.5 hours. Evidently the ion drag mechanism cannot explain the negative correlation of v_{II} and $v_{\perp}$ on a time scale of an hour or two that is shown in Fig. 2.

The polarization field mechanism is illustrated in Fig. 4. It is assumed here that the northward component of the neutral wind changes, causing a downward increase in v_{II} and, at the same time, an increase in the westward flow of Pedersen current in the F-region If the flow of this electric

53

current is inhibited by horizontal variations in the ionospheric conductivity or wind, charge will accumulate, and an eastward polarization electrostatic field will develop to restrict the flow of F-region Pedersen current. The polarization field, in turn, will cause an upward increase

Fig. 5. The diffusion mechanism. See text for explanation

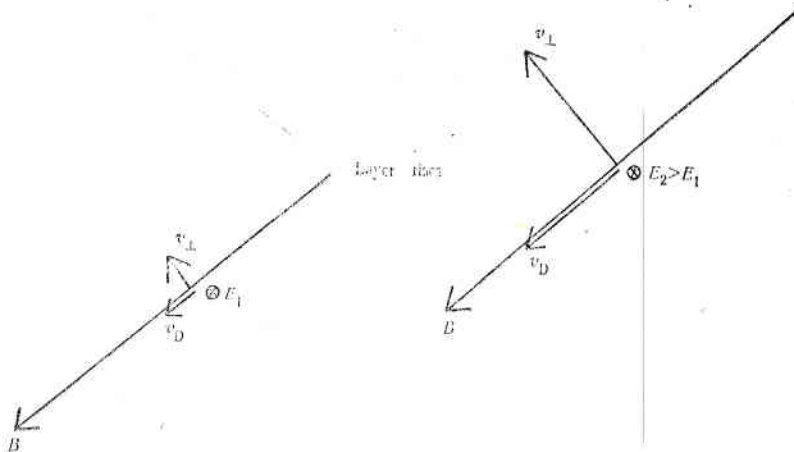in $v_\perp$, as shown in Fig. 4. In equilibrium there is no relative motion of ions and neutrals and no current flow. The response of the ion velocity components to a change in neutral wind is instantaneous, but the polarization field mechanism works only if the flow of F-region current is inhibited by horizontal variations.

The diffusion mechanism is illustrated in Fig. 5. Here it is supposed that an increase in the eastward electric field causes an upward increase in $v_\perp$. The vertical component of $v_\perp$ causes the F-layer to rise from the position shown on the left of the figure to that shown on the right. Because the diffusion coefficient increases exponentially with increasing altitude, the downward diffusion velocity, v_D, increases as the layer rises. The increasing diffusion velocity appears in the data as a downward increase of $v_\parallel$ which accompanies the upward increase of $v_\perp$. The characteristic time associated with this mechanism is the time for the height F-layer to respond to changes in externally imposed vertical drift velocity. Theoretical considerations indicate that this time is less than about 15 min.

Comparison of the Theories

The three mechanisms therefore differ in several respects. The ion drag and diffusion mechanisms both assert that the basic cause of fluctuations in $v_\parallel$ and $v_\perp$ is fluctuations in the externally imposed electric field. According to the ion drag mechanism, the neutral wind contribution to $v_\parallel$ changes in response to the field induced change in $v_\perp$; according to the diffusion mechanism it is the diffusion component of $v_\parallel$ that responds to the change in $v_\perp$. The polarization field mechanism differs from both ion drag and diffusion by attributing the fluctuations not to externally-imposed electric field change but to externally-imposed change in the neutral wind. We do not, at present, know

54

why either the wind or the field should fluctuate on a time scale of hours during the night, but identification of which of these mechanisms is responsible for the negative correlation of $v_{\parallel}$ and $v_{\perp}$ would tell us which fluctuation requires explanation.
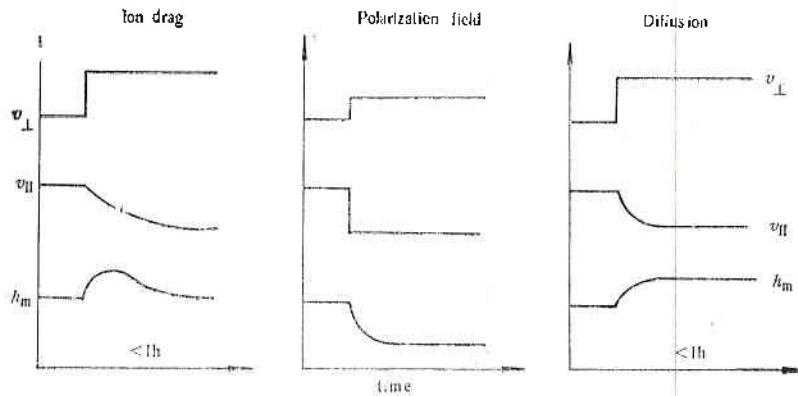

Fig. 6. Predictions of the three mechanisms concerning the correlation between change in F-layer height and change in the velocity components

The three mechanisms differ also in their predictions concerning the time lag between fluctuations in one velocity component and fluctuations in the other. The time resolution of the data is not good enough to permit a choice between the instantaneous response of the polarization field mechanism and the 15-min. response of the diffusion mechanism, but it is good enough to rule out the 1 to 2 hour response of the ion drag mechanism (see Fig. 2).

Finally, the three mechanisms differ in their predictions concerning the response of F-layer height to changes in ion drift velocities. These responses are compared in Fig. 6. According to the ion drag mechanism, a sudden increase in upward $v_{\perp}$ causes a rapid rise in F-layer height. Gradually ion drag increases the northward neutral wind and $v_{\parallel}$ increases downward. Increasing negative $v_{\parallel}$ drives the F-layer down again until, after several hours, the vertical components of $v_{\parallel}$ and $v_{\perp}$ are equal in magnitude but opposite in sign and the F-layer has returned to its original height.

According to the polarization field mechanism, a sudden downward increase in $v_{\parallel}$ is accompanied by a sudden upward increase in $v_{\perp}$. The mechanism is not perfect however; some current must flow, to return either through the E-region, the conjugate point ionosphere, or in a horizontal circuit through the F-region. Therefore the upward increase in $v_{\perp}$ is not as large as the downward increase in $v_{\parallel}$. As a result, the F-layer moves downward in response to a net downward component of the combination of $v_{\parallel}$ and $v_{\perp}$.

According to the diffusion mechanism, a sudden upward increase in $v_{\perp}$ causes the F-layer to rise. As it rises the downward diffusion velocity increases until a new balance is achieved, with $v_{\perp}$ upward, a smaller $v_{\parallel}$ downward, and the F-layer at a greater height than before. The important distinction between the polarization and diffusion mechanisms, therefore, is that the former predicts a positive correlation between F-layer height and $v_{\parallel}$ while the latter predicts a positive correlation between F-layer height and $v_{\perp}$.

We therefore compare, in Fig. 7, the measured F-layer height and the measured velocity components for the night illustrated in Fig. 2. The correlation between F-layer height and $v_\perp$ during the latter half of the night is striking. Unfortunately, there appears to be an equally strong correlation bet-
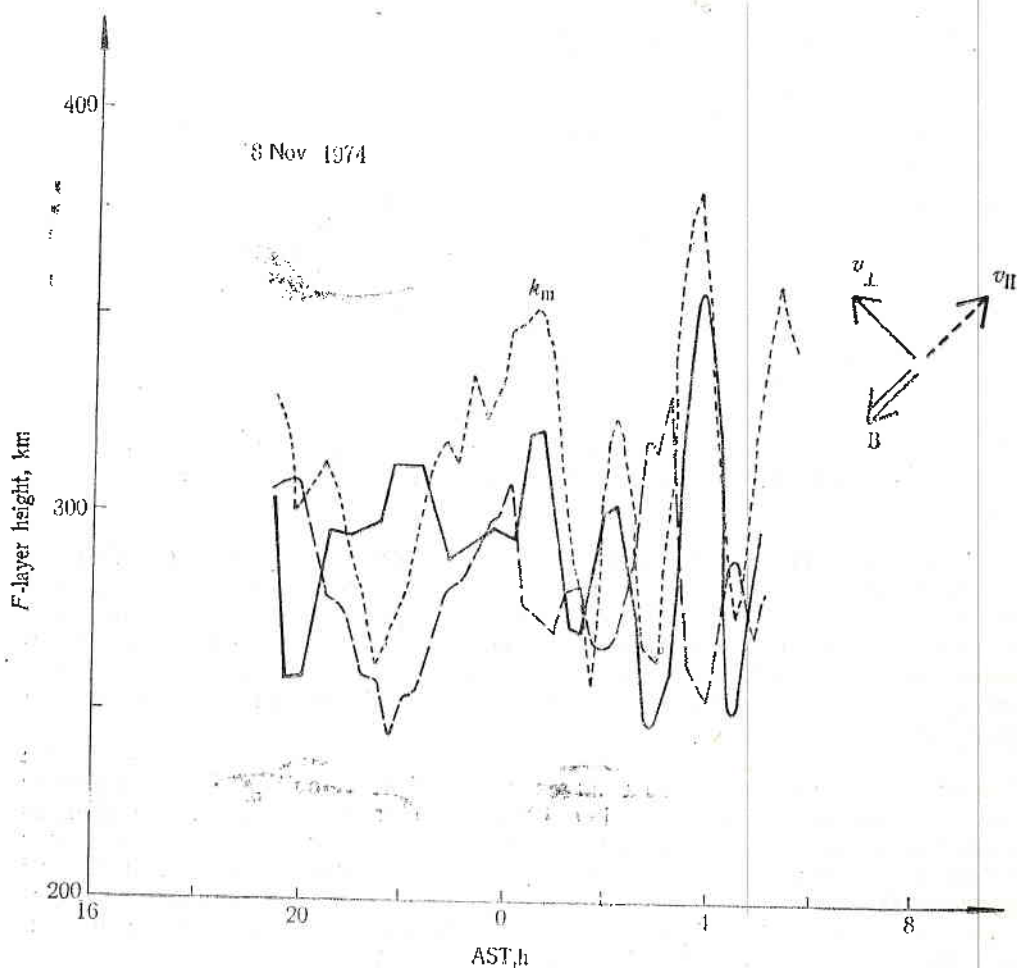
Fig. 7. Measured F-layer height (dotted line) compared with measured velocity components

ween height and $v_{\parallel}$ during the first half of the night. Examination of other nights of Arecibo data leads to the same result. The negative correlation of $v_{\parallel}$ and $v_\perp$ is nearly always well-developed, but the height of the F-layer correlates sometimes with one velocity component and sometimes with the other. Possibly both the polarization field and the diffusion mechanisms are contributing, with a relative importance that varies during the night for unkown reasons.

56

Suggestions for Further Research

It might be possible to distinguish between the polarization and diffusion mechanisms by comparing F-layer height changes at the two ends of a geomagnetic field line. Figure 8 indicates what the two mechanisms predict.
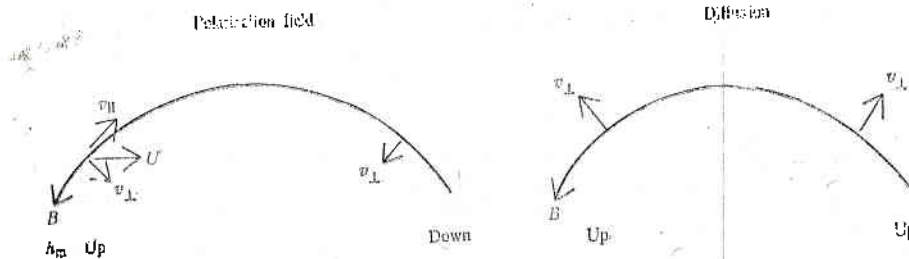
Fig. 8. Changes in F-layer height at the ends of a geomagnetic field line according to the polarization field and diffusion mechanisms

According to the polarization field mechanism, an equatorward wind at one end of the field line causes the F-layer to rise while developing a polarization field that causes a downward $v_\perp$. The polarization field, but not the wind perturbation, is transmitted to the conjugate point by the large field-aligned electrical conductivity of the topside ionosphere and protonosphere. Thus the F-layer rises in one hemisphere while falling in the other. The diffusion mechanism, on the other hand, predicts that the F-layer will rise at both ends of the field line under the action of the externally imposed electrostatic field. Changes in neutral wind are not involved in this mechanism. A study by P e t e l s k i (1972, 1973) indicates that F-layer height changes at conjugate points are generally correlated positively, but the correlation has not been investigated for stations at geomagnetic latitudes as low as that of Arecibo (30°N).

The considerations described in this paper have been entirely qualitative. Quantitative theoretical analysis of the various possible explanations for the negative correlation of $v_\parallel$ and $v_\perp$ combined with a careful comparison of theoretical predictions with data can be expected to clarify the situation. Scientists of any nation wishing to use the observing facilities of the Arecibo Observatory or existing Arecibo data to study this or any other problem in ionospheric physics (or in radio or radar astronomy) are invited to contact the Director of Observatory Operations, Arecibo Observatory, P. O. Box 995, Arecibo, Puerto Rico 00612, U.S.A.

Conclusion

For reasons that are not known either the wind or the electric field (or both) in the nocturnal F-region fluctuates in direction on a time scale of an hour or two. The resultant fluctuations in the externaly imposed ion drift velocity would have a very large effect on the structure of the nocturnal ionosphere were it not for the existence of an imperfectly understood negative feedback mechanism that causes a negative correlation between ion drift velocity components parallel and perpendicular to the geomagnetic field. This paper has

57

called attention to the phenomenon and has offered several possible explanations, but sufficient work has not yet been done to provide a clear understanding of the mechanism.

References

B e h n k e, R. A., T. H a g f o r s. Evidence for the existence of nighttime F-region polarization fields at Arecibo. — Radio Sci., **9**, 1974, 211-216.

B e h n k e, R. A., R. M. H a r p e r. Vector measurements of F-region ion transport at Arecibo. — J. Geophys. Res., **78**, 1973, 8222-8234.

D o u g h e r t y, J. P. On the influence of horizontal motion of the neutral air on the diffusion equation of the F-region. — J. Atmos. Terrest. Phis., **20**, 1961, 167-176.

H e e l i s, R. A., P. C. K e n d a l l, R. J. M o f f e t t, D. W. W i n d l e. Electrical coupling of the E-and F-regions and its effect on F-region drifts and winds. — Planet. Space Sci., **22**. 1974, 743-756.

P e t e l s k i, E. F. Real height variations of the ionospheric F2-layer above some pairs of geomagnetically conjugate stations. — J. Atmos. Terr. Phys., **34**. 1972, 1163-1170.

P e t e l s k i, E. Dynamik der Ionosphärischen F2-Schicht Mittlerer Breiten über Erdmagnetisch Konjugierten Punkten-Messergebnisse. Ph. D. Dissertation, University of Göttingen, 1973.

R i s h b e t h, H. The effect of winds on the ionospheric F2 peak. — J. Atmos. Terr. Phys., **29**, 1967, 225-238.

R i s h b e t h, H. The F-layer dynamo. — Planet. Space Sci., **19**, 1971, 263-267.

R i s h b e t h, H. Polarization fields produced by winds in the eqatorial F-region. — Planet. Space Sci., **19**, 1971, 357-369.

R i s h b e t h, H., O. K. G a r r i o t t. Introduction to Ionospheric Physics. New York, Academic Press, 1969

R i s h b e t h, H., L. R. M e g i l l, J. H. C a h n. The effect of ion-drag on the neutral air in the ionospheric F-region.—Ann. Geophys., **21**, 1965, 235-244.

S t u b b e. P., S. C h a n d r a The effect of electric fields on the F-region behaviour as compared with neutral wind effects. — J. Atmos. Terr. Phys., **32**, 1970, 1909-1919.

T h o m a s, D. P., P. J. S. W i l l i a m s. Measurements of ion-drag induced by plasma velocity in the F-region. — J. Atmos. Terr. Phys., **37**, 1975, 1271-1275.

Корреляция между ветром и электрическим полем в естественной F-области

Дж. С. Дж. Уокер

(Р е з ю м е)

Измеренная скорость ионов в E- и F-областях показывает отрицательную корреляцию между параллельной компонентой электрического поля, которая представляет собой комбинированный эффект диффузии и меридионального ветра и перпендикулярной компонентой, которая вызвана зональным электрическим полем. Представлены объяснения этой корреляции. Одно из них связано с ионным увлечением, которое вызывает отклик ветра в F-области на изменение ионной скорости. Другой механизм предполагает, что ветер в F-области является причиной возникновения поляризационного электрического поля, которое вызывает дрейф. Дискутированы возможные следствия от действия отдельных механизмов.

Measurement Results and Conclusions on the Spectral Reflective Coefficients of Volcanites, Granitoides and Gneisses

H. B. Spiridonov, A. H. Krumov, N. K. Katzkov, S. N. Yovchev

1. Definition of the Problem

The remote sensing of the Earth by air- and space-born high sensitive instruments provides for images (photographs and photoelectron pictures) of land and water surface in several ranges (channels) of the visible and near infrared portion of the electromagnetic spectrum. These images are of general application and the different formations are outlined within the respective channels. Based on this information, the geological and geomorphological studies specify the location, shape and sizes of various geological bodies; maps of lineament and circular structures are compiled. All this is an initial stage in applying remote techniques in geology. In future there have to be developed methodics of identifying geological objects, based on their spectral reflective characteristics. A necessary condition here is to provide for system and multiple laboratory and ground (field) studies on the main classes of geological object within their different behaviours and to prepare a catalogue of their spectral reflective characteristics (SRC). Referring to that, some work has been done in Bulgaria in cataloguing the SRC of the major genetic rock classes: magmatic, metamorphic and sedimentary. It is known that the SRC of a given object is the dependence of the spectral reflective coefficient on the wavelength within a given range of the electromagnetic spectrum. The spectral reflective coefficient (SRCO) is the ratio between the reflected radiation from the studied object (B_λ obj.) and the maident radiation on the reference object (screen) (B_λ ref.), i. e. with known reflective coefficient and spectral characteristics within the studied range.

2. Instruments and Measurements Techniques

Our Laboratory has developed a portable spectrometer to measure the SRC of various earth formations and objects *in vitro* and *in situ*. The instrument, known as ISOCH-020, consists of twenty channels with channel width 10-12 nm and works within the range of 400-800 nm at aperture angle of view

--13°. The natural sunlight is used in field work and a xenon lamp with power of 100 W or other artificial source of light, and the non-uniformity of its spectral characteristic of irradiation within the range of 400-800nm does not exceed 30%. A specially designed screen 80 mm in diameter is used as reference object. The screen has a photometric characteristic close to the one of ideal diffusion reflective white surface. The average SRCO is over 95% and the non-uniformity of SRC within the range of 400-800 nm is ±0.25%.

The rock samples to be studied have the shape of irregular polyhedron, with natural roughness and in certain cases one of the faces was additionally polished. Studies were perfomed under natural sunlight and the solar zenith angle varied between 46 and 65°. In order to reduce as much as possible the influence of the diffuse scattered light by the surrounding objects, the instrument and the samples were placed on black-mat tissue. In dependence on the sample sizes, the distance to the optic aperture of the instrument was selected so that the field of view would embrace as much as possible of the measurable surface. That was necessary because of the fact that the diffuse indicatrice of the actual object had to be considered, due to large solar zenith angles, microshades would appear and they reduce the SRCO.

3. Brief Petrographic Characteristics of the Rocks

Samples to measure the coefficient of spectral brightness are taken from various outcrops observed in different parts on the Bulgarian territory and are selected in such a way as to be representative of magmatic and metamorphic rocks.

a) Volcanites

Samples from two big groups of volcanic rocks are selected — acid and medium acid. The samples are taken mainly from the Rhodopes and the Western part of Sredna Gora mountain, i. e. South and West of Bulgaria. The group of acid rocks comprises rhyolites (samples Nos. 1-6), rhyodacite (No. 7), delenites (Nos. 8-9) and the medium acid rocks are presented by No. 10 — latite and No. 11 — andesite.

The age of the volcanic rocks is Paleogene and they are related to the Alpine orogenic volcanism. They occur as flows, subvolcanic bodies and dikes, intruded in the crystalline complex and the granitoides of the Rhodope massif, as well as in depressions located between its major morphostructures.

Among the acid volcanic rocks the rhyolites are widespread. Their common feature is the presence of aphanitic ground mass, composed of potassium felspar, quartz and volcanic glass. In it phenocrysts of plagioclase, felspar, quartz and sometimes biotite, amphibole and pyroxene are observed. The groundmass versus porphyry individuals is from 85 to 30%. The rhyolites are mainly of felsitic (samples Nos. 1-4), porphyry (No. 5) and hyaline (No. 6) texture. Accessory minerals in the rhyolites are zircon, tourmaline, titanium, magnetite. The rhyolite texture is fluidal banded.

Macroscopically the plagiorhyolite-rhyodacite (No. 7) has fine porphyritic texture - holocrystalline for the ground mass. The main rock-forming minerals are: plagioclase, felspar, biotite, amphibole and rarely quartz.

The coarse porphyritic delenites are subvolcanic bodies. They have micro- to medium-grained alotriomorphic texture. Main intratelluric minerals are: pyroxene, amphibole, plagioclase, quartz and felspar (sanidine). Accessory: zircone,

apatite, titanite, magnetite, orthite, some secondary minerals as epidote, chlorite, sericite also occur.

The medium acid volcanic rocks are presented by latite (No. *10*) and andesite (No. *11*). These are melanocratic rocks with typical hialopilitic (andesite) texture and massive structure. Microscopically the ground mass is aphanitic composed of plagioclase, pyroxene, volcanic glass. Porhyries of plagioclase, pyroxene and amphibole may be observed here and very rarely — olivine.

b) Granitoides

They are from Rilo-Rhodopean batholites. Samples of granodiorites, biotite granites and two-mica granites are collected. Here are samples of numbers: *4584, 4732, 3011, 7107, 2086, 5368, 2193, 8653, 3735, 2224, 1 and 11*.

The granitoides are mainly coarse- to medium-grained granular rocks. Their structure is mostly hipidiomorphic granular, sometimes porphyritic and in certain cases — cataclastic. Their texture is massive, sometimes parallel. Main rock forming minerals are: felspar, quartz, plagioclase, biotite and two-mica muscovite. Secondary and accessory minerals are: orthite, titanite, zircon, apatite and ore minerals.

c) Gneisses

Two types are considered: biotite and two-mica (samples Nos. *340, 1907* and *5005*).

Gneisses are fine- to medium-grained rocks with lepidogranoblastic structure and parallel texture. The main minerals are: plagioclase, quartz, biotite and muscovite. Accessories are: zircon, rutile, apatite and ore minerals.

4. Discussion of Results

Both within the period of measurements and when discussing the results, the factors with greatest influence on the rock SRCO may be defined separately in two principal groups: internal and external.

Among the external factors the main role is played by the source of light, which may be of natural or artificial origin, but its influence is known as a rule and could be considered in data interpretation.

Among internal factors significant is the influence of the structural-textural feature, the mineral and chemical composition, the surface of the measured samples, etc.

When measuring the spectral brightness of the different genetic classes of rocks, sun was used as a source of light. The strength of solar irradiation for the geographic latitude of Sofia (eastern longitude —23°20′45″; northern latitude — 42°41′02″) depends on solar location over horizon, i. e. on the zenith angle. Measurements were performed during the autumn of 1978, Sept. 30 and Oct. 3-4, within the interval 11:23-15:51. During these days the zenith angle changed from 46 to 65°. When comparing the measured values of the SRCO for the three days and for the interval of noon-hours of the autumn season, it was determined that the solar zenith angle is of weak importance (Tables 1 and 2).

61

Table 1

Spectral Reflective Coefficient of Volcanites

Rock	rhyolite		rhyolite		rhyolite		rhyolite		rhyolite	perlite		rhyodacite		delenite	delenite	latite		andesite
No.	1		2		3		4		5	6		7		8	9	10		11
hm/surface	rough	polished	rough	polished	rough	polished	rough	polished	rough	rough	polished	rough	polished	rough	rough	rough	polished	rough
402	22.0	34.0	18.0	22.5	22.0	33.0	15.0	18.5	24.0	30.0	41.0	22.0	42.0	21.0	11.0	14.0	22.0	10.0
411	22.0	33.0	18.0	22.5	22.0	33.0	15.5	18.5	23.0	30.0	41.0	22.0	41.5	20.5	10.5	14.0	22.5	11.0
425	22.0	33.0	17.0	23.0	22.5	33.0	16.0	18.5	23.0	29.5	40.0	21.0	41.0	20.5	10.5	14.5	22.5	11.0
440	23.0	34.0	18.0	23.0	23.0	33.0	16.5	19.0	23.0	29.5	41.0	22.0	43.0	20.5	10.5	15.5	23.5	10.5
464	24.0	35.0	18.0	23.0	24.0	33.0	17.5	19.0	23.0	30.0	41.0	23.5	43.0	20.5	11.0	15.5	23.5	11.0
483	25.0	35.5	18.5	24.0	24.5	33.0	18.0	19.0	24.0	31.0	41.0	24.5	44.0	21.0	11.5	16.0	23.5	11.5
501	26.0	36.0	19.5	24.5	25.0	33.5	19.0	19.5	24.0	31.5	41.0	25.5	44.5	21.0	11.5	16.5	23.5	12.0
546	31.0	39.0	22.0	27.0	26.0	34.5	22.0	21.5	27.0	33.5	42.0	30.0	48.0	22.5	14.0	17.5	23.5	13.0
557	32.5	40.0	23.0	27.5	27.0	34.5	23.0	21.5	28.5	34.0	45.0	31.5	49.0	23.0	15.0	18.5	23.0	14.0
597	37.0	41.5	25.0	29.0	28.0	35.5	25.5	23.0	31.0	37.0	46.5	33.5	50.0	24.0	16.0	17.5	23.0	14.0
618	39.0	42.5	25.5	30.0	29.5	36.0	27.0	24.0	33.0	38.5	48.0	36.0	51.0	25.5	17.0	18.0	23.0	15.5
662	41.0	43.0	26.5	30.0	30.0	36.0	28.0	24.0	34.0	40.0	49.0	37.5	51.0	27.0	17.5	17.5	23.0	15.5
689	43.0	44.0	27.5	30.5	30.5	36.5	29.0	24.5	36.0	42.5	51.0	39.0	51.0	28.0	18.0	17.5	22.0	16.5
701	43.0	44.0	27.0	30.5	31.0	37.0	29.0	24.5	36.0	42.5	50.0	39.0	51.0	28.0	19.0	17.5	22.5	16.5
713	43.0	44.0	27.0	30.5	30.0	36.0	29.0	26.5	36.0	43.0	50.0	40.5	51.5	28.5	19.0	17.5	22.0	16.0
725	44.0	45.0	28.0	30.5	30.0	36.0	29.0	24.5	38.0	44.0	52.0	40.5	51.0	30.0	20.0	18.0	22.0	17.0
740	45.0	45.0	28.0	30.5	30.0	36.0	29.5	25.0	37.0	45.0	52.0	41.0	51.0	30.0	20.5	17.5	22.0	17.5
753	45.5	45.5	28.0	31.0	30.0	36.0	30.0	24.5	37.0	45.0	52.0	41.0	51.0	30.0	20.5	17.0	21.5	17.0
775	46.0	45.0	28.0	30.5	30.0	36.0	30.0	24.5	37.0	45.0	52.0	41.0	51.0	30.0	21.0	18.0	22.0	15.5
802	46.0	44.0	27.0	29.5	30.0	35.0	30.0	23.5	37.5	45.0	52.0	41.0	51.0	30.0	24.0	18.0	21.5	15.0

Table 2

Spectal Reflective Coefficient of Granitoides and Gneisses

Rock	Biotite		Granites				Two-mica granites			Biotite granodiorite			Gneisses		
No.	2086	5368	2193	3735	8653	2221	I	II	4584	4732	3011	7107	1907	5005	340
nm/surf.	rough	rough	rough	rough	rough	rough	rough	rough	rough	rough	rough	rough	rough	rough	rough
402	42.5	40.0	35.0	39.0	49.0	27.0	51.5	48.0	44.0	22.0	23.0	22.0	13.0	20.0	7.5
411	41.5	41.5	35.0	36.0	47.0	26.5	49.5	47.0	44.0	22.5	23.0	22.0	13.5	20.0	9.5
425	41.0	41.0	35.0	38.0	48.0	26.0	49.5	47.0	45.0	22.0	23.5	22.5	13.0	20.0	9.0
440	42.0	41.5	35.0	39.5	47.0	27.0	50.5	48.5	45.5	23.0	23.5	22.5	13.5	20.5	9.0
464	44.5	41.5	36.0	40.0	44.0	28.0	53.0	50.0	44.5	24.0	25.0	22.5	15.0	21.0	10.0
483	44.5	42.5	37.5	39.0	45.0	30.0	54.0	49.5	46.5	25.0	24.0	24.0	16.0	22.0	10.0
501	45.5	43.5	38.0	37.5	44.0	30.0	55.0	49.5	48.0	26.0	25.0	24.5	17.0	22.5	10.0
546	49.5	46.0	43.0	41.0	46.5	34.0	58.5	53.0	49.0	29.0	26.0	27.0	24.0	26.0	11.5
557	51.0	48.5	43.5	42.0	46.0	35.0	59.0	53.5	50.0	29.5	27.0	27.5	25.0	27.0	17.0
597	52.0	48.0	45.0	43.0	46.0	36.0	60.0	53.5	51.0	30.0	27.0	28.0	27.0	28.0	17.5
618	53.0	49.5	45.5	44.0	47.0	37.5	61.0	55.0	52.5	31.0	27.5	29.0	29.0	29.0	20.0
662	55.5	49.0	47.0	44.5	46.5	37.5	62.0	58.0	52.0	32.0	27.0	30.5	29.0	30.0	21.0
689	54.5	51.0	46.5	45.0	46.0	40.5	63.5	57.0	51.0	32.5	27.0	31.0	30.0	30.0	23.0
711	55.0	50.5	48.0	45.0	45.0	39.0	62.5	55.5	52.0	32.5	28.0	31.0	29.5	30.5	23.5
713	54.5	51.0	46.5	45.0	47.0	38.5	62.5	58.5	52.0	33.0	28.0	32.0	30.0	30.0	24.0
725	56.0	48.0	47.5	45.5	46.0	39.5	64.0	58.5	53.0	33.0	27.5	31.5	31.0	30.0	24.5
740	56.5	52.0	46.5	45.5	46.0	40.0	63.0	59.0	52.5	33.0	27.5	31.5	31.5	30.5	25.0
753	56.0	52.0	48.0	46.0	47.0	40.5	63.5	58.0	53.5	33.5	27.0	31.5	31.5	30.5	26.5
775	55.5	52.0	48.0	46.0	48.0	41.0	64.5	60.0	54.0	34.0	27.0	32.0	32.0	31.0	27.0
802	57.0	52.0	47.0	46.0	46.0	40.5	64.0	59.0	53.5	34.0	27.0	32.0	31.5	30.5	27.0

63

a) Volcanites

Data obtained by sample measurements of acid volcanic rocks show that highest is the SRCO of sample No. *1*-rhyolite taken from the Eastern Rhodopes. Sample No. *2* — rhyolite from the same volcanic region is defined by lowest indices of spectral brightness. Both samples do not differ in such structural indices as shape, size of porphyries, but there is considerable difference in the quantity of ground mass. Referring to this index, the acid volcanic rocks may be divided into two groups: (1) with great amount of ground mass (over 80% for samples Nos. *1, 6, 7*), and (2) with increased porphyry content (30-40% — samples Nos. *2, 3, 4*) (Fig. 1, Table 1). The rock samples of the first group are characterized by high values of SRCO within the range of 600-800 nm. The rhyolite (Sample No. *5*) under equal content of porphyry and ground mass has average indices of reflective capacity with respect to the upper two groups (Fig. 1, Table 1). Sample No. *7* — plagiorhyolite has the followng specifics: within the range of 400-500 nm the spectral brightness, equals the rhyolitic one, but within the range of 600-800 nm it augments, which may be interpreted with structural features of the rock. It is of dense almost aphiric structure for the porphyry and holocrystalline — for the ground mass. This structural index of the sample brings it closer to the rhyolites with higher amount of ground masses. In the case, the small sizes of the minerals definitely influence the increase of the SRCO within the range of 600-800 nm. The reverse is the effect on the spectral brightness in augmenting the porphyric sizes. Typical example is the coarse-grained porphyric delenite (sample No. *9*). Here the lowest values of spectral brightness are observed — 10% within the short-wave interval of the electromagnetic spectrum, up to 24% in the IR range. The other sample (No. *8*) of coarse-grained porphyric delenite does not differ from No. *9* in structural indices (sizes and shape of minerals) but its indices are with 10% higher on the average. In macroscopic comparison of the two samples a difference between the surfaces under which the measurements are taken, appeared. For sample No. *9* it is rough and uneven, with difference between roughnesses up to 5 nm. At equal other conditions one more index is introduced, namely the surface of the measured samples. Under natural conditions, this index woule probably be of lesser importance because of physico-chemical rock weathering, dust, development of microorganisms, etc.

The dominant colour of the acid volcanic rocks is rose-violet and pale rose. The perlite (sample No. *6*) represents an exception — it is almost white and the rhyolite (sample No. *4*) is of intensive red colour. And in fact, only these rock samples have shown SRCO indices which differ from the others and this influence is especially remarkable within the short-wave interval of the electromagnetic spectrum, between 400-500 nm. In this range the perlite shows values of spectral brightness of 10% higher and the difference with reference to the rhyolite of intensive red colour attains 15%. This difference is the smallest within the range of 546-557 nm.

The latite (sample No. *10*) and the andesite (sample No. *11*) refer to the medium-acid rocks. Here a steep decrease of the reflective capacity is observed. A slow increase of the SRCO is found for the latite — from 14 to 18%. The lowest values of spectral brightness (from 10.5 to 17.5%) are measured also for the andesite, and in the near-infra-red region a certain decrease is detected between 753 and 802 nm. The latite demonstrates another peculiarity — from 557 to 802 nm the values of SRCO are almost the same. Obviously, within the increase of the dark-coloured minerals, the reflective capa-

64

city of the volcanic rocks considerably decreases and this is to be traced within the whole measurement range of the electromagnetic spectrum.

The colour of the medium acid rocks is: grey-greenish for the latite and dark grey for the andesite. The following peculiarity has been determined:
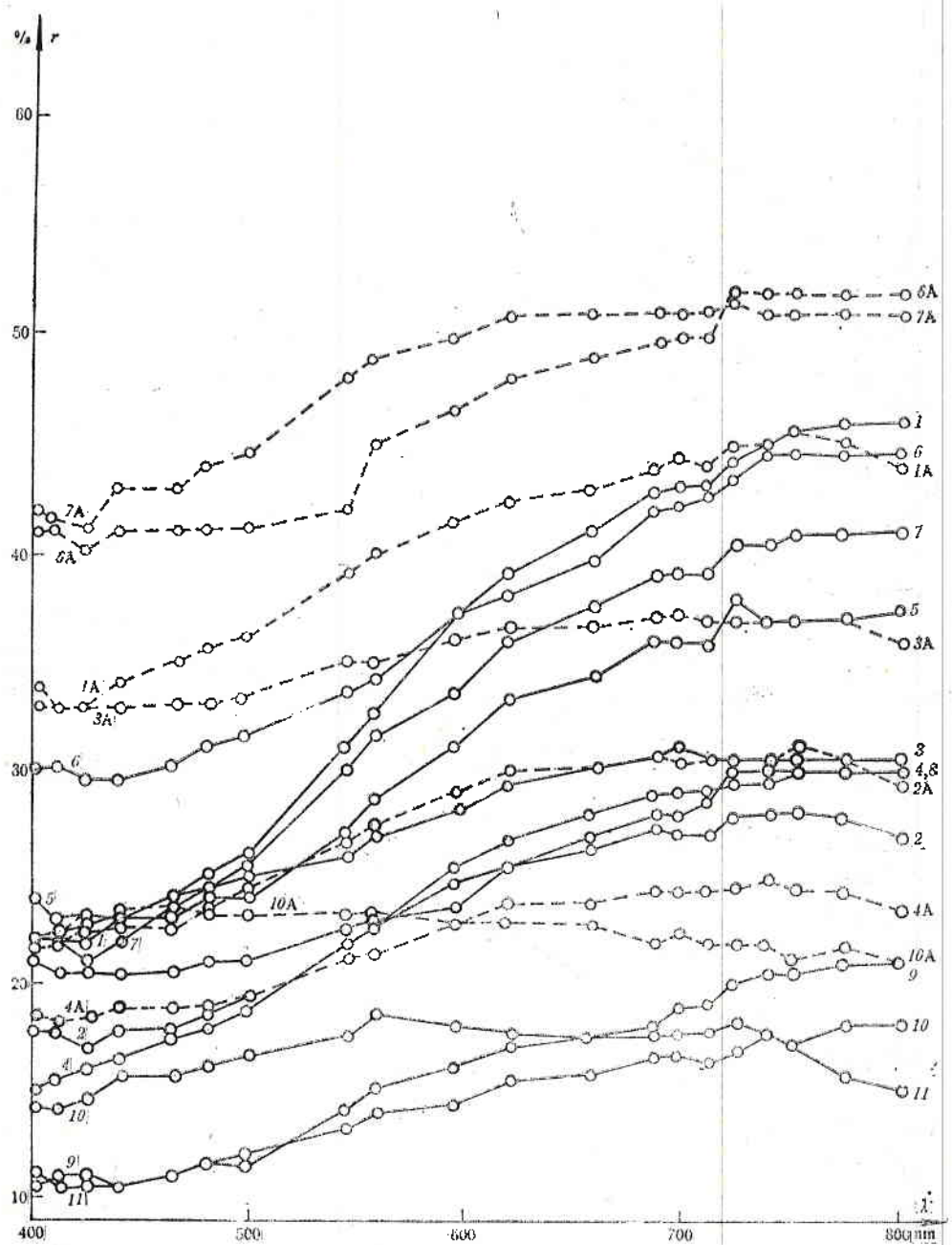

Fig. 1. SRCO curves of volcanites

Samples: *1, 2, 3, 4, 5* — rhyolites; *6* — perlite; *7* — plagiorhyolite-rhyodacite; *8, 9* — delenites; *10* — latite; *11* — andesite; Broken curves refer to polished samples
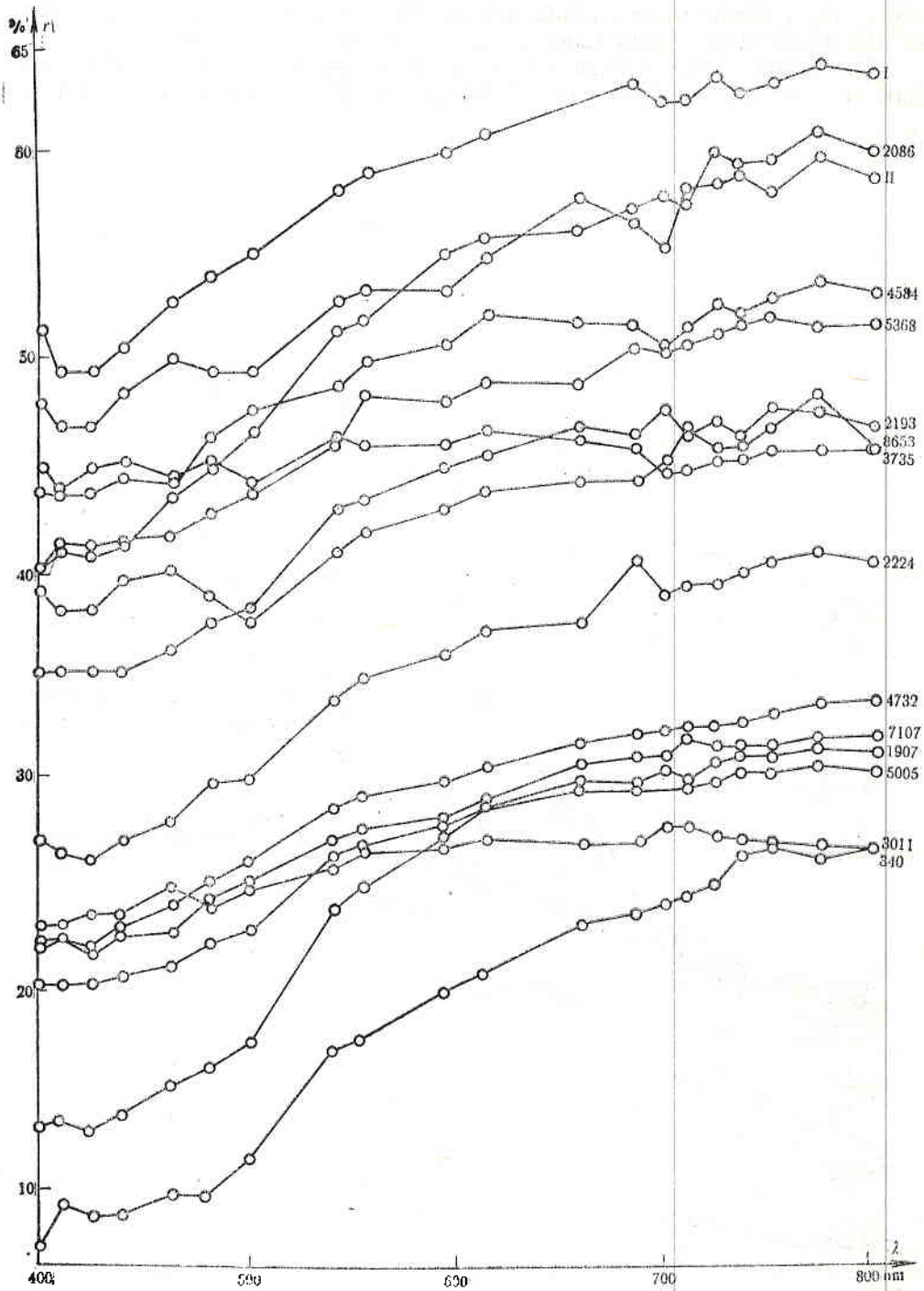
Fig. 2. SRCO curves of granitoides and gneisses

Samples: biotite granites — Nos. 2086, 5368, 2193, 3735, 8653, 2224; two-mica granites — I, II; biotite granodiorites — Nos. 4584, 4732, 3011, 7107; gneisses — Nos. 1907, 5005, 304

under all measurements the SRCO of the lathite is higher than the andesite SRCO by 4-5% on the average.

Measurements have shown that the rock surface influences significantly the SRCO, that is why one of the sample faces was additionally polished (Fig. 2, Table 1). It was found that within the interval of 400 to 550 nm, the coefficient of light brightness increases by 10% on the average and to the near infra-red range gradually decreases and is about 5%.

b) Granitoides

When measuring the coefficient of light brightness of granitoides, it was determined that its highest values are attained with the two-mica granites and gradually decreases to the biotite granites and the granodiorites.

The two-mica granites perform SRCO changes from 48-51% at 408 nm to 59-64% at the near infra-red region. The lower values of sample II compared to sample I are due to the greater size of the mineral grains.

The biotite granites have SRCO from 28 to 60%. Their average values are between 35 and 50% (Fig. 2, Table 2). Lowest are the values of sample No. *2224* (from 28 to 40.5%). We assume that this is due to the weathered sample surface and the greater quantities of the biotite. Highest spectral brightness values has sample No. *2086* at 775 nm — 62%. The reflective capacity increase results from the augmented content of salic minerals as the percentage of the potassium felspar is particularly high. The surface of the rock is smooth. For the cataclastic biotite granite (Sample No. *8653*) SRCO has almost identical values, which is due to the uniform distribution of the mafic and salic minerals.

Results from SRCO measurements of biotite granodiorites show that they have lowest value compared with other granitoides. Sample No. *4584* is a certain exception, where SRCO changes from 44 to 54%, while for the other samples this varies between 22 and 35%. There is no difference in structural features and mineral composition between the samples. The difference is to be traced in the gravity ratio between the mafic and salic minerals. Sample No. *4584* contains about 65% light minerals (quartz, felspar, plagioclase). Furthermore it is cut by a small aplite vein. The surface is very fresh. Lowest values of SRCO has sample No. *3011*, here the mafites are predominant. Sample No. *7107* — biotite adamellite — refers to this group. Its graph does not differ from the other granodiorites.

c) Gneisses

Gneisses exhibit the lowest values of SRCO. For the biotite gneisses (samples Nos *1907, 5005*) the SRCO varies between 13-20% at 402 nm to 30-31.5% at 802 nm. Surprisingly, the lowest SRCO was determined for the two-mica gneiss — 340, i. e, from 7.5 to 27%. We assume that the reflective capacity decreases due to the highly expressed banded texture.

Typical peculiarity for the volcanites and gneisses, referring to the values of the spectral brightness coefficient, is the presence of two plateaux. The first is determined in the short-wave interval of the electromagnetic spectrum, between 400-500 nm with very poor decrease within the interval 411-425 nm. The second plateau is within the range of 700-802 nm also with weak decrease after 775 nm. In fact the two plateaux represent ranges within the optic spectrum with width up to 100 nm, where the reflective capacity is constant. This refers to the group of acid and medium acid rocks.
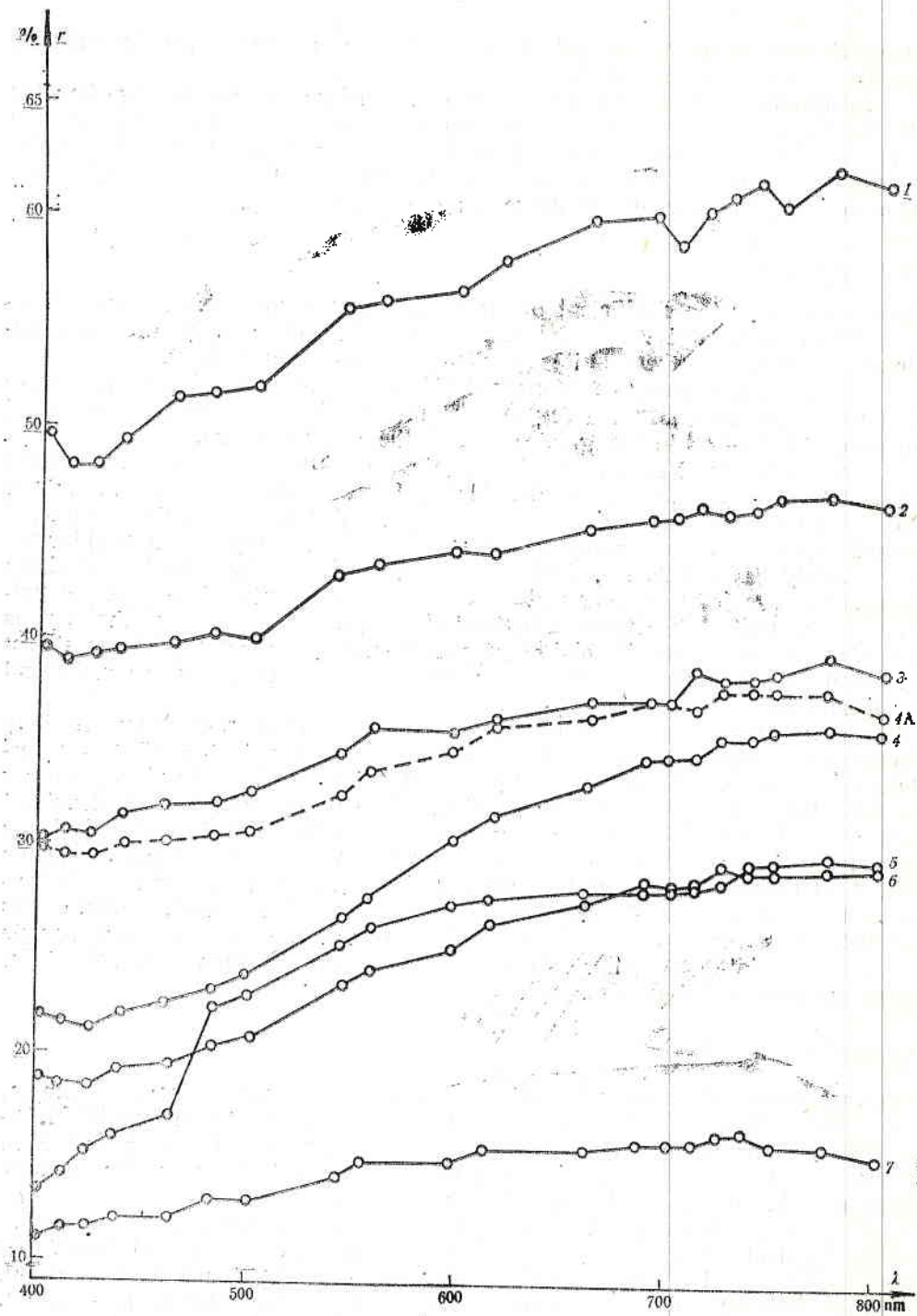
Fig. 3. SRCO averaged curves of volcanites, granitoids and gneisses
1 — two-mica granites; *2* — biotite granites; *3* — granodiorites; *4* — rhyolites; *5* — gneisses; *6* — delenites; *7* — andesite-latite

Another clearly exspressed peculiarity of the studied samples is the rapid increase of the spectral brightness within the interval of 500-700 nm. This feature gradually decreases with the increase of the dark-coloured silicates.

5. Conclusions

The measurements and the interpretations of the results obtained give grounds for the following conclusions:

1. Direct proportional dependence exists between the ground mass quantity and the SRCO for the acid volcanic rocks.

2. Acid rocks have higher SRCO values than the medium-acid and the basic rocks.

3. The predominant quantity of salic minerals augments the SRCO and vice versa.

4. The influence of the rock structure is manifested through the size of the minerals: at greater sizes of the porphyries the SRCO decreases and vice versa.

5. Smooth and polished rock surfaces increase the SRCO.

6. Samples of weathered surface have lower SRCO than the fresh ones.

7. Rock of massive texture have higher SRCO than the ones of parallel (banded) structure.

8. The lighter colour of rocks increases the SRCO and vice versa.

References

1. Кринов, Е. Л. Спектральная отражательная способность природных образований. М., АН СССР, 1947.
2. Gunther, F., M. H. Podwysocki. Discrimination of rock and soil types by digital analysis of Landsat data. — In: Proc. Amer. Soc. Photogramm., 43rd Annu. Meet., 1977, Washington, D. C., S. I., 155-156.
3. Мелешко, К. Е. Спектрофотометрические исследования природных покровов Земли. Л., Недра, 1976.

Результаты и интерпретация измерений
спектральных отражательных характеристик
вулканитов, гранатоидов и гнейсов

Х. Б. Спиридонов, А. Х. Крумов, Н. К. Кацков, С. Н. Йовчев

(Резюме)

В данной работе приводятся результаты измерений спектральных отражательных характеристик скальных образцов вулканита, гранатоида и гнейса в лабораторных условиях с помощью разработанного болгарскими специалистами полевого спектромера ИСОХ-020 при естественном освещении Солнца. На основе полученных данных сделана интерпретация о влиянии геологического типа, структуры, окраски и состояния поверхности исследуемых образцов на их спектральные отражательные характеристики.

Asymmetry in Irregularity Distribution of Both Hemispheres Obtained by Spherical Ion Traps and Langmuir Probes

G. A. Stanev, L. G. Bankov, D. K. Teodosiev

Introduction

The different irregularity characteristics in charged thermal particles density have been studied recently in a series of papers using various methods. Radio scintillation observations [1, 2] give a good possibility to study the temporal variations of the irregularity regions at a given point of the Earth, as well as their relation with the geomagnetic activity. Satellite use enables the planetary study of irregularities and the direct measurement of the amplitudes and the scale sizes of the ionospheric irregularities. Using the data from the Langmuir probe on Alouette-2, D y s o n [3] describes the equatorial and the polar boundary of the high latitudinal irregularities. M c C l u r e and H a n s o n [4] show different types of ionospheric irregularities, using results obtained by retarding potential analyser on OGO-6. The spectral characteristics of the different types of irregularities are examined in [5] and they are shown to be equal for the irregularities both in high latitudes and in equatorial region. S a g a l y n et al. [6] describes diurnal and seasonal changes of high latitudinal irregularities and the difference in both the hemispheres, using spherical electrostatic probe. O z e r o v [7] examines the probability of irregularity appearance in dependence on the geomagnetic latitude and the geographic one also with the help of spherical electrostatic probe. It is shown that for given irregularity amplitudes, the calculated ratio scintillation index, applied to the equatorial region latitudes, shows good coincidence with experimental data [8].

Several theories for the interpretation of irregularities appearance have been suggested [9, 10, 11], but the difference in methods and the relatively poor data made difficult the theoretical interpretation.

This paper treats the diurnal variations of the high latitudinal irregularities in the Northern and Southern hemispheres. Results are based on measurements on positive ion density with spherical electrostatic probe and the Langmuir probe data from Intercosmos-8 [12] are used for comparison.

Experiment

Intercosmos-8, launched on Dec. 1, 1972 has initial apogee of 676 km over the South pole and perigee of 215 km over the North pole. The orbit changes relatively fast, and by the end of January 1973 the orbit has apogee of 446 km in the Northern hemisphere, and perigee of 192 km in the Southern hemisphere close to the equator. This enables the observation of ionospheric phenomena at different altitudes within a short period of time. Measurements of about 120 orbits have been used within the period Dec. 3, 1972, Jan. 27, 1973.

Description of some equipment installed on Intercosmos-8 and of some results obtained by the equipment, are given in [13, 14, 15, 16]. In order to measure irregularities in the ion concentration, with respect to the satellite body negative voltage 5V is supplied to the outer grid of the probe for a period of about 3 s. The following 3 s a swept voltage is supplied, and during that period the concentration is measured. This mode of operation is repeated each 6 s. The high negative potential assures work in regime of saturation and collector current fluctuations depend strongly on the change of ion concentration.

Bit level sensitivity in irregularity mode depends on concentration and for 5×10^5 cm^{-3} it is 5%, respectively for 4×10^4 cm^{-3} it is 15%. Irregularity space dimensions, which can be recorded, are within limits of 2-20 km.

Parallel to that, the behaviour of ion concentration measured by Langmuir probe is observed. Because of the fact that the Langmuir probe works 1 s per each 9 s cycle, the characteristics of the upper irregularities cannot be obtained, but in the irregularity zone great scatter of electron concentration value is always observed.

Using collector current records, the sizes and the relative amplitude of the irregularities have been evaluated, and a comparison with data from [5] has been made. Regardless of the different way of parametric determination and the greater scatter, the same linear dependence between dimensions and relative amplitude with slope close to 1 is observed.

Diurnal Variations of Irregularity Appearance Limits in Polar Regions

In order to study the diurnal dependence of irregularity appearance, we divided them into 3-hour intervals by local time, respectively for relatively quiet geomagnetic conditions — $k_p \leq 3$, and disturbed conditions — $k_p > 3$. In this way, the equatorial boundary of high-latitudinal irregularities, shown on Fig. 1 (solid line), have been determined. This was done for both hemispheres, at different geomagnetic situation.

In the Northern hemisphere (Fig. 1a) the equatorial boundary at $k_p \leq 3$ is poleward during noon hours at about 70° invariant latitude and is most remote from the pole during night hours 21-24h and predawn hours 03-06h. The same behaviour is maintained under increased geomagnetic activity — $k_p > 3$, as the equatorial boundary generally shifts to the equator, on the average by 3° (Fig. 1b). Satellite height changes in this region from about 210 to 440 km. Data on sector 06-09 are not available.

In the Southern hemisphere (Fig. 1c) the boundary at $k_p \leq 3$ is poleward during noon hours, at about 75° invariant latitude, and most remote from the pole during night hours 21-03h, at about 60° invariant latitude. Data on the

71

Southern hemispere and on $k_p > 3$ are insufficient, but show the same dependence (Fig. 1d). It is interesting to note that in the Southern hemisphere the equatorial boundary in predawn sector 03-06h is obtained for all k_p very close
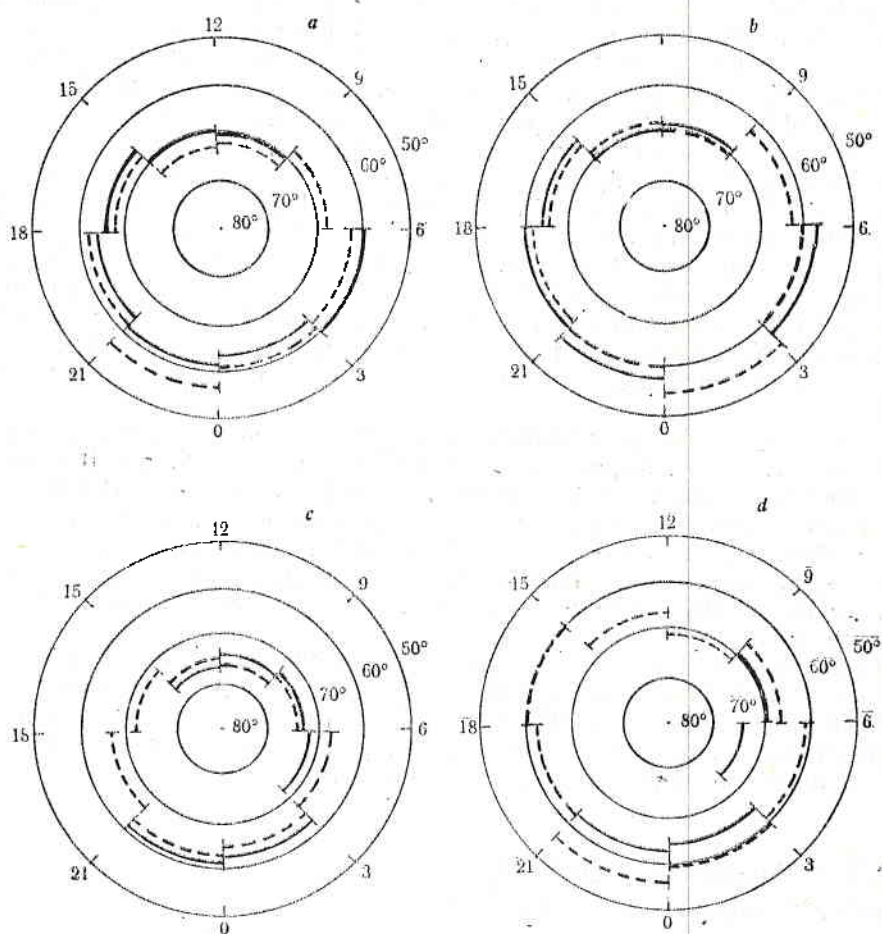

Fig. 1. Equatorial boundary of high-latitudinal irregularities (solid line). It is given for the Northern hemisphere at $k_p \leq 3$ (a) and at $k_p > 3$ (b), as well as for the Southern hemisphere at $k_p \leq 3$ (c) and at $k_p > 3$ (d). The equatorial boundary of the irregularities obtained under the same conditions by S a g a l y n et al. [6] is also shown (dashed line)

to the pole at about 72° invariant latitude. Satellite altitude changes from 270 to 650 km.

Poleward from the equatorial boundary, irregularity records were not always continuous. As a rule, we have observed simultaneous concentration decrease and irregularity disappearance in the midlatitudinal trough, around its minimum.

In the Northern hemisphere irregularity disappearance is observed at about 73° invariant latitude, but there are orbits in which irregularities in greater latitudes are continuously available. In the Southern hemisphere, irregularities have been observed up to 80° invariant latitude during predawn hours.

72

The comparison between the equatorial boundaries of the high latitudinal irregularities, at $k_p \leq 3$ in both hemispheres, shows that in the Southern hemisphere the boundary is situated more poleward than in the Northern hemi-
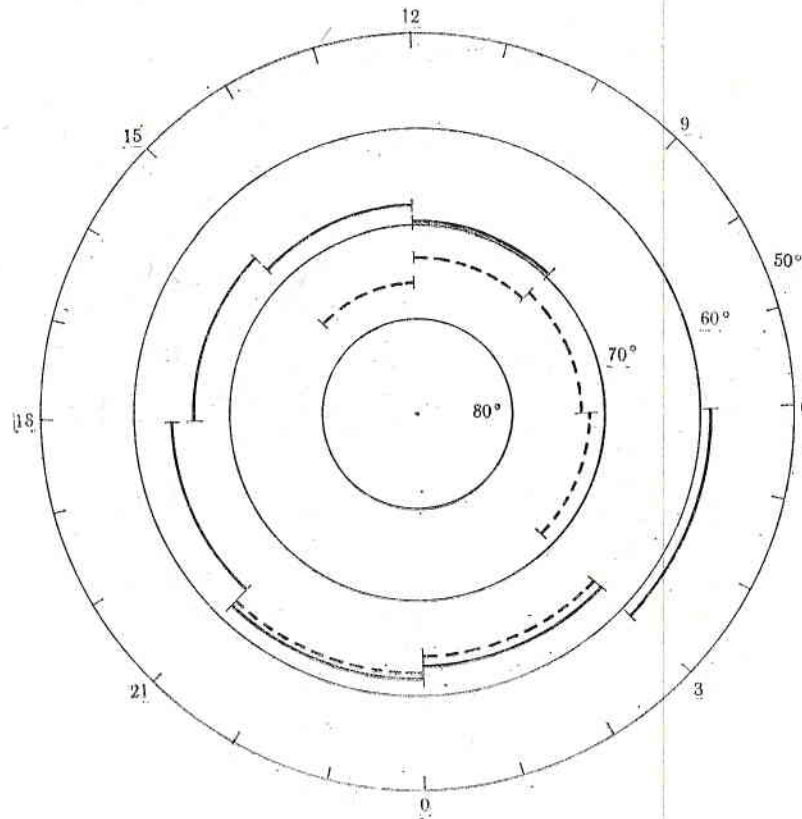

Fig. 2. Comparison between the equatorial boundary of high-latitudinal irregularities in the Northen hemisphere (solid line) and in the Southern hemisphere (dashed line) at $k_p \leq 3$

sphere, as during night hours the two boundaries almost coincide (Fig. 2). The difference during noon hours is about 5° invariant latitude. The predawn sector 03-06h is a particular case, where the difference is the greatest — 13° invariant latitude. The asymmetry obtained in the equatorial boundary agrees with the results obtained previously in [6]. This shows that this asymmetry in irregularity distribution in both hemispheres is probably due to differences in the physical conditions generating these irregularities.

Discussion

Results obtained here are in good agreement with the results of other authors. The equatorial boundary of high latitudinal irregularities, which have been determined in a similar way by S a g a l y n et al. [6], is plotted on Fig. 1 with

73

a dashed line. Differences might be due to several reasons, e. g. to different instruments. Difference in altitudes of ISIS-I transits (225-3526 km) and Intercosmos-8 (210-650 km) might also contribute to the differences in equatorial boundaries of the irregularities.
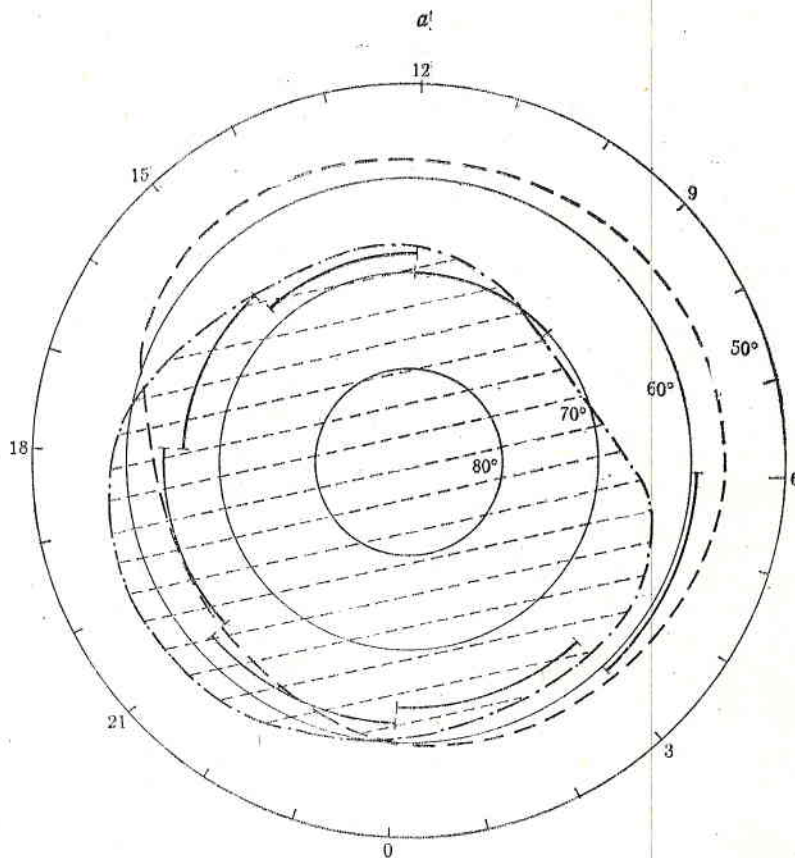

Fig. 3

a — Comparison between the equatorial boundary of irregularities with radio scintillation regions [2] (stroked) and with plasmapause situation [17] (dashed line);

Irregularity absence in the midlatitudinal trough as well as in greater latitudes can be explained easily by taking into consideration the fact that the instrument sensitivity is about 10%, and the relative amplitude of irregularities in midlatitudinal trough is less than 1 per cent [4]. The same reference shows similar decrease up to 3% in high latitudes of about 80° invariant latitude.

The comparison between the radio scintillation boundary at $k_p = 0 \div 1$ in [2] with irregularity boundary at $k_p \leq 3$ in the Northern hemisphere shows satisfactory coincidence, especially when taking into consideration the different geomagnetic situation and that the radio scintillation boundary is determined as latitude, at which the mean scintillation index at 40 MHz is 50%. Especially good is the coincidence during day hours (Fig. 3a). The difference is maximal in local time interval 18-21h, where it is about 6° invariant latitude.

At the same Fig. 3a shows the comparison between plasmapause situation $k_p \leq 3$, taken from [17] with the obtained irregularity equatorial boundary, at the same quiet geomagnetic situation for the Northern hemisphere. A good coincidence of both boundaries is observed during night hours 18-06h, while
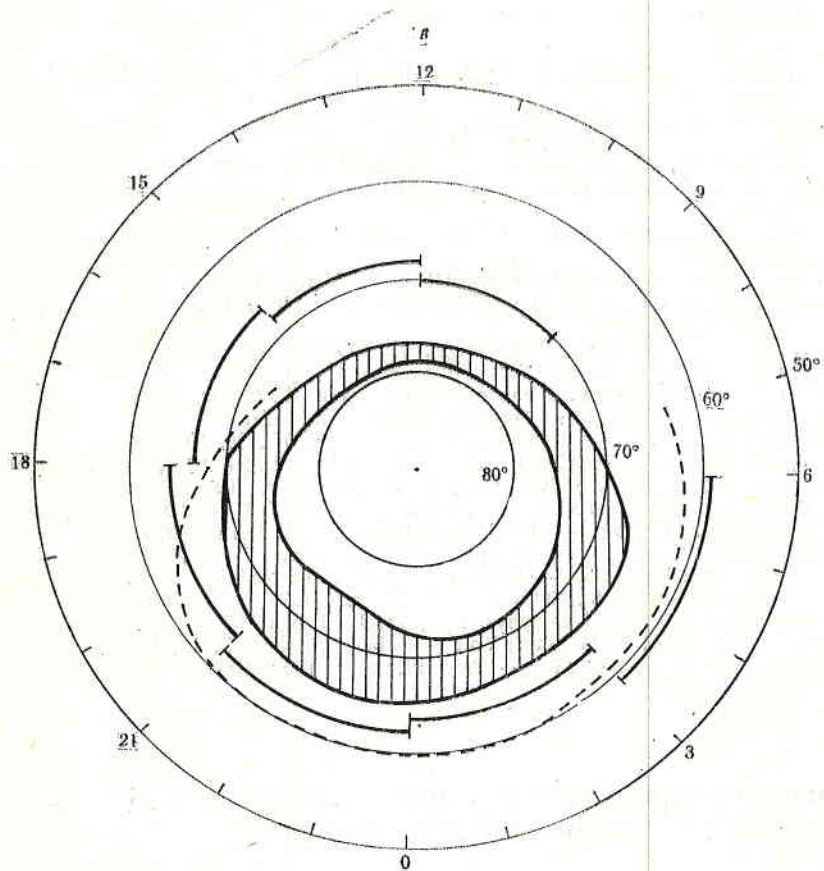

Fig. 3
b — Comparison between equatorial boundary of irregularities with midlatitudinal trough [19] (dotted line) and with auroral oval

there is rather great difference during day hours, appearing till 12° invariant latitude at the local noon.

Figure 3b shows the comparison between the irregularity equatorial boundary by Intercosmos-8 measurements, with the auroral oval taken from [18], also for the Northern hemisphere for $k_p \leq 3$. The equatorial boundary of the auroral oval is situated more poleward than the equatorial boundary of high latitudinal irregularities as the difference is maximal during day hours at about 9° invariant latitude, and is minimal at about 2° invariant latitude at local time 21-00h.

The same Fig. 3b shows the electron trough in the Northern hemisphere [19]. In the night intervals of the local time the behaviour of the electron

75

trough coincides with the behaviour of the boundary, which confirms well our observations, i. e. that irregularities appear during night hours, immedietely before midlatitudinal ion trough.

References

1. A a r o n s, J., J. P. M u l l e n, H. E. W h i t n e y. — J. Geophys. Res., **74**, 1969, No 3, p. 883.
2. A a r o n s, J. — J. Geophys. Res., **78**, 1973, No 31, p. 7441.
3. D y s o n, P. J. — J. Geophys. Res., **74**, 1969, p. 6291.
4. M c C l u r e, J. P., W. B. H a n s o n. — J. Geophys. Res., **78**, 1973, No 31, p. 7341.
5. D y s o n, P. L., J. P. M c C l u r e, W. B. H a n s o n. — J. Geophys. Res., **79**, 1974, No 10, p. 1497.
6. S a g a l y n, R. C., M. S m i d d y, M. A h m e d. — J. Geophys. Res., **79**, 1974, No 28, p. 4252.
7. O z e r o v, V. D. — IV B. 219. COSPAR XVIII. Varna, 1975.
8. B a s u, S., S. B a s u, J. N. B h a r, B. K. G u h a t h a k u r t a. — IV. B. 2. 7. COSPAR XVIII. Varna, 1975.
9. F r i h a g e n, J. — J. Atmos. Terr. Phys., **31**, 1969, p. 81.
10. F r i h a g e n, J. — J. Atmos. Terr. Phys., **33**, 1971, p. 21.
11. Г е р ш м а н, Б. Н. Динамика ионосферной плазмы. М., Наука, 1974.
12. Ч а п к ы н о в, С. К. и др. — Научные приборы, **5**, 1974.
13. C h a p k u n o v, S. K. — Compt. rend. Acad. bulg. sci., **24**, 1971, No 11.
14. C h a p k u n o v, S. K. — Compt. rend. Acad. bulg. sci., **24**, 1971, No 2, p. 183.
15. S e r a f i m o v, K. B., I. S. K u t i e v, A. Z. B o c h e v, Ts. P. D a c h e v, K. I. G r i n- g a u s, V. V. A f o n i n, G. I. G d a l e v i c h, V. F. G u b s k i y, V. D. O z e r o v, J. S c h m i l a u e r. — IV. C. 4. COSPAR XVIII. Varna, 1975.
16. S e r a f i m o v, K. B., I. S. K u t i e v, J. A r s o v, Ts. P. D a c h e v, G. S t a n e v, G. L. G d a l e v i c h, V. V. A f o n i n, V. F. G u b s k i y, V. D. O z e r o v, J. S c m i- l a u e r. — B. 3. 8., COSPAR XVIII. Varna, 1975.
17. C a r p e n t e r, D. L. — J. Geophys. Res., **71**, 1966, p. 693.
18. F e l d s t e i n, Y. I., G. G. S t a r k o v. — Planet Space Sci., **15**, 1967, p. 209.
19. J e l l y, D. H., L. E. P e t r i e. — Proc. IEEE, **57**, 1969, 1005.

Асимметрия в распределении неедноородностей в двух полусферах по данным спутника „Интеркосмос-8"

Г. А. Станев, Л. Г. Банков, Д. К. Теодосиев

(Р е з ю м е)

Рассмотрены данные ионной концентрации, полученные от около 120 орбит спутника „Интеркосмос-8" в период 12. 1972 — 1. 1973 гг. Анализированы данные неоднородностей концентрации и место их появления в зависимости от местного времени и геомагнитной активности. Сделано сравнение данных, полученных в северном и южном полушариях. Результаты исследования сравнены с результатами, полученными другими авторами.